REPORT DOCUMENTATION PAGE

Form Approved OMB NO. 0704-0188

1. REPORT DATE (DD-MM-YYYY)	2. REPORT TYPE	3. DATES COVERED (From - To)
03-10-2017	Final Report	15-Jul-2013 - 14-Jul-2017

4. TITLE AND SUBTITLE
Final Report: ARO 1.2: Solid Mechanics: Augmented Finite Element Method For High-Fidelity Analysis of Structural Composites

5a. CONTRACT NUMBER W911NF-13-1-0211

5b. GRANT NUMBER

5c. PROGRAM ELEMENT NUMBER 611102

5d. PROJECT NUMBER

5e. TASK NUMBER

5f. WORK UNIT NUMBER

6. AUTHORS

7. PERFORMING ORGANIZATION NAMES AND ADDRESSES

University of Miami - Coral Gables
1320 South Dixie Highway
Suite 650, LC 2960
Coral Gables, FL 33146 -2926

8. PERFORMING ORGANIZATION REPORT NUMBER

9. SPONSORING/MONITORING AGENCY NAME(S) AND ADDRESS (ES)

U.S. Army Research Office
P.O. Box 12211
Research Triangle Park, NC 27709-2211

10. SPONSOR/MONITOR'S ACRONYM(S) ARO

11. SPONSOR/MONITOR'S REPORT NUMBER(S) 63154-EG.28

12. DISTRIBUTION AVAILIBILITY STATEMENT
Approved for public release; distribution is unlimited.

13. SUPPLEMENTARY NOTES
The views, opinions and/or findings contained in this report are those of the author(s) and should not contrued as an official Department of the Army position, policy or decision, unless so designated by other documentation.

14. ABSTRACT

15. SUBJECT TERMS

16. SECURITY CLASSIFICATION OF: a. REPORT	b. ABSTRACT	c. THIS PAGE	17. LIMITATION OF ABSTRACT	15. NUMBER OF PAGES	19a. NAME OF RESPONSIBLE PERSON
UU	UU	UU	UU		Qingda Yang
					19b. TELEPHONE NUMBER 305-284-3221

Standard Form 298 (Rev 8/98)
Prescribed by ANSI Std. Z39.18

RPPR Final Report
as of 16-Oct-2017

Agency Code:

Proposal Number: 63154EG | **Agreement Number: W911NF-13-1-0211**

INVESTIGATOR(S):

Name: Ph.D Qingda Yang
Email: qdyang@miami.edu
Phone Number: 3052843221
Principal: Y

Organization: **University of Miami - Coral Gables**
Address: 1320 South Dixie Highway, Coral Gables, FL 331462926
Country: USA

DUNS Number: 625174149 | EIN: 590624458
Report Date: 14-Oct-2017 | Date Received: 03-Oct-2017
Final Report for Period Beginning 15-Jul-2013 and Ending 14-Jul-2017

Title: ARO 1.2: Solid Mechanics: Augmented Finite Element Method For High-Fidelity Analysis of Structural Composites

Begin Performance Period: 15-Jul-2013 | **End Performance Period:** 14-Jul-2017
Report Term: 0-Other

Submitted By: Ph.D Qingda Yang | Email: qdyang@miami.edu
Phone: (305) 284-3221

STEM Degrees: 3 **STEM Participants:** 6

Major Goals: The proposed objective of this study, according to the original propose, is to develop "an efficient and accurate multiscale computational methodology for rapid virtual testing of composites with complex microstructures". The proposed research goals are:
"1) Development of new 2D and 3D A-FEM elements that can explicitly account for statistical material heterogeneity and can faithfully predict progressive damage initiation, propagation and multi-crack interaction";
"2) Apply the new method to study composites of interest to the Army, coupled with 3D micro-CT-based precision experiments, to understand key physical phenomena of crack formation and growth, and to quantify their direct effects on structural integrity under general loads";
Two more goals were added in the 4th year extension proposal in view of the importance of material nonlinearity due to finer scale (micron- or sub-micron scale) material damage,
"3) Complete the development of a 'multi-physics' nonlinear element within the AFEM framework that will allow us to represent a microcrack in a heterogeneous medium";
"4) Verify the ability of the multi-physics element to make correct predictions of the conditions for crack deflection, bifurcation, and branching and of the influence on these phenomena of fine-scale continuum damage in the surrounding material".

Accomplishments: Major Technical Achievements resulted from the projects:

• A new augmentation formulation that enables standard finite element method to deal with strong and weak discontinuities caused by arbitrary, coupled multiple damage formation and propagation in complex heterogeneous, without the need for adding extra DoFs into the global problem.

• A novel elemental condensation procedure (consistency-check based algorithm) that demonstrated 2-3 orders of magnitude improvement in numerical efficiency, accuracy, and robustness.

• A novel inertia-based stabilizing method that guarantees unconditional convergence and allows for smooth transition from quasi-static crack development to rapid or even dynamic crack propagation, and vice versa.

• A nonlinear A-FEM to account for both finer scale (i.e. submicron scale) continuum damage or plasticity and larger scale nonlinearity due to nonlinear coupling of multiple cracks.

• Extended the new A-FEM with coupled thermal-mechanical analysis capabilities under static, cyclic, and dynamic

loading conditions.

• Much improved understanding of the interaction of multiple damage modes in composites and their convoluted influence on structural integrity through comparing/correlating detailed A-FEM analysis results against high resolution experimental measurements /characterizations (DIC, micro-CT, etc)

Training Opportunities: This project helped to train the following graduate students and post-doctorate researchers:

1. Dr. Mehdi Naderi (former post-doc researcher, 12/2012-4/2014), 80% Effort. Now with Technical Data Analysis, Inc, Washington, DC.

2. Dr. Jaedal Jung (former post-doc Researcher, 7/2014-4/2017), overall 30% effort since 7/2014. Now with Teledyne Scientific Company, Thousand Oaks, CA.

3. Dr. Derek Schesser (Ph.D student, graduated in 5/2015), 50% support from this project during 2013-2015. Now a DARPA Science Engineering Technology Advisor (SETA).

4. Ms. Brigitte Morales (PhD student, 6/2014-5/2015), 50% support. Left this program and joined another group in the department in 6/2015 after being awarded with an NSF scholarship.

5. Ms. Yunwei Xu (PhD student in progress), supported by this project 100% from 8/15/2014- 8/14/2016.

6. Mr. Yuhang Yang (PhD student in progress) supported 100% from 8/15/2016-8/14/2017.

7. Mr. Scott Floerke (MS student graduated 5/2017). Performed C4 blast simulations on aluminum panels under joined advising of the PI and Dr. Chian-fong Yen in ARL.

8. Mr. James Robertson (MS student graduated 5/2017). Programmed a fiber/matrix model generator using python script language which enabled high-fidelity RVE analyses.

RPPR Final Report
as of 16-Oct-2017

Results Dissemination: This projected resulted 17 published journal papers and 1 book chapter. Another five journal publications are in preparation. Below is the list:
Published/accepted (18):

1. Q. D. Yang and B. C. Do, “Predicting Damage Evolution in Composites with Explicit Representation of Discrete Damage Modes”, Handbook of Damage Mechanics: Nano to Macro Scale for Materials and Structures, editor George Voyiadjis. SpringerReference, New York, 2014 (book chapter)

2. W. Liu, Q.D. Yang*, S. Mohammadizadeh, and X.Y. Su, “An Efficient Augmented Finite Element (A-FEM) for Arbitrary Cracking and Crack Interaction in Solids”, International Journal of Numerical Methods in Engineering, 99 (438-468), 2014.

3. D.S. Ling*, L.F. Bu, F.B. Tu, Q.D. Yang, and Y.M. Chen, “A finite element method with mesh-separation-based approximation technique and its application in modeling crack propagation with adaptive mesh refinement”, International Journal of Numerical Methods in Engineering, 99 (487-521), 2014

4. F.B. Tu, D.S. Ling*, L.F. Bu, and Q.D. Yang, Generalized bridging domain method for coupling finite elements with discrete elements, Computer Methods in Applied Mechanics and Engineering, 276 (509-533), 2014.

5. Q. D. Yang*, D. Schesser, M. Niess, P. Wright, M. Mavrogordato, I. Sinclair, S. M. Spearing, and B. N. Cox, “On crack initiation in notched, cross-plied polymer matrix composites”, Journal of the Mechanics and Physics of Solids, 78 (314-332). 2014.

6. C. X. Zhang, J. Z. Song, Q. D. Yang, “Periodic buckling patterns of graphene/hexagonal boron nitride heterostructure”, Nanotechnology, 25 (445401-10), 2014

7. Q. Xu, W.M. Tao, S.X. Qu*, Q. D. Yang, “A cohesive zone model for the elevated temperature interfacial debonding and frictional sliding behavior”, Composite Science and Technology, 110 (45-52), 2015

8. W. Liu, D. Schesser, Q. D. Yang and D.S. Ling, “A Consistency-Check Based Algorithm for Element Condensation in Augmented Finite Element Methods for Fracture Analysis”, Engineering Fracture Mechanics, 139 (78-97), 2015.

9. Y. C. Gu, J. Jung, Q. D. Yang, and W. Q. Chen, “A New Stabilizing Method for Numerical Analyses with Severe Local and Global Instability”, ASME Journal of Applied Mechanics, 82 (101010-1, -12), 2015

10. J. Jung, B. C. Do, and Q. D. Yang, “A-FEM for Arbitrary Cracking and Crack Interaction in Solids under Thermo-Mechanical Loadings”, Philosophical Transactions A. 374: 20150282.2016

11. G. Borstnar, M. N. Mavrogordato, Q. D. Yang, I. Sinclair, and S. M. Spearing, “Crack path simulation in a particle-toughened interlayer within a polymer composite laminate”, Composite Science & Technology 133 (89-96). 2016

12. A. Vanaerschot, B. N. Cox, S. V. Lomov, D. Vandepitte, “Multi-scale modelling strategy for textile composites based on stochastic reinforcement geometry,” Comput. Methods Appl. Mech. Engrg. 310 (906–934). 2016

13. M. Naderi, J. Jung, and Q. D. Yang, “A three-dimensional Augmented Finite Element for Modeling arbitrary cracking in solids”, International Journal of Fracture, 192 (147-168). 2016

14. J. Jung and Q. D. Yang, “A Two-Dimensional Augmented Finite Element for Dynamic Crack Initiation and Propagation”. International Journal of Fracture. 203 (41-61). 2017

15. G. D. Nian, Y. J. Shan, S.X. Qu, and Q. D. Yang, “Failure analysis of syntactic foams: a computational model with cohesive law and XFEM”, Composites Part B. 89 (18-26), 2016

16. B. N. Legarth and Q. D. Yang, “Micro-mechanical analyses of debonding and matrix cracking in dual-phase materials”, ASME Journal of Applied Mechanics, 83 (051006-1, -9), 2016

17. J. S. Hu, K. F. Zhang, Q.D. Yang, H. Cheng, Y. Yang, An experimental study on bearing response of single-lap

bolted composite interference-fit joints. In press, Composite: Part B. 2017

18. J.S. Hu, K. F. Zhang, Q. D. Yang, C. Hui, S. N. Liu, Y. Yang, Fretting behaviors of interface between CFRP and coated titanium alloy in composite interference-fit joints under service condition. In press, Materials & Design, 2017.

Manuscripts in Preparation:
19. Y.W. Xu, J. Jung, S. Nojavan, and Q.D. Yang, “An Orthotropic A-FEM for Progressive Damage Analyses of Laminar Composites with Explicit Presentation of All Major Damage Modes,” in preparation for possible submission to Composite A, 2017.

20. J. Quek and B. N. Cox, “Graph theory analysis of rich fiber-scale data opens a new route to high-fidelity simulations of damage evolution in composites,” in preparation for submission to JMPS, 2017.

21. Y.W. Xu, J. Jung, and Q. D. Yang, “Effects of fine scale nonlinearity on coupled delamination and ply cracking in laminated composites,” in preparation for possible submission to Composites & Structures, 2017.

22. Q.D. Yang, T. A. Parthasarathy, O. Sudre, B.N. Cox, “Coupled Binary Model (CDM) and Continuum Damage Model (CDM) for Failure Analysis of Textile CMC Structures Subject to Environmental Degradation, ” in presparation for possible submission to the Journal of American Ceramics Society. 2017.

23. Q.D. Yang, Y. H. Yang, O. Sudre, B.N. Cox, “Coupled Binary Model (CDM) and Continuum Damage Model (CDM) for Progressive Failure Analysis of Large Textile CMC Structures, ” in presparation for possible submission to the Journal of American Ceramics Society. 2017.

Honors and Awards: Nothing to Report

Protocol Activity Status:

Technology Transfer: • Key enabling capabilities of the A-FEM have been enriched and applied to several other governmental and industrial programs.
• Broad collaborations with national/international universities, research institutions, and industrial companies.

Details in Appendix C of the final report

PARTICIPANTS:

Participant Type: PD/PI
Participant: Qingda Yang
Person Months Worked: 8.00 **Funding Support:**
Project Contribution:
International Collaboration:
International Travel:
National Academy Member: N
Other Collaborators:

Participant Type: Consultant
Participant: Brian Cox
Person Months Worked: 4.00 **Funding Support:**
Project Contribution:
International Collaboration:
International Travel:
National Academy Member: N
Other Collaborators:

Participant Type: Postdoctoral (scholar, fellow or other postdoctoral position)
Participant: Jaedal Jung

Person Months Worked: 4.00 **Funding Support:**
Project Contribution:
International Collaboration:
International Travel:
National Academy Member: N
Other Collaborators:

Participant Type: Postdoctoral (scholar, fellow or other postdoctoral position)
Participant: Mehdi Naderi
Person Months Worked: 6.00 **Funding Support:**
Project Contribution:
International Collaboration:
International Travel:
National Academy Member: N
Other Collaborators:

Participant Type: Graduate Student (research assistant)
Participant: Briggitte Morales
Person Months Worked: 10.00 **Funding Support:**
Project Contribution:
International Collaboration:
International Travel:
National Academy Member: N
Other Collaborators:

Participant Type: Graduate Student (research assistant)
Participant: Yuhang Yang
Person Months Worked: 12.00 **Funding Support:**
Project Contribution:
International Collaboration:
International Travel:
National Academy Member: N
Other Collaborators:

Participant Type: Graduate Student (research assistant)
Participant: YunWei Xu
Person Months Worked: 12.00 **Funding Support:**
Project Contribution:
International Collaboration:
International Travel:
National Academy Member: N
Other Collaborators:

Participant Type: Other (specify)
Participant: Scott Floerke
Person Months Worked: 10.00 **Funding Support:**
Project Contribution:
International Collaboration:
International Travel:
National Academy Member: N
Other Collaborators:

Participant Type: Other (specify)

RPPR Final Report
as of 16-Oct-2017

Participant: James Robertson
Person Months Worked: 8.00 **Funding Support:**
Project Contribution:
International Collaboration:
International Travel:
National Academy Member: N
Other Collaborators:

ARTICLES:

Publication Type: Journal Article Peer Reviewed: Y **Publication Status:** 1-Published
Journal: International Journal for Numerical Methods in Engineering
Publication Identifier Type: DOI Publication Identifier: 10.1002/nme.4697
Volume: 0 Issue: 0 First Page #: 0
Date Submitted: Date Published:
Publication Location:
Article Title: An efficient augmented finite element method for arbitrary cracking and crack interaction in solids
Authors:
Keywords: A-FEM, crack interaction, cohesive zone models
Abstract: This paper presents an augmentation method that enables bilinear finite elements to efficiently and accurately account for arbitrary, multiple intra-elemental discontinuities in 2D solids. The augmented finite element method (A-FEM) employs four internal nodes to account for the crack displacements due to an intra-elemental weak or strong discontinuity, and it permits repeated elemental augmentation to include multiple interactive cracks. It thus enables a unified treatment of damage evolution from a weak discontinuity to a strong discontinuity, and to multiple interactive cohesive cracks, all within a single bilinear element that employs standard external nodal DoFs only. A novel elemental condensation procedure has been developed to solve the internal nodal DoFs as functions of the external nodal DoFs for any irreversible, piece-wise linear cohesive laws. It leads to a fully condensed elemental equilibrium equation with mathematical exactness, eliminating the need for nonlinear equil
Distribution Statement: 1-Approved for public release; distribution is unlimited.
Acknowledged Federal Support:

Publication Type: Journal Article Peer Reviewed: Y **Publication Status:** 1-Published
Journal: Computer Methods in Applied Mechanics and Engineering
Publication Identifier Type: DOI Publication Identifier: 10.1016/j.cma.2014.03.023
Volume: 276 Issue: 0 First Page #: 0
Date Submitted: Date Published:
Publication Location:
Article Title: Generalized bridging domain method for coupling finite elements with discrete elements
Authors:
Keywords: Discrete element method; Finite element method; Multiscale method; Spurious wave reflection; Granular flow phenomenon
Abstract: The concurrent coupling of finite elements and discrete elements is an effective DOF reduction methodology for reproducing the granular flow phenomenon as discrete element method does. In this paper, we present a novel coupling strategy named the generalized bridging domain method. This method introduces independent functions to weight the material properties of the continuum and those of the discrete element model, and then the equilibrium of each new model is guaranteed by imposing compensation forces. The compensation force of continuum is determined by force and displacement compatibility requirements of continuum with respect to discrete elements, and vice versa. Utilizing different weighting functions, four typical coupling methods, the bridging domain method, edge-to-edge coupling, separate domain coupling, and separate edge coupling, are obtained. Additionally, a new integration algorithm with multiple time steps is developed for the separate edge coupling. The numerical perfor
Distribution Statement: 1-Approved for public release; distribution is unlimited.
Acknowledged Federal Support:

RPPR Final Report
as of 16-Oct-2017

Publication Type: Journal Article Peer Reviewed: Y **Publication Status:** 1-Published
Journal: International Journal for Numerical Methods in Engineering
Publication Identifier Type: DOI Publication Identifier: 10.1002/nme.4689
Volume: 99 Issue: 7 First Page #: 0
Date Submitted: Date Published:
Publication Location:
Article Title: A finite element method with mesh-separation-based approximation technique and its application in modeling crack propagation with adaptive mesh refinement
Authors:
Keywords: FEM; approximation technique; discontinuity; hanging node; adaptive mesh refinement
Abstract: This paper presents a FEM with mesh-separation-based approximation technique that separates a standard element into three geometrically independent elements. A dual mapping scheme is introduced to couple them seamlessly and to derive the element approximation. The novel technique makes it very easy for mesh generation of problems with complex or solution-dependent, varying geometry. It offers a flexible way to construct displacement approximations and provides a unified framework for the FEM to enjoy some of the key advantages of the Hansbo and Hansbo method, the meshfree methods, the semi-analytical FEMs, and the smoothed FEM. For problems with evolving discontinuities, the method enables the devising of an efficient crack-tip adaptive mesh refinement strategy to improve the accuracy of crack-tip fields. Both the discontinuities due to intra-element cracking and the incompatibility due to hanging nodes resulted from the element refinement can be treated at the elemental level. The eff
Distribution Statement: 1-Approved for public release; distribution is unlimited.
Acknowledged Federal Support:

DISSERTATIONS:

Publication Type: Thesis or Dissertation
Institution: University of Miami
Date Received: 03-Oct-2017 Completion Date: 5/15/15 4:00AM
Title: UNIFIED COHESIVE ZONE MODEL FOR DAMAGE MODELING DUE TO CYCLIC LOADING
Authors: Derek Schesser
Acknowledged Federal Support: **N**

Publication Type: Thesis or Dissertation
Institution: University of Miami
Date Received: 03-Oct-2017 Completion Date: 5/15/15 4:00AM
Title: UNIFIED COHESIVE ZONE MODEL FOR DAMAGE MODELING DUE TO CYCLIC LOADING
Authors: Derek Schesser
Acknowledged Federal Support: **N**

Publication Type: Thesis or Dissertation
Institution: University of Miami
Date Received: 03-Oct-2017 Completion Date: 5/15/17 4:00AM
Title: MODELING OF A FIBER TOW FOR COMPOSITES FAILURE ANALYSIS
Authors: James Robertson
Acknowledged Federal Support: **N**

Publication Type: Thesis or Dissertation
Institution: University of Miami
Date Received: 03-Oct-2017 Completion Date: 6/15/17 4:00AM
Title: Calibration and Comparison of the CONWEP Model with the ALE Method for Simulating Response of Aluminum 2024-T3 to C4 Blast
Authors: Scott Floerke
Acknowledged Federal Support: **N**

Publication Type: Thesis or Dissertation
Institution: University of Miami
Date Received: 03-Oct-2017 Completion Date: 6/15/17 4:00AM
Title: Calibration and Comparison of the CONWEP Model with the ALE Method for Simulating Response of Aluminum 2024-T3 to C4 Blast
Authors: Scott Floerke
Acknowledged Federal Support: **N**

FINAL REPORT

AUGMENTED FINITE ELEMENT METHOD FOR HIGH-FIDELITY ANALYSIS OF STRUCTURE COMPOSITES

ARO Prime Contract Number: W911NF-13-1-0211

The University of Miami DOC Number: 661581

Prepared by:

Prof. Qingda Yang
Department of Mechanical and Aerospace Engineering
The University of Miami
1251 Memorial Drive
Coral Gables, FL 33124

Prepared for:

Dr. Ralph A. Anthenien
Mechanical Sciences Division
U.S. Army Research Office
P.O. Box 12211
Research Triangle Park, NC 27709-2211

September, 2017

REPORT DOCUMENTATION PAGE

Form Approved
OMB No. 0704-0188

1. REPORT DATE *(DD-MM-YYYY)*	2. REPORT TYPE	3. DATES COVERED *(From - To)*
09/28/2017	Final Report	07/15/2013-07/14/2017

4. TITLE AND SUBTITLE
Augmented Finite Element Method for High-Fidelity Analysis of Structural Composites

5a. CONTRACT NUMBER

5b. GRANT NUMBER
W911NF-13-1-0211

5c. PROGRAM ELEMENT NUMBER

6. AUTHOR(S)
Qingda Yang

5d. PROJECT NUMBER

5e. TASK NUMBER

5f. WORK UNIT NUMBER

7. PERFORMING ORGANIZATION NAME(S) AND ADDRESS(ES)
Department Mechanical & Aerospace Engineering
The University of Miami
Coral Gables, FL 33124

8. PERFORMING ORGANIZATION REPORT NUMBER
661581

9. SPONSORING / MONITORING AGENCY NAME(S) AND ADDRESS(ES)
Mechanical Sciences Division
U.S. Army Research Office
P.O. Box 12211
Research Triangular Park
NC 27709-2211

10. SPONSOR/MONITOR'S ACRONYM(S)
US ARO

11. SPONSOR/MONITOR'S REPORT NUMBER(S)

12. DISTRIBUTION / AVAILABILITY STATEMENT
Approved for public release; distribution unlimited.

13. SUPPLEMENTARY NOTES
The views, opinions and/or findings contained in this report are those of the author(s) and should not be construed as an official Department of the Army position, policy or decision, unless so designated by other documentation

14. ABSTRACT
This report documents the development of a new augmented finite element method (A-FEM) that enables efficient and accurate treatment of arbitrary, multiple intra-elemental discontinuities in composite materials with complex microstructures. A novel consistency-check based algorithm for element condensation has been invented and it demonstrated orders-of-magnitude improvement in numerical efficiency, accuracy, and robustness. The new A-FEM's high-fidelity simulation capabilities to interactive cohesive crack formation and propagation in homogeneous and heterogeneous solids have been demonstrated through detailed modeling of the progressive damage processes in composites at various material and structural scales. The proposed goal of "developing an efficient and accurate multiscale computational methodology for rapid virtual testing of composites with complex microstructures" has thus been fully achieved and demonstrated.

15. SUBJECT TERMS
Augmented finite element method, Composites, Failure Analysis, Cohesive Zone Models

16. SECURITY CLASSIFICATION OF:			17. LIMITATION OF ABSTRACT	18. NUMBER OF PAGES	19a. NAME OF RESPONSIBLE PERSON
					Qingda Yang
a. REPORT	b. ABSTRACT	c. THIS PAGE			19b. TELEPHONE NUMBER *(include area code)*
U	U	U	UU	61	305-284-3221

TABLE OF CONTENTS

AUGMENTED FINITE ELEMENT METHOD FOR HIGH-FIDELITY ANALYSIS OF STRUCTURE COMPOSITES (FINAL REPORT)

EXECUTIVE SUMMARY

The proposed objective of this study, according to the original propose, is to develop "an efficient and accurate multiscale computational methodology for rapid virtual testing of composites with complex microstructures". The proposed research goals are:

"1) Development of new 2D and 3D A-FEM elements that can explicitly account for statistical material heterogeneity and can faithfully predict progressive damage initiation, propagation and multi-crack interaction";

"2) Apply the new method to study composites of interest to the Army, coupled with 3D μCT-based precision experiments, to understand key physical phenomena of crack formation and growth, and to quantify their direct effects on structural integrity under general loads";

Two more goals were added in the 4th year extension proposal in view of the importance of material nonlinearity due to finer scale (micron- or submicron scale) material damage,

"3) Complete the development of a 'multi-physics' nonlinear element within the AFEM framework that will allow us to represent a microcrack in a heterogeneous medium";

"4) Verify the ability of the multi-physics element to make correct predictions of the conditions for crack deflection, bifurcation, and branching and of the influence on these phenomena of fine-scale continuum damage in the surrounding material".

All these objectives have been met. Here we highlight the key achievements with more details given in the main body of this final report.

Major Technical Achievements:

- A new augmentation formulation that enables standard finite element method to deal with strong and weak discontinuities caused by arbitrary, coupled multiple damage formation and propagation in complex heterogeneous, without the need for adding extra DoFs into the global problem.
- A novel elemental condensation procedure (consistency-check based algorithm) that demonstrated 2-3 orders of magnitude improvement in numerical efficiency, accuracy, and robustness.
- A novel inertia-based stabilizing method that guarantees unconditional convergence and allows for smooth transition from quasi-static crack development to rapid or even dynamic crack propagation, and vice versa.
- A nonlinear A-FEM to account for both finer scale (i.e. submicron scale) continuum damage or plasticity and larger scale nonlinearity due to nonlinear coupling of multiple cracks.
- Extended the new A-FEM with coupled thermal-mechanical analysis capabilities under static, cyclic, and dynamic loading conditions.
- Much improved understanding of the interaction of multiple damage modes in composites and their convoluted influence on structural integrity through comparing/correlating detailed A-FEM analysis results against high resolution experimental measurements/characterizations (DIC, micro-CT, etc)
- 18 published/accepted journal publications and 5 more in preparation (***Appendix A***).

Collaborations and Technology Transfer (Appendix C)

- Key enabling capabilities of the A-FEM have been enriched and applied to several other governmental and industrial programs.
- Broad collaborations with national/international universities, research institutions, and industrial companies.

Graduate Students Involved During Reporting Period (Appendix B)

- This project benefitted 4 PhD students, 2 MS students, and 2 post-doctorate researchers

1. BACKGROUND OVERVIEW

Composite materials are now widely used in many key areas such as aerospace, defense, renewable energy, and off-shore engineering. Recent high profile examples include the Boeing 787 dream-liners, ultra-light weight composite blades for wind mills, and multilayer FRPC-steel pipelines for deep-sea oil transportation. Multiscale hierarchical microstructures are usually integrated into such structures to achieve multi-functional purposes and/or to further gain the weight-savings. Key advantages of composites over the traditional structural metal and metal alloys include significant weight savings, better reliability and durability, and lower manufacturing and maintenance costs. In particular, composite engineering offers the exciting possibility to design the hierarchical features in micro- or meso-scale to achieve the desired structural performance through optimization process [1-3].

However, due to the relatively short history of composite usage as primary load-bearing structural components, the current knowledge base remains inadequate for confident design of safe and durable composite structures. The safety and durability uncertainty of composite structures remains high and damage tolerance analysis must be considered as an integral part in the composite structural design process. However, unlike structural metals which are homogeneous and isotropic, composites are inherently inhomogeneous and anisotropic. Microscopic flaws and imperfections are inevitably present in these materials due to manufacturing processes. Currently the damage tolerance and durability design relies heavily on large experimental test programs that are extremely costly and time consuming. High-fidelity simulation capabilities that can potentially offer efficient and accurate strength and durability predictions based on constituent materials properties can greatly reduce the costly experimental inputs. However, accurate estimation/prediction of composite strength at structural scale remains elusive despite decades of intensive research [4-6].

It proves very changing to faithfully predict the ultimate strength of composites due to the fact that almost all composites exhibit complex progressive damage evolution phenomena before complete failure. For example, a composite laminate will typically develop non-critical intra-ply cracks (transverse cracks in off-axial plies and longitudinal splits in 0^0-plies) far below the ultimate load, which facilitate local delaminations between neighboring plies. These damage processes continuously evolve in a nonlinearly coupled manner and eventually lead to the formation of large delaminations, which in turn cause significant fiber breakage in primary load bearing plies and lead to ultimate structural failure [7, 8]. While it is desired from damage tolerance point of view, predicting such progressive damage evolution up to ultimate failure proves to be very challenging.

Thanks to recent development in numerical modeling methods and high-resolution experimental characterization, significant advances in composite strength prediction, especially in continuous fiber reinforced composite laminates, have been made in the past decade [1, 2, 9, 10]. This was enabled by 1) the development of advanced finite element methods (FEMs) including the extended finite element method (X-FEM, e.g. [11-14]), Phantom node method (PNM) (e.g. [15-17]), and the PNM-based augmented finite element method (PNM-based A-FEM, e.g. [18-21], and 2) the nonlinear cohesive zone models (CZMs) for discrete fracture events in composites (e.g. [22-28]. The key is to embed CZM descriptions for major damage modes into the advanced FEM formulations so that the discrete cracking events can be initiated and propagated at the locations determined by local stresses in response to external loads. For a more comprehensive review of

the recent advances and the remaining outstanding numerical and material issues associated with such progressive damage modeling in composite laminates, the readers are referred to the recent review article by Van de Meer [9].

It has been generally recognized that, to achieve high-fidelity predictions of the progressive failure processes in structural composites, several key elements have to be considered simultaneously in the numerical framework: 1) a numerical model should allow for crack/discontinuity initiation from a pristine continuum at locations determined by local stress environments; 2) carefully calibrated cohesive laws for crack/discontinuity evolution and propagation; 3) crack/discontinuity initiation criteria that account for the constraining effects from neighboring plies (in-situ strength, e.g. [29, 30]); and 4) correct representation of the shear nonlinearity at ply level [20, 25, 31]; 4) special numerical treatment is needed to correctly account for the coupling between the cracked ply elements and the interfacial cohesive elements (otherwise correct stress transfer is not always guaranteed and numerical stress locking may occur [32-34]); and 5) a computationally efficient algorithm that can track all individual cracks and their nonlinear coupling, preferably without the need to introduce additional DoFs (The additional DoFs in X-FEM and PNM-FEM are specific to a single crack and they become problematic when multiple crack merge or a single crack branches into multiple cracks).

Further, in textile composites the material heterogeneity issue of composites cannot be resolved adequately by mainstream formulations of conventional materials/structures modeling, owing to the complex interaction between fiber reinforcement architecture and constituent material heterogeneity, which are on the same scale as that of the features of the structures. This negates the common strategy of homogenizing the material properties in simulations. The heterogeneity arises from the distinct fiber tows in the textile, which are strongly anisotropic and their shapes may be significantly distorted due to manufacturing process. The tows are typically ~ 0.1 – 1 mm in lateral dimension, which is of the same order of the panel thickness (1~ 10 mm). Furthermore, the interlacing pattern of an integral textile structure, which has profound impact on the elastic properties and failure strength [35-37], can be quite complex, involving many hundreds of geometrically dissimilar tow segments or local tow arrangements. The structure will generally be subject to non-periodic mechanical and thermal loads, including spatial and temporal peaks. In a piece of structure of relevant size, it remains a serious challenge to develop a mesh that deals with the interlacing architecture, the heterogeneity of the tows, and general loads, while maintaining computational tractability. Strength prediction is even more challenging: the randomly distributed matrix-rich pockets have to be explicitly considered because they are susceptible to microcrack formation at relatively small loads. The complex coupling of all the nonlinear processes associated with crack nucleation, bifurcation and deflection must be adequately captured.

The above challenges require the establishment of numerical modeling platforms that can deal with not only the arbitrary cracking issue, but also the issue of arbitrary crack interaction such as crack merging and crack bifurcation, again, without any *a priori* knowledge of the locations and load levels at which such events should happen. Unfortunately, the above mentioned advanced numerical methods (X-FEM, PNM-based A-FEM) are all very inflexible in dealing with multiple crack merging or bifurcation. This is because, in these methods each individual crack requires its own additional copy of degree of freedoms (DoFs) (X-FEM) or extra node copies (PNM-based A-FEM) to describe the discontinuous displacement field associated with it. Tracing the evolution of complex fracture surfaces of multiple cracks quickly becomes extremely tedious and numerically

burdensome because, in such cases, there are no effective tracking algorithms that can judiciously assign different copies of DoFs or nodes to different cracks for complex crack configurations.

It is therefore beneficial to seek numerical methods that can account for arbitrary discontinuities and their nonlinear interactions with less numerical burden for tracing complex crack surfaces. In this regard, there are mainly two methods to reduce or eliminate the need for additional DoFs or nodes. One method is the phase-field method [38-40]. This method introduces an additional nodal DoF to approximate a fracture surface with a highly concentrated yet continuous phase-field, which smoothes the boundary of the crack over a small region. The major advantage is that the evolution of the fracture surfaces follows from the solution of a coupled system of partial differential equations. Thus, it does not require the fracture surfaces to be tracked algorithmically. However, this method is mesh-dependent and it requires an extremely fine mesh to resolve the sharp discontinuity associated with an interface or a crack surface. The computational cost remains extremely high. There are also serious ambiguities regarding the non-zero stresses at crack wake surfaces.

Another approach is the embedded discontinuity method. This method follows the earlier work in smeared localization models and enhanced strain methods [41-46] and it has been extended to account for discrete discontinuities by several research groups [47-54] following Simo and colleagues' seminal approach in treating plastic strain localizations with discrete discontinuous descriptions [55, 56]. Special (or regularized) shape functions are used to account for the discontinuous crack displacements within an element [50, 51, 53, 56]. However, the special shape functions have to be carefully constructed so that the orthogonal principle is satisfied. Otherwise, spurious deformation modes or serious stress locking may occur [54, 55]. Furthermore, the ability of this approach in handling interactive cracks is limited -- thus far there is no report on regularized shape functions that can descript multiple discontinuities within a single element.

Thus the main focus of this study is to develop new finite element methods that can deal with discrete cracks without the need of introducing additional DoFs or nodes, so that the numerical burden for tracing crack surfaces can be minimized. During the proposed research period, we have formulated and implemented a novel A-FEM formulation *that can treat multiple intra-element cohesive cracks in homogeneous or heterogeneous solids, without the need to introduce any extra DoFs*. In the new A-FEM formulation four internal nodes with regular displacement DoFs were introduced to account for a cohesive crack, so that the crack displacements are natural outcomes from element equilibrium consideration. Thus it does not need to assume the deformation modes *a priori* for crack displacements as in the enhanced strain method or in many of the embedded discontinuity methods. More importantly, we demonstrated the new A-FEM can account for 1) intra-element material heterogeneity which involves a natural evolution from a weak discontinuity to a strong one, and 2) repeated elemental augmentation to enable multiple, interactive intra-element discontinuities to account for crack merging (from a bulk material domain into a material interface) or crack bifurcation away from the interface. In addition, we report a novel and efficient solving algorithm for elemental condensation that provides analytical solutions to the local equilibrium equations with embedded piece-wise linear cohesive crack like discontinuities. It will be demonstrated that the new A-FEM with the help of the new condensation algorithm can provide orders of magnitude improvement in numerical efficiency, accuracy and robustness [21, 57].

2. PROBLEM STATEMENT

2.1 Strong and Weak Form

Consider a discontinuous physical domain Ω as shown in Figure 1. The domain is composed of two sub-domains of the same or different materials, *i. e.*, $\Omega = \Omega^+ \cup \Omega^-$. The two domains are connected by a discontinuity which could be a cohesive crack or a material boundary, $\Gamma_c = \Gamma_c^{\ +} \cup \Gamma_c^{\ -}$.[1] The prescribed tractions $\boldsymbol{f}$ are imposed on boundary Γ_F and the prescribed displacements $\bar{\boldsymbol{u}}$ on boundary Γ_u. The stress field inside the domain, $\boldsymbol{\sigma}$, is related to the external loading $\boldsymbol{f}$. The strong form of the equilibrium equations and boundary conditions are:

$$
\begin{array}{llll}
\nabla \cdot \boldsymbol{\sigma}^+ = 0 & (\text{in } \Omega^+); & \nabla \cdot \boldsymbol{\sigma}^- = 0 & (\text{in } \Omega^-) \\
\boldsymbol{\sigma}^+ \cdot \mathbf{n}^+ = \mathbf{f}^+ & (\text{on } \Gamma_F^{\ +}) & \boldsymbol{\sigma}^- \cdot \mathbf{n}^- = \mathbf{f}^- & (\text{on } \Gamma_F^{\ -}) \\
\mathbf{u}^+ = \bar{\mathbf{u}}^+ & (\text{on } \Gamma_u^{\ +}) & \mathbf{u}^- = \bar{\mathbf{u}}^- & (\text{on } \Gamma_u^{\ -}) \\
\mathbf{t}^+ = \boldsymbol{\sigma}^+ \cdot \mathbf{n}^+ = -\mathbf{t} & (\text{on } \Gamma_c^{\ +}) & \mathbf{t}^- = \boldsymbol{\sigma}^- \cdot \mathbf{n}^- = \mathbf{t} & (\text{on } \Gamma_c^{\ -})
\end{array}
\qquad (1)
$$

where $\boldsymbol{\sigma}^+$ and $\boldsymbol{\sigma}^-$ are the stresses in the subdomains Ω^+ and Ω^-, respectively; $\mathbf{t}^+$ and $\mathbf{t}^-$ are the tractions along the discontinuity surfaces $\Gamma_c^{\ +}$ and $\Gamma_c^{\ -}$, respectively; $\mathbf{n}^+$ and $\mathbf{n}^-$ are the outward normal of $\Gamma_c^{\ +}$ and $\Gamma_c^{\ -}$, respectively. The last two expressions in Eqn (1) come from the stress continuity across the discontinuity. The traction, $\mathbf{t}$, is a function of the relative displacements, $\boldsymbol{\Delta}\mathbf{u}$, between $\Gamma_c^{\ +}$ and $\Gamma_c^{\ -}$, i.e.,

$$
\begin{array}{ll}
\mathbf{t} = \mathbf{t}(\boldsymbol{\Delta}\mathbf{u}) & (\text{on } \Gamma_c) \\
\boldsymbol{\Delta}\mathbf{u} = \mathbf{u}^+ - \mathbf{u}^- & (\text{on } \Gamma_c)
\end{array}
\qquad (2)
$$

where $\mathbf{u}^+$ and $\mathbf{u}^-$ are the displacement fields in Ω^+ and Ω^-, respectively. Eqn (2) serves as the constitutive law and kinematic equation of the discontinuity. In this study, cohesive zone models with piece-wise linear traction-separation laws were used to describe strong discontinuities.

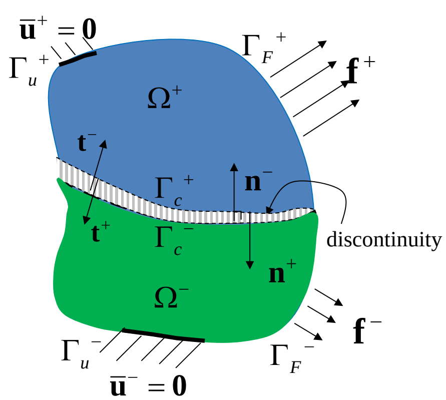

Figure 1: Notation for an elastic body with a discontinuity

[1] For a weak discontinuity $\Gamma_c^{\ +} = \Gamma_c^{\ -}$ while for a strong discontinuity $\Gamma_c^{\ +}$ and $\Gamma_c^{\ -}$ are separated.

The domain surrounding the discontinuity is assumed to be elastic. We further assume small strains and displacements condition. Thus the constitutive law and kinematic equations for the two domains can be written as:

$$\begin{array}{ll} \boldsymbol{\sigma}^{+} = \mathbf{C}^{+} : \boldsymbol{\varepsilon}^{+} \quad (\text{in } \Omega^{+}); & \boldsymbol{\sigma}^{-} = \mathbf{C}^{-} : \boldsymbol{\varepsilon}^{-} \quad (\text{in } \Omega^{-}) \\ \boldsymbol{\varepsilon}^{+} = [\nabla \mathbf{u}^{+} + (\nabla \mathbf{u}^{+})^{\mathbf{T}}]/2 \quad (\text{in } \Omega^{+}); & \boldsymbol{\varepsilon}^{-} = [\nabla \mathbf{u}^{-} + (\nabla \mathbf{u}^{-})^{\mathbf{T}}]/2 \quad (\text{in } \Omega^{-}) \end{array} \tag{3}$$

where $\mathbf{C}^{+}$ and $\mathbf{C}^{-}$ are the material stiffness tensors of the two sub-domains traversed by the discontinuity, respectively. They can be of isotropic or orthotropic. The superscript $(\cdot)^{\mathbf{T}}$ denotes transposition.

The above strong form of the problem can be converted into a weak form using the principle of virtual work. The displacement fields ($\mathbf{u}^{+}$ and $\mathbf{u}^{-}$) must be sub-sets of the kinematically admissible displacement fields, $\mathbb{U}$:

$$\mathbf{u}^{+} \in \mathbb{U} = \{\mathbf{v}^{+} \in \mathbb{V} : \mathbf{v}^{+} = \bar{\mathbf{u}}^{+} \quad \text{on } \Gamma_{u}{}^{+}\}; \ \mathbf{u}^{-} \in \mathbb{U} = \{\mathbf{v}^{-} \in \mathbb{V} : \mathbf{v}^{-} = \bar{\mathbf{u}}^{-} \quad \text{on } \Gamma_{u}{}^{-}\}. \tag{4}$$

Applying the principle of virtual work separately to the subdomains, the weak forms can be written as

$$\begin{cases} \int_{\Omega^{+}} \boldsymbol{\sigma}^{+} : \boldsymbol{\varepsilon}^{+}(\mathbf{v}^{+}) \, \mathrm{d}\Omega = \int_{\Gamma_{F}{}^{+}} \mathbf{F}^{+} \cdot \mathbf{v}^{+} \, \mathrm{d}\Gamma - \int_{\Gamma_{c}} \mathbf{t}(\Delta \mathbf{v}) \cdot \mathbf{v}^{+} \, \mathrm{d}\Gamma \\ \int_{\Omega^{-}} \boldsymbol{\sigma}^{-} : \boldsymbol{\varepsilon}^{-}(\mathbf{v}^{-}) \, \mathrm{d}\Omega = \int_{\Gamma_{F}{}^{-}} \mathbf{F}^{-} \cdot \mathbf{v}^{-} \, \mathrm{d}\Gamma + \int_{\Gamma_{c}} \mathbf{t}(\Delta \mathbf{v}) \cdot \mathbf{v}^{-} \, \mathrm{d}\Gamma \end{cases} \qquad \forall (\mathbf{v}^{+}, \mathbf{v}^{-}) \in \mathbb{U} \tag{5}$$

where $\boldsymbol{\Delta}\mathbf{v} = \mathbf{v}^{+} - \mathbf{v}^{-} \quad (\text{on } \Gamma_{c})$. The left-hand-sides are the internal virtual work and the right-hand-sides are the virtual work done by the external forces and the tractions along the crack surfaces. Note that, if one of the subdomains (say Ω^{-}) further cracks, the principle of virtual work can be applied to all three subdomains without any further modifications.

2.2. Piece-wise Linear Cohesive Laws

The discontinuity in section 2.1 is often modeled by cohesive laws that provide explicit traction-separation relations. Any nonlinear cohesive laws can be approximated with piece-wise linear laws as shown in Figure 2. The cohesive law employs separate mode I and mode II traction-separation relations and it was first proposed by Yang, Thouless and colleagues [22, 58-60]. For those cohesive laws employing coupled mode I and mode II relation as in [24, 26], the piece-wise linear form of the traction-separation laws can be obtained with an incremental form.

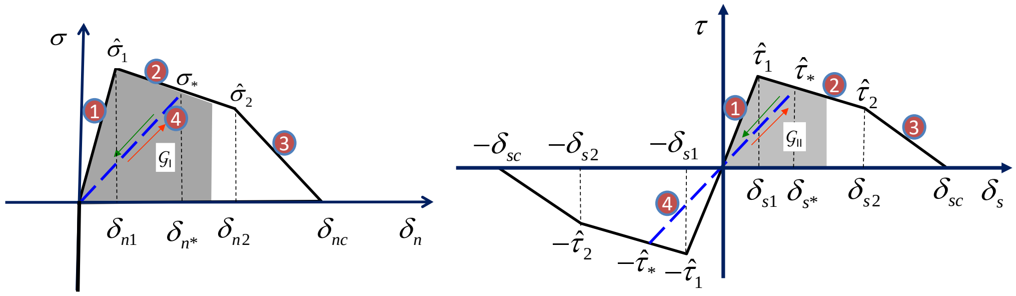

(a) mode I (b) mode II

Figure 2 A mixed mode Piece-wise linear cohesive law with (a) mode I and (b) mode II traction separation relations.

For the piece-wise linearized models, it is advantageous to index the traction-separation laws by cohesive segment numbers as labeled in Figure 2 by the circled numbers. Each segment is characterized by a critical stress ($\hat{\tau}^{(i)}$ or $\hat{\sigma}^{(j)}$), a corresponding local crack displacement ($\delta_s^{(i)}$ or $\delta_{\rm n}^{(j)}$), and a constant stiffness ($\alpha_s^{(i)}$ or $\alpha_n^{(j)}$). Here the superscripts (i) and (j) (i, j = 1, 2, and 3) are free indices for the cohesive segments with constant stiffness. For the cohesive model shown in Figure 2,

$$\hat{\sigma}^{(1)} = \hat{\sigma}_1;\ \hat{\sigma}^{(2)} = \hat{\sigma}_2;\ \hat{\sigma}^{(3)} = 0;\ \hat{\tau}^{(1)} = \hat{\tau}_1;\ \hat{\tau}^{(2)} = \hat{\tau}_2;\ \hat{\tau}^{(3)} = 0\,. \tag{6}$$

$$\delta_n^{(1)} = \delta_{n1};\ \delta_n^{(2)} = \delta_{n2};\ \delta_n^{(3)} = \delta_{nc};\ \ \delta_s^{(1)} = \delta_{s1};\ \delta_s^{(2)} = \delta_{s2};\ \delta_s^{(3)} = \delta_{sc}\,. \tag{7}$$

And the constant cohesive slopes for any segments are:

$$\alpha_s^{(i)} = (\hat{\tau}^{(i)} - \hat{\tau}^{(i-1)})/(\delta_s^{(i)} - \delta_s^{(i-1)});\ \alpha_n^{(j)} = (\hat{\sigma}^{(j)} - \hat{\sigma}^{(j-1)})/(\delta_n^{(j)} - \delta_n^{(j-1)})\ \ (i, j = 1,2,3)\,, \tag{8}$$

where $\hat{\sigma}^{(0)} = \hat{\tau}^{(0)} = 0$ and $\delta_n^{(0)} = \delta_s^{(0)} = 0$. Further, the crack displacement ranges consistent with the cohesive segments are indexed with

$$\overleftrightarrow{\delta}_s^{(i)} = \left(\delta_s^{(i-1)}, \delta_s^{(i)}\right]; \qquad \overleftrightarrow{\delta}_n^{(j)} = \left(\delta_n^{(j-1)}, \delta_n^{(j)}\right] \qquad (i, j = 1,2,3) \tag{9}$$

Thus the linearized relation between the cohesive stresses, $\sigma(\delta_n)$ and $\tau(\delta_s)$, and the crack displacements, δ_n and δ_s, for any segments may be written as:

$$\begin{aligned} &\tau(\delta_s) = \mathrm{sgn}(\delta_s)\left[\hat{\tau}^{(i-1)} + \alpha_s^{(i)}\left(\left|\delta_s\right| - \delta_s^{(i-1)}\right)\right] && (\text{for } \left|\delta_s\right| \in \overleftrightarrow{\delta}_s^{(i)}\ \&\&\ \left|\delta_s\right| \geq \delta_{s*}) \\ &\sigma(\delta_n) = \hat{\sigma}^{(j-1)} + \alpha_n^{(j)}(\delta_n - \delta_n^{(j-1)}) && (\text{for } \delta_n \in \overleftrightarrow{\delta}_n^{(j)}\ \&\&\ \delta_n \geq \delta_{n*}\ ) \end{aligned} \tag{10}$$

where the sign function $\mathrm{sgn}(\bullet)$ is defined as $\mathrm{sgn}(\bullet)=\begin{Bmatrix}1 & \text{if } \bullet>0 \\ 0 & \text{if } \bullet=0 \\ -1 & \text{if } \bullet<0\end{Bmatrix}$. $|\bullet|$ denotes taking the absolute value of the argument. δ_{s*} and δ_{n*} are two solution-dependent variables related to the irreversibility of the cohesive model, as discussed below.

The irreversibility of the cohesive model was explicitly considered by an additional unloading segment in each traction-separation law (segment 4 in Figure 2). In this paper, the maximum crack displacements ever reached, δ_{n*} for mode I and δ_{s*} for mode II as shown in Figure 2, were used as the historical (or, solution-dependent) variables to facilitate distinguishing between loading and unloading path, i.e., unloading occurs when the current crack displacements are smaller than the respective historical displacements. The corresponding historical cohesive stresses, $\hat{\sigma}_*$ and $\hat{\tau}_*$, were computed from these historical crack displacements using Eqn (10). Thus for segment *i* or *j* = 4, the cohesive stress – crack displacement relation is

$$\begin{aligned}&\tau(\delta_s)=\mathrm{sgn}(\delta_s)\alpha_s^{(4)}|\delta_s|; && (\text{for } |\delta_s|\in\overleftrightarrow{\delta}_s^{(4)} \ \&\& \ |\delta_s|<\delta_{s*})\\ &\sigma(\delta_n)=\alpha_n^{(4)}\delta_n && (\text{for } \delta_n\in\overleftrightarrow{\delta}_n^{(4)} \ \&\& \ \delta_n<\delta_{n*})\end{aligned} \tag{11}$$

The cohesive stiffnesses and the displacement ranges are

$$\begin{aligned}&\alpha_s^{(4)}=(\hat{\tau}_*/\delta_{s*}); && \alpha_n^{(4)}=(\hat{\sigma}_*/\delta_{n*})\\ &\overleftrightarrow{\delta}_s^{(4)}=[0,\delta_{s*}]; && \overleftrightarrow{\delta}_n^{(4)}=[-\infty,\delta_{n*}]\end{aligned} \tag{12}$$

For other cohesive laws such cohesive segments may be constructed similarly after piece-wise linearization.

Based on the individual modes, a mixed-mode cohesive model can be constructed by recognizing that the total traction-separation work absorbed during fracture, $\mathcal{G}$, can be separated into the mode I and mode II components, $\mathcal{G}_{\mathrm{I}}$ and $\mathcal{G}_{\mathrm{II}}$, so that,

$$\mathcal{G}=\mathcal{G}_{\mathrm{I}}+\mathcal{G}_{\mathrm{II}}\,. \tag{13}$$

The two separate components can be calculated by integration of the mode-I and mode-II traction-separation curves (Fig. 2):

$$\begin{aligned}\mathcal{G}_{\mathrm{I}}&=\int_0^{\delta_{\mathrm{n}}}\sigma(\delta)\,\mathrm{d}\delta\\ \mathcal{G}_{\mathrm{II}}&=\int_0^{\delta_{\mathrm{s}}}\tau(\delta)\,\mathrm{d}\delta\end{aligned} \tag{14}$$

Note that δ_{n} and δ_{s} are not independent parameters; they evolve together as a natural result of the interplay between the deformation of two joined domains and the details of the two pure-

mode traction-separation laws. A failure criterion is required to determine the critical values of the two components of $\mathcal{G}$, $\mathcal{G}_{\mathrm{I}}^{*}$ and $\mathcal{G}_{\mathrm{II}}^{*}$ (shaded areas in Figure 2), at which complete fracture of the cohesive zone occurs. The criterion used in this study is a simple one from [61]

$$\mathcal{G}_{\mathrm{I}}^{*}/\Gamma_{\mathrm{I}}+\mathcal{G}_{\mathrm{II}}^{*}/\Gamma_{\mathrm{II}}=1 \tag{15}$$

where Γ_{I} and Γ_{II} are the <u>total</u> areas under the pure mode I and pure mode II cohesive laws. They are the mode I and mode II fracture toughnesses in the linear-elastic-fracture-mechanics (LEFM) context.

A more detailed account of this mixed-mode cohesive zone model can be found in [23, 59, 60]. The major advantage of this cohesive law is that there is no need to specify the mode mixedness *a priori*. The mode mixedness and the mixed-mode toughness evolve as numerical outcomes of the local equilibrium of stresses. More importantly, this law guarantees correct mode mixedness when LEFM conditions are satisfied [34, 62, 63].

3. A NEW 2-D A-FEM FORMULATION

3.1 A-FEM Formulation with Single Intra-Elemental Crack

Without the loss of generality, the 4-node, quadrilateral plane element is used here to illustrate the augmented finite element scheme. The physical element with regular or external nodes 1, 2, 3, and 4 is severed by a cohesive crack or a bi-material interface as shown in Figure 3. We take a common approach that assumes: 1) during crack growth, a crack tip always resides at an element boundary during its propagation as in the phantom node method and the alike [18, 20, 64, 65], and 2) the existence of a cohesive zone eliminates the crack-tip singularity [22, 23, 66-68]. Thus the method proposed here cannot treat cracks with crack-tip singularities as can be conveniently done in the X-FEM framework. However, for many engineering materials that fail by the development of finite damage process zones (i.e., polymers, concretes, ductile metals, fiber-reinforced polymeric composites, etc), such a treatment is appropriate [23, 28, 65, 69, 70].

If the element is cut by a single crack, there are two basic crack configurations: 1) two quadrilateral subdomains as shown in Figure 3(b), and 2) one triangular subdomain and one pentagonal subdomain as shown in Figure (3c). For each crack, a local coordinate system is defined by the directions along (**s**) and perpendicular to (**n**) the crack path, from which the normal (δ_n) and shear (δ_s) crack displacements can be defined as shown in Figure 3(b). These local crack displacements are related to the global crack displacements, Δu and Δv, by $\{\delta_s,\delta_n\}^{\mathbf{T}}=[\mathbf{R}_1]\{\Delta u,\Delta v\}^{\mathbf{T}}$, where $[\mathbf{R}_1]=\begin{bmatrix}\cos\theta_1 & \sin\theta_1\\ -\sin\theta_1 & \cos\theta_1\end{bmatrix}$ is the rotational matrix between the global and local coordinates and θ_1 is the angle between global **x**-axis and local **s**-axis (Figure 3).

We introduce 4 internal nodes (node 5, 6, 6', and 5' in Figure 3 (b) and (c)) with regular displacement DoFs so that the displacement jumps across the crack are simply the differences in displacements between the respective node-pairs 5-5' and 6-6'.

With the help of these internal nodes, the displacement field in each subdomain, $\mathbf{u}^{\alpha}$ (α = + or −), can be obtained through standard FE shape function interpolation as below,

$$\mathbf{u}^{\alpha} = \mathbf{N}^{\alpha} \cdot \mathbf{d}^{\alpha}; \tag{16}$$

where $\mathbf{d}^{\alpha}$ is the nodal displacement array of the subdomain α (α = + or −). If the element is cut into 2 quadrilateral sub-domains as shown in Figure 3(b), $\mathbf{d}^{+} = \{u_3, v_3, u_4, v_4, | u_{6'}, v_{6'}, u_{5'}, v_{5'}\}^{\mathbf{T}}$ and $\mathbf{d}^{-} = \{u_1, v_1, u_2, v_2, | u_6, v_6, u_5, v_5\}^{\mathbf{T}}$. $\mathbf{N}^{\alpha}$ is the interpolation matrix composed of standard bi-linear isoparametric shape functions. The symbol "|" indicates that the displacements ahead of it are external nodal displacements which are denoted with $\mathbf{d}_{ext}^{+} = \{u_3, v_3, u_4, v_4\}^{\mathbf{T}}$, and those behind it are the internal nodal displacements which are denoted with $\mathbf{d}_{\text{int}}^{+} = \{u_{6'}, v_{6'}, u_{5'}, v_{5'}\}^{\mathbf{T}}$. Similarly, $\mathbf{d}_{ext}^{-} = \{u_1, v_1, u_2, v_2\}^{\mathbf{T}}$ and $\mathbf{d}_{\text{int}}^{-} = \{u_6, v_6, u_5, v_5\}^{\mathbf{T}}$.

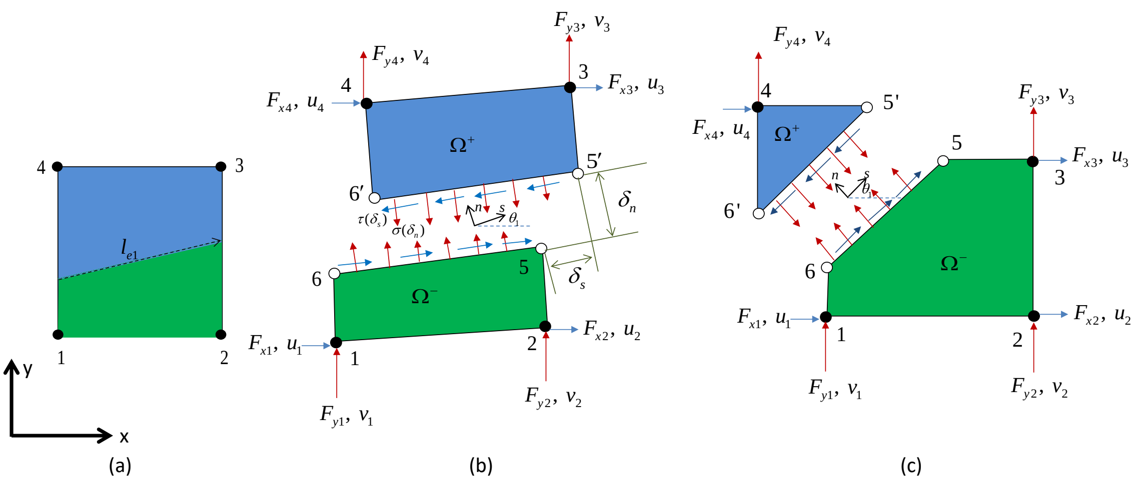

Figure 3 Illustration of the element augmentation from (a) a regular element with possible different material domains, to (b) an A-FE with two quadrilateral sub-domains, or to (c) an A-FE with one triangular sub-domain and one pentagonal sub-domain.

If the element is cut into a triangular and a pentagonal subdomain as in Figure 3(c), then $\mathbf{d}^{+} = \begin{Bmatrix} \mathbf{d}_{ext}^{+} \\ \mathbf{d}_{\text{int}}^{+} \end{Bmatrix} = \{u_4, v_4, | u_{6'}, v_{6'}, u_{5'}, v_{5'}\}^{\mathbf{T}}$ and $\mathbf{d}^{-} = \begin{Bmatrix} \mathbf{d}_{ext}^{-} \\ \mathbf{d}_{\text{int}}^{-} \end{Bmatrix} = \{u_1, v_1, u_2, v_2, u_3, v_3, | u_6, v_6, u_5, v_5\}^{\mathbf{T}}$. The shape functions in the interpolation matrix $\mathbf{N}^{\alpha}$ are from the polygon FEM with optimized quadrature rules recently developed by Sukumar and colleagues [71, 72]. The strain field in each subdomain is:

$$\boldsymbol{\varepsilon}^{\alpha} = (\partial_L{}^{\mathbf{T}} \mathbf{N}^{\alpha}) \cdot \mathbf{d}^{\alpha} = \mathbf{B}^{\alpha} \cdot \mathbf{d}^{\alpha}; \tag{17}$$

where ∂_L is the differentiation operator, i. e., $\partial_L = \begin{bmatrix} \partial/\partial x & 0 & \partial/\partial y \\ 0 & \partial/\partial y & \partial/\partial x \end{bmatrix}$, and $\mathbf{B}^{\alpha}$ is the so-called strain matrix.

Substituting Eqn (16) and (17) into Eqn (5) and using the principle of virtual work, one obtains the weak form of the equilibrium equation for standard elements

$$\begin{cases} \mathbf{L}^{+} \cdot \mathbf{d}^{+} = \mathbf{F}_{ext}^{+} + \mathbf{F}_{\text{int}}^{+} \\ \mathbf{L}^{-} \cdot \mathbf{d}^{-} = \mathbf{F}_{ext}^{-} + \mathbf{F}_{\text{int}}^{-} \end{cases} \tag{18}$$

where

$\mathbf{L}^{\alpha} = \int_{\Omega_e^{\alpha}} (\mathbf{B}^{\alpha})^{\mathbf{T}} \mathbf{D}^{\alpha} \mathbf{B}^{\alpha} \mathrm{d}\Omega$ is the stiffness matrix corresponding to subdomain α;

$\mathbf{F}_{ext}^{\alpha} = \int_{\Gamma_F{}^{\alpha}} (\mathbf{N}^{\alpha})^{\mathbf{T}} \mathbf{f}^{\alpha} \mathrm{d}\Gamma$ is the equivalent external force array on subdomain α;

$\mathbf{F}_{\text{int}}^{\alpha} = \int_{\Gamma_c{}^{\alpha}} (\mathbf{N}_{\text{coh}}{}^{\alpha})^{\mathbf{T}} \mathbf{t}^{a}\ \mathrm{d}\Gamma$ is the equivalent internal force array integrated from the cohesive stresses along the intra-element cohesive crack.

$\mathbf{D}^{\alpha}$ is the material stiffness matrix transformed from the local coordinates into the global coordinates (see, for example [73]).

In the interest of developing an efficient A-FE that can deal with multiple interactive intra-elemental cracks, here we adopt the non-conforming approach, which basically assumes that the inter-element continuity is enforced only through the regular (or external) nodes and their nodal DoFs ($\mathbf{d}_{ext}^{+}$ and $\mathbf{d}_{ext}^{-}$); while the conformity of the internal DoFs associated with the internal nodes ($\mathbf{d}_{\text{int}}^{+}$ and $\mathbf{d}_{\text{int}}^{-}$) are not enforced. This simplification leads to the conclusion that $\mathbf{F}_{ext}^{\alpha}$ is a function of regular nodal DoFs ($\mathbf{d}_{ext}^{+}$ and $\mathbf{d}_{ext}^{-}$) only, and $\mathbf{F}_{\text{int}}^{\alpha}$ is a function of internal DoFs ($\mathbf{d}_{\text{int}}^{+}$ and $\mathbf{d}_{\text{int}}^{-}$) only, which allow us to re-write Eqn (8) as follows,

$$\begin{cases} \begin{bmatrix} \mathbf{L}_{11}^{+} & \mathbf{L}_{12}^{+} \\ \mathbf{L}_{21}^{+} & \mathbf{L}_{22}^{+} \end{bmatrix} \begin{Bmatrix} \mathbf{d}_{ext}^{+} \\ \mathbf{d}_{\text{int}}^{+} \end{Bmatrix} = \begin{Bmatrix} \mathbf{F}_{ext}^{+} \\ \mathbf{F}_{\text{int}}^{+} \end{Bmatrix} \\ \begin{bmatrix} \mathbf{L}_{11}^{-} & \mathbf{L}_{12}^{-} \\ \mathbf{L}_{21}^{-} & \mathbf{L}_{22}^{-} \end{bmatrix} \begin{Bmatrix} \mathbf{d}_{ext}^{-} \\ \mathbf{d}_{\text{int}}^{-} \end{Bmatrix} = \begin{Bmatrix} \mathbf{F}_{ext}^{-} \\ \mathbf{F}_{\text{int}}^{-} \end{Bmatrix} \end{cases} \tag{19}$$

Where $\mathbf{L}_{ij}^{\alpha}$ (i, j = 1, 2; α = +, -) are the sub-matrices of $\mathbf{L}^{\alpha}$, i.e., $\mathbf{L}^{\alpha} = \begin{bmatrix} \mathbf{L}_{11}^{\alpha} & \mathbf{L}_{12}^{\alpha} \\ \mathbf{L}_{21}^{\alpha} & \mathbf{L}_{22}^{\alpha} \end{bmatrix}$. We note that $\mathbf{L}_{22}^{\alpha}$ is the sub-stiffness matrix related to the two internal nodes of the subdomain α.

Next we derive the condensed elemental equilibrium equation for both of the configurations in Fig 3(b) and Fig 3(c) in a unified formulation. It is noted that for both configurations, the internal DoF and equivalent force arrays are the same, i. e.,

$$\mathbf{d}_{\text{int}}^{+} = \mathbf{d}_{6'5'} = \{u_{6'}, v_{6'}, u_{5'}, v_{5'}\}^{\mathbf{T}}; \qquad \mathbf{F}_{\text{int}}^{+} = \mathbf{F}_{6'5'} = \{F_{x6'}, F_{y6'}, F_{x5'}, F_{y5'}\}^{\mathbf{T}}$$
$$\mathbf{d}_{\text{int}}^{-} = \mathbf{d}_{65} = \{u_{6}, v_{6}, u_{5}, v_{5}\}^{\mathbf{T}}; \qquad \mathbf{F}_{\text{int}}^{-} = \mathbf{F}_{65} = \{F_{x6}, F_{y6}, F_{x5}, F_{y5}\}^{\mathbf{T}} \tag{20a}$$

The external DoF and force arrays are specific to a particular crack configuration. For the two quadrilateral subdomain configurations (Fig 3b),

$$\mathbf{d}_{ext}^{+} = \mathbf{d}_{34} = \{u_{3}, v_{3}, u_{4}, v_{4}\}^{\mathbf{T}}; \qquad \mathbf{F}_{ext}^{+} = \mathbf{F}_{34} = \{F_{x3}, F_{y3}, F_{x4}, F_{y4}\}^{\mathbf{T}}$$
$$\mathbf{d}_{ext}^{-} = \mathbf{d}_{12} = \{u_{1}, v_{1}, u_{2}, v_{2}\}^{\mathbf{T}}; \qquad \mathbf{F}_{ext}^{-} = \mathbf{F}_{12} = \{F_{x1}, F_{y1}, F_{x2}, F_{y2}\}^{\mathbf{T}}, \tag{20b}$$

For the triangular-pentagonal subdomain configuration of Fig 3(c),

$$\mathbf{d}_{ext}^{+} = \mathbf{d}_{4} = \{u_{4}, v_{4}\}^{\mathbf{T}}; \qquad \mathbf{F}_{ext}^{+} = \mathbf{F}_{4} = \{F_{x4}, F_{y4}\}^{\mathbf{T}}$$
$$\mathbf{d}_{ext}^{-} = \mathbf{d}_{123} = \{u_{1}, v_{1}, u_{2}, v_{2}, u_{3}, v_{3}\}^{\mathbf{T}}; \qquad \mathbf{F}_{ext}^{-} = \mathbf{F}_{123} = \{F_{x1}, F_{y1}, F_{x2}, F_{y2}, F_{x3}, F_{y3}\}^{\mathbf{T}} \tag{20c}$$

However, for both configurations, the equilibrium can be written as

$$\begin{bmatrix} \mathbf{L}_{11}^{+} & \mathbf{L}_{12}^{+} \\ \mathbf{L}_{21}^{+} & \mathbf{L}_{22}^{+} \end{bmatrix} \begin{Bmatrix} \mathbf{d}_{ext}^{+} \\ \mathbf{d}_{6'5'} \end{Bmatrix} = \begin{Bmatrix} \mathbf{F}_{ext}^{+} \\ \mathbf{F}_{6'5'} \end{Bmatrix} \quad \begin{matrix} \text{(a)} \\ \text{(b)} \end{matrix} \qquad (\text{for } \Omega^{+})$$
$$\begin{bmatrix} \mathbf{L}_{11}^{-}] & \mathbf{L}_{12}^{-} \\ \mathbf{L}_{21}^{-}] & \mathbf{L}_{22}^{-} \end{bmatrix} \begin{Bmatrix} \mathbf{d}_{ext}^{-} \\ \mathbf{d}_{65} \end{Bmatrix} = \begin{Bmatrix} \mathbf{F}_{ext}^{-} \\ \mathbf{F}_{65} \end{Bmatrix} \quad \begin{matrix} \text{(c)} \\ \text{(d)} \end{matrix} \qquad (\text{for } \Omega^{-}) \tag{21}$$

Also, due to stress continuity across the cohesive crack, $\mathbf{F}_{65} = -\mathbf{F}_{6'5'} = \int_{\Gamma_c^{\alpha}} \mathbf{N}_{\text{coh}}{}^{\mathbf{T}} \mathbf{t} \, d\Gamma$. Eqn (21) is valid for both weak and strong discontinuous problems.

<u>Weak Discontinuity:</u> For weak discontinuity problems, $\mathbf{d}_{6'5'} = \mathbf{d}_{65}$. Together with the condition of $\mathbf{F}_{65} = -\mathbf{F}_{6'5'}$, Eqn (21) further simplifies to

$$\begin{Bmatrix} \mathbf{F}_{ext}^{-} \\ \mathbf{F}_{ext}^{+} \end{Bmatrix} = \begin{bmatrix} \mathbf{L}_{11}^{-} - \mathbf{L}_{12}^{-}\boldsymbol{\Lambda}^{-1}\mathbf{L}_{21}^{-} & -\mathbf{L}_{12}^{-}\boldsymbol{\Lambda}^{-1}\mathbf{L}_{21}^{+} \\ -\mathbf{L}_{12}^{+}\boldsymbol{\Lambda}^{-1}\mathbf{L}_{21}^{-} & \mathbf{L}_{11}^{+} - \mathbf{L}_{12}^{+}\boldsymbol{\Lambda}^{-1}\mathbf{L}_{21}^{+} \end{bmatrix} \begin{Bmatrix} \mathbf{d}_{ext}^{-} \\ \mathbf{d}_{ext}^{+} \end{Bmatrix}, \tag{22}$$

where $\boldsymbol{\Lambda} = \mathbf{L}_{22}^{-} + \mathbf{L}_{22}^{+}$. Furthermore, the internal forces are determined as:

$$\mathbf{F}_{65} = \left\{ \left(\mathbf{I} - \mathbf{L}_{22}^{-}\boldsymbol{\Lambda}^{-1} \right) \mathbf{L}_{21}^{-}, \quad -\mathbf{L}_{22}^{-}\boldsymbol{\Lambda}^{-1}\mathbf{L}_{21}^{+} \right\} \begin{Bmatrix} \mathbf{d}_{ext}^{-} \\ \mathbf{d}_{ext}^{+} \end{Bmatrix} \tag{23}$$

Thus, for an element containing two material domains with a perfectly bonded interface, once the external nodal displacements are given (which is the case for displacement-based FEs), the resultant forces acting along the interface are immediately known. This solution is mathematically rigorous in the FEM sense.

With $\mathbf{F}_{65}$ known, the current tractions acting on the interface are known. For example, the normal and shear stresses averaged along the interface, in local coordinates, are $\begin{Bmatrix} \bar{\tau}_{\text{int}} \\ \bar{\sigma}_{\text{int}} \end{Bmatrix} = [\mathbf{R}_1]^{\mathbf{T}} \begin{Bmatrix} (F_{x5}+F_{x6})/l_{e1} \\ (F_{y5}+F_{y6})/l_{e1} \end{Bmatrix}$, where l_{e1} is the interface length (Fig 3a). These stresses can then be used to determine the initiation of interface debonding, which is the turning point from a weak discontinuity to a strong one. A common initiation criterion used in this paper, is

$$\left(< \bar{\sigma}_{\text{int}} > / \hat{\sigma}_1\right)^2 + \left(\bar{\tau}_{\text{int}} / \hat{\tau}_1\right)^2 = 1 \tag{24}$$

where the MacAuley bracket $< \bullet >$, defined as $< \bullet > = (\bullet + |\bullet|)/2$, is used to reflect the physical observation that compressive normal stresses do not contribute to crack initiation.

If this criterion of Eqn (24) is met, the discontinuity becomes a strong one, i.e., $\mathbf{d}_{6'5'} \neq \mathbf{d}_{65}$, which is addressed next.

Strong Discontinuity: For strong discontinuities, we shall consider cohesive cracks with mixed-mode piece-wise linear traction-separation laws as detailed in Figure 2, where the linear segments of each traction-separation laws are properly indexed. The indexing scheme is closely related to the new condensation solver that will be described shortly.

Following the notation established in section 2.2, the cohesive stresses between the two pairs of internal nodes 5-5' and 6-6' can be expressed in its local coordinates as

$$\left\{\tau_{6'6}{}^{(i)}, \sigma_{6'6}{}^{(j)}, \tau_{5'5}{}^{(k)}, \sigma_{5'5}{}^{(l)}\right\}^{\mathbf{T}} = \boldsymbol{\sigma}_{\mathbf{0}} + \boldsymbol{\alpha}_0 \left\{\delta_{s6'6}, \delta_{n6'6}, \delta_{s5'5}, \delta_{n5'5}\right\}^{\mathbf{T}} \quad (i, j, k, l = 1, 2, \cdots 4) \tag{25a}$$

where

$$\boldsymbol{\sigma}_{\mathbf{0}} = \left\{\hat{\tau}^{(i-1)} - \alpha_s{}^{(i)}\delta_s{}^{(i-1)}, \hat{\sigma}^{(j-1)} - \alpha_n{}^{(j)}\delta_n{}^{(j-1)}, \hat{\tau}^{(k-1)} - \alpha_s{}^{(k)}\delta_s{}^{(k-1)}, \hat{\sigma}^{(l-1)} - \alpha_n{}^{(l)}\delta_n{}^{(l-1)}\right\}^{\mathbf{T}} \tag{25b}$$

is the characteristic stress matrix. The critical stresses, $\hat{\tau}^{(i)}$ and $\hat{\sigma}^{(j)}$ $(i, j = 1,..,4)$ have been defined in section 2.2 (Eqn 10, Eng 11 and Figure 2).

$$\boldsymbol{\alpha}_0 = \text{Diag}[\alpha_s{}^{(i)}; \alpha_n{}^{(j)}; \alpha_s{}^{(k)}; \alpha_n{}^{(l)}] \tag{25c}$$

is the cohesive stiffness matrix. Here $\text{Diag}[a;\ b;\ c;\ d]$ means a diagonal matrix with non-zero arguments *a*, *b*, *c*, and *d* at the corresponding diagonal places. This notation will be used in the rest of this paper. $\left\{\delta_{s6'6}, \delta_{n6'6}, \delta_{s5'5}, \delta_{n5'5}\right\}^{\mathbf{T}}$ is the crack displacement array at internal node-pairs 6'-6 and 5'-5 measured in local coordinate system.

Each of the free indices (*i*, *j*, *k*, *l*) can range from 1 to the maximum cohesive segment number, indicating in which segments of the cohesive laws the current cohesive stresses are located

(Section 2.2). Note that the characteristic stress ($\boldsymbol{\sigma_0}$) and stiffness matrices ($\boldsymbol{\alpha_0}$) are determined if any particular combination of (*i*, *j*, *k*, *l*) is chosen.

$\mathbf{F}_{65}$ and $\mathbf{F}_{6'5'}$ are obtained by integrating the cohesive stresses in Eqn (25a) over the crack plane and then converted into global coordinates using the rotation matrix $\mathbf{R_1}$, which gives:

$$\mathbf{F}_{65} = -\mathbf{F}_{6'5'} = l_{e1}\left(\mathbf{S_0} + \boldsymbol{\alpha}\cdot\Delta\mathbf{d}_{\text{int}}\right) \tag{26a}$$

where $\Delta\mathbf{d}_{\text{int}} = \mathbf{d}_{6'5'} - \mathbf{d}_{65} = \left\{(\mathbf{d}_{6'} - \mathbf{d}_6),\ (\mathbf{d}_{5'} - \mathbf{d}_5)\right\}^T$ are the crack displacements at node pairs 6'-6 and 5'-5 in global coordinates, i. e.,

$$\Delta\mathbf{d}_{\text{int}} = \mathbf{d}_{6'5'} - \mathbf{d}_{65} = \text{Diag}[\mathbf{R}_1;\mathbf{R}_1]\left\{\delta_{s66'},\delta_{n66'},\delta_{s55'},\delta_{n55'}\right\}^{\mathbf{T}} \tag{26b}$$

$\{\mathbf{S_0}\}$ and $[\boldsymbol{\alpha}]$ are related to the characteristic cohesive stress and stiffness matrices in Eqn (25):

$$\begin{aligned}\mathbf{S}_0 &= \text{Diag}[\mathbf{R}_1^{\mathbf{T}};\ \mathbf{R}_1^{\mathbf{T}}]\ (\mathbf{T}_{\text{coh}})^{\mathbf{T}}\ \boldsymbol{\sigma_0}\\ \boldsymbol{\alpha} &= \text{Diag}[\mathbf{R}_1^{\mathbf{T}};\ \mathbf{R}_1^{\mathbf{T}}]\ (\mathbf{T}_{\text{coh}})^{\mathbf{T}}\ \boldsymbol{\alpha}_0\ \mathbf{N}_{\text{coh}}\ \text{Diag}[\mathbf{R}_1;\ \mathbf{R}_1]\end{aligned} \tag{26c}$$

Here $\mathbf{T}_{\text{coh}}$ and $\mathbf{N}_{\text{coh}}$ are the integration and interpolation matrices associated with the cohesive stress integration and the displacement interpolation along the crack plane, respectively. For the single crack case, we used the standard Gaussian interpolation and integration scheme with 2 integration points, i.e.,

$$\mathbf{N}_{\text{coh}} = \begin{bmatrix}\text{Diag}[\xi_{\text{B}};\xi_{\text{B}}] & \text{Diag}[\xi_{\text{A}};\xi_{\text{A}}]\\ \text{Diag}[\xi_{\text{A}};\xi_{\text{A}}] & \text{Diag}[\xi_{\text{B}};\xi_{\text{B}}]\end{bmatrix};\ \mathbf{T}_{\text{coh}} = \frac{l_{e1}}{2}\begin{bmatrix}\text{Diag}[\xi_{\text{B}};\xi_{\text{B}}] & \text{Diag}[\xi_{\text{A}};\xi_{\text{A}}]\\ \text{Diag}[\xi_{\text{A}};\xi_{\text{A}}] & \text{Diag}[\xi_{\text{B}};\xi_{\text{B}}]\end{bmatrix} = \frac{l_{e1}}{2}(\mathbf{N}_{\text{coh}})^{\mathbf{T}},$$

where $\xi_A = \left(1 - 1/\sqrt{3}\right)/2$ and $\xi_B = \left(1 + 1/\sqrt{3}\right)/2$. (The matrices for several other popular interpolation and integration schemes have been summarized and evaluated in [57, 74]).

Substituting Eqn (26) into expressions (b) and (d) in Eqn (21), the following equation is derived:

$$\begin{cases}(\mathbf{L}_{22}^{+} + l_{e1}\boldsymbol{\alpha})\mathbf{d}_{6'5'} - (l_{e1}\boldsymbol{\alpha})\mathbf{d}_{65} = -l_{e1}\mathbf{S_0} - \mathbf{L}_{21}^{+}\mathbf{d}_{ext}^{+}\\ -(l_{e1}\boldsymbol{\alpha})\mathbf{d}_{6'5'} + (\mathbf{L}_{22}^{-} + l_{e1}\boldsymbol{\alpha})\mathbf{d}_{65} = l_{e1}\mathbf{S_0} - \mathbf{L}_{21}^{-}\mathbf{d}_{ext}^{-}\end{cases} \tag{27}$$

For a given cohesive segment combination ((*i*, *j*, *k*, *l*) this is a linear equation, from which the crack displacements at the internal node pairs, $\Delta\mathbf{d}_{\text{int}} = \mathbf{d}_{6'5'} - \mathbf{d}_{65}$, is solved explicitly:

$$\begin{aligned}\Delta\mathbf{d}_{\text{int}} = &-l_{e1}\left(\mathbf{A}^{-1} + \mathbf{B}^{-1} - l_{e1}\mathbf{A}^{-1}\boldsymbol{\alpha}(\boldsymbol{\Psi}_{22}^{-})^{-1} + l_{e1}\mathbf{B}^{-1}\boldsymbol{\alpha}(\boldsymbol{\Psi}_{22}^{+})^{-1}\right)\mathbf{S}_0\\ &+\left(\mathbf{B}^{-1} - l_{e1}\mathbf{A}^{-1}\boldsymbol{\alpha}(\boldsymbol{\Psi}_{22}^{-})^{-1}\right)\mathbf{L}_{21}^{-}\mathbf{d}_{ext}^{-} + \left(l_{e1}\mathbf{B}^{-1}\boldsymbol{\alpha}(\boldsymbol{\Psi}_{22}^{+})^{-1} - \mathbf{A}^{-1}\right)\mathbf{L}_{21}^{+}\mathbf{d}_{ext}^{+}\end{aligned} \tag{28a}$$

where,

$$\boldsymbol{\Psi}_{22}^{+}=\mathbf{L}_{22}^{+}+l_{e1}\boldsymbol{\alpha};\boldsymbol{\Psi}_{22}^{-}=\mathbf{L}_{22}^{-}+l_{e1}\boldsymbol{\alpha};\mathbf{A}=\boldsymbol{\Psi}_{22}^{+}-l_{e1}{}^{2}\boldsymbol{\alpha}(\boldsymbol{\Psi}_{22}^{-})^{-1}\boldsymbol{\alpha};\ \mathbf{B}=\boldsymbol{\Psi}_{22}^{-}-l_{e1}{}^{2}\boldsymbol{\alpha}(\boldsymbol{\Psi}_{22}^{+})^{-1}\boldsymbol{\alpha} \quad \text{(28b)}$$

The explicit solution to the crack displacements can also be solved as:

$$\begin{aligned}\begin{Bmatrix}\mathbf{d}_{6'5'}\\ \mathbf{d}_{65}\end{Bmatrix}=&\begin{bmatrix}-l_{e1}\mathbf{A}^{-1}\left(\mathbf{I}-l_{e1}\boldsymbol{\alpha}(\boldsymbol{\Psi}_{22}^{-})^{-1}\right) & \mathbf{0}\\ \mathbf{0} & l_{e1}\mathbf{B}^{-1}\left(\mathbf{I}-l_{e1}\boldsymbol{\alpha}(\boldsymbol{\Psi}_{22}^{+})^{-1}\right)\end{bmatrix}\begin{Bmatrix}\mathbf{S}_0\\ \mathbf{S}_0\end{Bmatrix}\\ &+\begin{bmatrix}-l_{e1}\mathbf{A}^{-1}\boldsymbol{\alpha}(\boldsymbol{\Psi}_{22}^{-})^{-1}\mathbf{L}_{21}^{-} & -\mathbf{A}^{-1}\mathbf{L}_{21}^{+}\\ -\mathbf{B}^{-1}\mathbf{L}_{21}^{-} & -l_{e1}\mathbf{B}^{-1}\boldsymbol{\alpha}(\boldsymbol{\Psi}_{22}^{+})^{-1}\mathbf{L}_{21}^{+}\end{bmatrix}\begin{Bmatrix}\mathbf{d}_{ext}^{-}\\ \mathbf{d}_{ext}^{+}\end{Bmatrix}\end{aligned} \quad \text{(28c)}$$

The fully condensed equilibrium equation without any internal forces and displacements can be obtained by substituting Eqn (28) into expressions (a) and (c) in Eqn (21) and eliminating $\mathbf{F}_{65}$ and $\mathbf{F}_{6'5'}$, i. e.,

$$\begin{aligned}&\begin{bmatrix}\mathbf{L}_{11}^{-}-\mathbf{L}_{12}^{-}\mathbf{B}^{-1}\mathbf{L}_{21}^{-} & -l_{e1}\mathbf{L}_{12}^{-}\mathbf{B}^{-1}\boldsymbol{\alpha}(\boldsymbol{\Psi}_{22}^{+})^{-1}\mathbf{L}_{21}^{+}\\ -l_{e1}\mathbf{L}_{12}^{+}\mathbf{A}^{-1}\boldsymbol{\alpha}(\boldsymbol{\Psi}_{22}^{-})^{-1}\mathbf{L}_{21}^{-} & \mathbf{L}_{11}^{+}-\mathbf{L}_{12}^{+}\mathbf{A}^{-1}\mathbf{L}_{21}^{+}\end{bmatrix}\begin{Bmatrix}\mathbf{d}_{ext}^{-}\\ \mathbf{d}_{ext}^{+}\end{Bmatrix}\\ &=\begin{Bmatrix}\mathbf{F}_{ext}^{-}\\ \mathbf{F}_{ext}^{+}\end{Bmatrix}-\begin{bmatrix}l_{e1}\mathbf{L}_{12}^{-}\mathbf{B}^{-1}\left(\mathbf{I}-l_{e1}\boldsymbol{\alpha}(\boldsymbol{\Psi}_{22}^{+})^{-1}\right) & 0\\ 0 & -l_{e1}\mathbf{L}_{12}^{+}\mathbf{A}^{-1}\left(\mathbf{I}-l_{e1}\boldsymbol{\alpha}(\boldsymbol{\Psi}_{22}^{-})^{-1}\right)\end{bmatrix}\begin{Bmatrix}\mathbf{S}_0\\ \mathbf{S}_0\end{Bmatrix}\end{aligned} \quad \text{(29)}$$

Eqn (29) is highly nonlinear because the matrices $\mathbf{S}_0, \mathbf{A},\ \mathbf{B},\ \boldsymbol{\Psi}_{22}^{+},$ and $\boldsymbol{\Psi}_{22}^{-}$, are all nonlinear functions of the crack displacements $\Delta\mathbf{d}_{\text{int}}$ (through $\boldsymbol{\alpha}_0$ and $\boldsymbol{\sigma}_0$ – see Eqn 26c and Eqn 28b), which are not known because at this point the only information is the external displacements $\mathbf{d}_{ext}^{-}$ and $\mathbf{d}_{ext}^{+}$. We shall defer the discussion of solution procedure until section 3.3.

3.2 A-FE Formulation with Two Interactive Cracks

The internal DoFs associated with the four internal nodes, together with the regular nodal DoFs, allows for stress evaluations at each subdomain, making it possible for further augmentation of the element for hosting more than one cohesive crack. A secondary crack can be introduced to a subdomain as long as it has more than one regular (external) node. In such a case, there are altogether three basic cracking configurations as shown in Fig 4a(1), Fig 4a(2) and Fig4a(3), where l_{e1} is the first crack length and l_{e2} is the second crack length. The second crack intersects and cuts the first crack into two segments with length γl_{e1} (left) and $(1-\gamma)l_{e1}$ (right). The three subdomains are noted with Ω^{+}, $\Omega^{l-}$and Ω^{r-} as shown in Figure 4b.

The deformed configurations corresponding to the three cases in Figure 4(a1-a3) are shown in Figure 4(b1-b3). To describe the discontinuity induced by the second crack, four more internal nodes, 7, 8, 7', and 8' are introduced and a local coordinate system is defined by the angle between its tangential direction ($\mathbf{s}_2$) and global x-direction, θ_2. The rotation matrix associated with this crack

is $\left[\mathbf{R}_2\right]=\begin{bmatrix}\cos\theta_2 & \sin\theta_2\\ -\sin\theta_2 & \cos\theta_2\end{bmatrix}$. With the 8 internal nodes, it is possible to integrate the subdomain stiffness matrix for each subdomain. In the following, we show that a unified elemental equilibrium equation can be derived for all the three configurations.

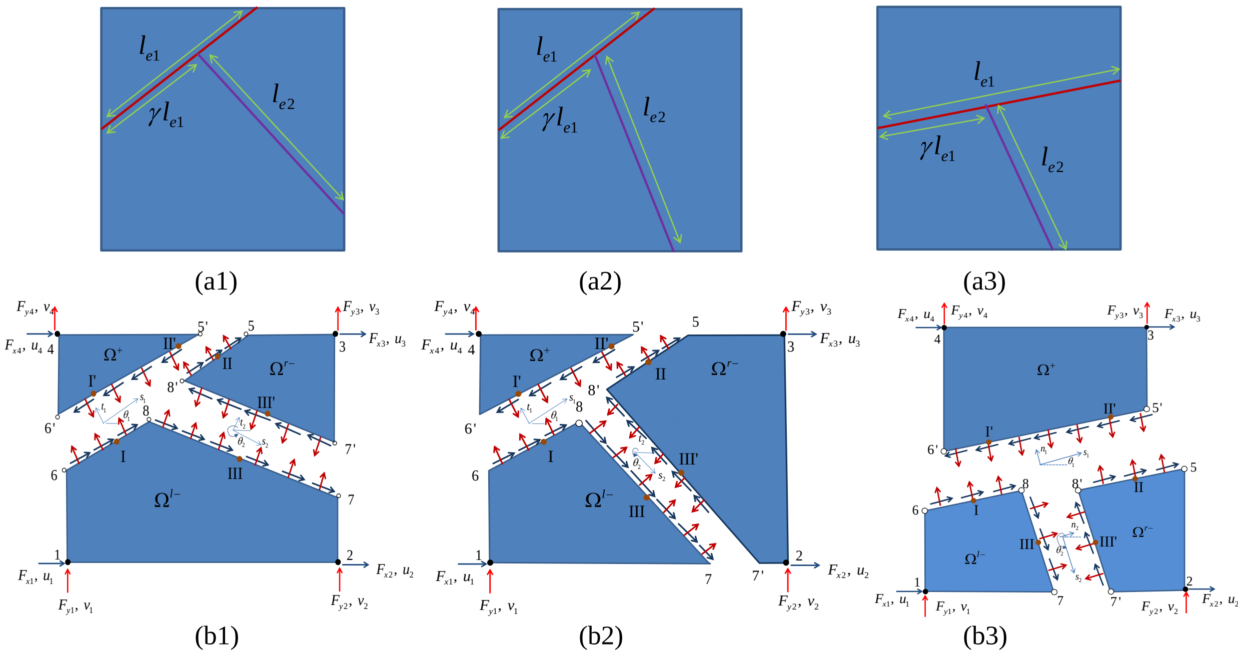

Figure 4 Illustration of a 2D A-FE with two intra-elemental cracks (3 subdomains)

Despite the different crack configurations in Figure 4, the internal DoF and force arrays can be arranged in a unified way as below.

$$\begin{aligned}&\mathbf{d}_{\text{int}}^{+}=\mathbf{d}_{6'5'};\ \mathbf{d}_{\text{int}}^{r-}=\mathbf{d}_{58'7'};\ \mathbf{d}_{\text{int}}^{l-}=\mathbf{d}_{786}\\ &\mathbf{F}_{\text{int}}^{+}=\mathbf{F}_{6'5'};\ \mathbf{F}_{\text{int}}^{r-}=\mathbf{F}_{58'7'};\ \mathbf{F}_{\text{int}}^{l-}=\mathbf{F}_{786}\end{aligned} \tag{30}$$

This enables a unified expression for the equilibrium of all three subdomains as follows

$$\begin{cases}\begin{bmatrix}\mathbf{L}_{11}^{+} & \mathbf{L}_{12}^{+}\\ \mathbf{L}_{21}^{+} & \mathbf{L}_{22}^{+}\end{bmatrix}\begin{Bmatrix}\mathbf{d}_{ext}^{+}\\ \mathbf{d}_{6'5'}\end{Bmatrix}=\begin{Bmatrix}\mathbf{F}_{ext}^{+}\\ \mathbf{F}_{6'5'}\end{Bmatrix} & \begin{matrix}\text{(a)}\\ \text{(b)}\end{matrix} \quad (\text{for } \Omega^{+})\\ \begin{bmatrix}\mathbf{L}_{11}^{r-} & \mathbf{L}_{12}^{r-}\\ \mathbf{L}_{21}^{r-} & \mathbf{L}_{22}^{r-}\end{bmatrix}\begin{Bmatrix}\mathbf{d}_{ext}^{r-}\\ \mathbf{d}_{58'7'}\end{Bmatrix}=\begin{Bmatrix}\mathbf{F}_{ext}^{r-}\\ \mathbf{F}_{58'7'}\end{Bmatrix} & \begin{matrix}\text{(c)}\\ \text{(d)}\end{matrix} \quad (\text{for } \Omega^{r-})\\ \begin{bmatrix}\mathbf{L}_{11}^{l-} & \mathbf{L}_{12}^{l-}\\ \mathbf{L}_{21}^{l-} & \mathbf{L}_{22}^{l-}\end{bmatrix}\begin{Bmatrix}\mathbf{d}_{ext}^{l-}\\ \mathbf{d}_{786}\end{Bmatrix}=\begin{Bmatrix}\mathbf{F}_{ext}^{l-}\\ \mathbf{F}_{786}\end{Bmatrix} & \begin{matrix}\text{(e)}\\ \text{(f)}\end{matrix} \quad (\text{for } \Omega^{l-})\end{cases} \tag{31}$$

Here, the sub-matrices ($\mathbf{L}_{ij}^{l-},\mathbf{L}_{ij}^{r-}$, and $\mathbf{L}_{ij}^{+}$ $(i,\, j=1,2)$) are the stiffness matrices of the subdomains Ω^{+}, $\Omega^{r-}$and Ω^{l-} , respectively. They were computed, according to the respective

crack configurations in Fig 4(b1-b3), with the sub-domain integration scheme discussed in section 3.1.

To integrate the cohesive stress along the three cohesive crack segments into respective internal nodal forces, the first order Gaussian Integration scheme with one integration points was used on each of the three cracked segments (i.e., assuming uniform cohesive stresses along each crack segment). The integration points are at the center of each crack segment as indicated in Figure 4(b) by the solid dots labeled by I, II, and III.

Denote the cohesive stresses at these points as ($\sigma_{\mathrm{I}}{}^{(i)}, \tau_{\mathrm{I}}{}^{(j)}$), ($\sigma_{\mathrm{II}}{}^{(k)}, \tau_{\mathrm{II}}{}^{(l)}$), and ($\sigma_{\mathrm{III}}{}^{(m)}, \tau_{\mathrm{III}}{}^{(n)}$). The superscript (*i, j, k, l, m, n*) are the free indices of the assumed cohesive segment numbers. The relation between these cohesive stresses and the internal nodal displacements is

$$\begin{cases} \left\{\tau_{\mathrm{I}}{}^{(i)}, \sigma_{\mathrm{I}}{}^{(j)}\right\}^{\mathbf{T}} = \boldsymbol{\sigma}_{0\mathrm{I}} + \boldsymbol{\alpha}_{0\mathrm{I}}\mathbf{R}_1\left((1-\gamma/2)\mathbf{d}_{6'} + (\gamma/2)\mathbf{d}_{5'}\right) - \boldsymbol{\alpha}_{0\mathrm{I}}\mathbf{R}_1\left(\mathbf{d}_6 + \mathbf{d}_8\right)/2 \\ \left\{\tau_{\mathrm{II}}{}^{(k)}, \sigma_{\mathrm{II}}{}^{(l)}\right\}^{\mathbf{T}} = \boldsymbol{\sigma}_{0\mathrm{II}} + \boldsymbol{\alpha}_{0\mathrm{II}}\mathbf{R}_1\left((1-\gamma/2)\mathbf{d}_{6'} + (1+\gamma/2)\mathbf{d}_{5'}\right) - \boldsymbol{\alpha}_{0\mathrm{II}}\mathbf{R}_1\left(\mathbf{d}_5 + \mathbf{d}_{8'}\right)/2 \\ \left\{\tau_{\mathrm{III}}{}^{(m)}, \sigma_{\mathrm{III}}{}^{(n)}\right\}^{\mathbf{T}} = \boldsymbol{\sigma}_{0\mathrm{III}} + \boldsymbol{\alpha}_{0\mathrm{III}}\mathbf{R}_2\left(\mathbf{d}_{7'} + \mathbf{d}_{8'}\right)/2 - \boldsymbol{\alpha}_{0\mathrm{III}}\mathbf{R}_2\left(\mathbf{d}_7 + \mathbf{d}_8\right)/2 \end{cases} \tag{32a}$$

where

$$\boldsymbol{\sigma}_{0\mathrm{I}} = \begin{Bmatrix} \hat{\tau}^{(i)} - \alpha_s{}^{(i)}\delta_s{}^{(i)} \\ \hat{\sigma}^{(j)} - \alpha_n{}^{(j)}\delta_n{}^{(j)} \end{Bmatrix}; \quad \boldsymbol{\sigma}_{0\mathrm{II}} = \begin{Bmatrix} \hat{\tau}^{(k)} - \alpha_s{}^{(k)}\delta_s{}^{(k)} \\ \hat{\sigma}^{(l)} - \alpha_n{}^{(l)}\delta_n{}^{(l)} \end{Bmatrix}; \quad \boldsymbol{\sigma}_{0\mathrm{III}} = \begin{Bmatrix} \hat{\tau}^{(m)} - \alpha_s{}^{(m)}\delta_s{}^{(m)} \\ \hat{\sigma}^{(n)} - \alpha_n{}^{(n)}\delta_n{}^{(n)} \end{Bmatrix} \tag{32b}$$

$$\boldsymbol{\alpha}_{0\mathrm{I}} = \mathrm{Diag}[\alpha_s{}^{(i)};\alpha_n{}^{(j)}]; \quad \boldsymbol{\alpha}_{0\mathrm{II}} = \mathrm{Diag}[\alpha_s{}^{(k)};\alpha_n{}^{(l)}]; \quad \boldsymbol{\alpha}_{0\mathrm{III}} = \mathrm{Diag}[\alpha_s{}^{(m)};\alpha_n{}^{(n)}]; \tag{32c}$$

The internal forces, $\{\mathbf{F}_{6'5'}\}$, $\{\mathbf{F}_{58'7'}\}$, and $\{\mathbf{F}_{786}\}$, integrated from the cohesive stresses along the respective crack lengths are

$$\begin{cases} \mathbf{F}_{6'5'} = \mathbf{T}_{\mathbf{R}}^{+}\left\{\tau_{\mathrm{I}}{}^{(i)}, \quad \sigma_{\mathrm{I}}{}^{(j)}, \quad \tau_{\mathrm{II}}{}^{(k)}, \quad \sigma_{\mathrm{II}}{}^{(l)}\right\}^{\mathbf{T}} \\ \mathbf{F}_{786} = \mathbf{T}_{\mathbf{R}}^{l-}\left\{\tau_{\mathrm{I}}{}^{(i)}, \quad \sigma_{\mathrm{I}}{}^{(j)}, \quad \tau_{\mathrm{III}}{}^{(m)}, \quad \sigma_{\mathrm{III}}{}^{(n)}\right\}^{\mathbf{T}} \\ \mathbf{F}_{58'7'} = \mathbf{T}_{\mathbf{R}}^{r-}\left\{\tau_{\mathrm{I}}{}^{(k)}, \quad \sigma_{\mathrm{I}}{}^{(l)}, \quad \tau_{\mathrm{III}}{}^{(m)}, \quad \sigma_{\mathrm{III}}{}^{(n)}\right\}^{\mathbf{T}} \end{cases} \tag{33a}$$

where $\mathbf{T}_{\mathbf{R}}^{+}$, $\mathbf{T}_{\mathbf{R}}^{l-}$, and $\mathbf{T}_{\mathbf{R}}^{r-}$ are the respective integration matrices as below:

$$\mathbf{T}_{\mathbf{R}}^{+}=-\frac{1}{2}\begin{bmatrix}\gamma\left(2-\gamma\right)l_{e1}\mathbf{R}_1{}^{\mathbf{T}} & \left(1-\gamma\right)^2 l_{e1}\mathbf{R}_1{}^{\mathbf{T}}\\ \gamma^2 l_{e1}\mathbf{R}_1{}^{\mathbf{T}} & (1-\gamma^2)l_{e1}\mathbf{R}_1{}^{\mathbf{T}}\end{bmatrix};$$

$$\mathbf{T}_{\mathbf{R}}^{l-}=\frac{1}{2}\begin{bmatrix}\mathbf{0} & l_{e2}\mathbf{R}_2{}^{\mathbf{T}}\\ \gamma l_{e1}\mathbf{R}_1{}^{\mathbf{T}} & l_{e2}\mathbf{R}_2{}^{\mathbf{T}}\\ \gamma l_{e1}\mathbf{R}_1{}^{\mathbf{T}} & \mathbf{0}\end{bmatrix};\quad \mathbf{T}_{\mathbf{R}}^{r-}=\frac{1}{2}\begin{bmatrix}(1-\gamma)l_{e1}\mathbf{R}_1{}^{\mathbf{T}} & \mathbf{0}\\ (1-\gamma)l_{e1}\mathbf{R}_1{}^{\mathbf{T}} & -l_{e2}\mathbf{R}_2{}^{\mathbf{T}}\\ \mathbf{0} & -l_{e2}\mathbf{R}_2{}^{\mathbf{T}}\end{bmatrix} \tag{33b}$$

Substituting Eqn (32) into (33) and re-organizing terms, the internal forces become:

$$\begin{Bmatrix}\mathbf{F}_{6'5'}\\ \mathbf{F}_{786}\\ \mathbf{F}_{58'7'}\end{Bmatrix}=\begin{Bmatrix}\mathbf{S}_1\\ \mathbf{S}_2\\ \mathbf{S}_3\end{Bmatrix}+\begin{bmatrix}\boldsymbol{\alpha}_{11} & \boldsymbol{\alpha}_{12} & \boldsymbol{\alpha}_{13}\\ \boldsymbol{\alpha}_{21} & \boldsymbol{\alpha}_{22} & \boldsymbol{\alpha}_{23}\\ \boldsymbol{\alpha}_{31} & \boldsymbol{\alpha}_{32} & \boldsymbol{\alpha}_{33}\end{bmatrix}\begin{Bmatrix}\mathbf{d}_{6'5'}\\ \mathbf{d}_{786}\\ \mathbf{d}_{58'7'}\end{Bmatrix} \tag{34a}$$

where

$$\mathbf{S}_1=\mathbf{T}_{\mathbf{R}}^{+}\begin{Bmatrix}\boldsymbol{\sigma}_{0\mathrm{I}}\\ \boldsymbol{\sigma}_{0\mathrm{II}}\end{Bmatrix},\ \mathbf{S}_2=\mathbf{T}_{\mathbf{R}}^{l-}\begin{Bmatrix}\boldsymbol{\sigma}_{0\mathrm{I}}\\ \boldsymbol{\sigma}_{0\mathrm{III}}\end{Bmatrix},\ \mathbf{S}_3=\mathbf{T}_{\mathbf{R}}^{r-}\begin{Bmatrix}\boldsymbol{\sigma}_{0\mathrm{II}}\\ \boldsymbol{\sigma}_{0\mathrm{III}}\end{Bmatrix}; \tag{34b}$$

$$\boldsymbol{\alpha}_{11}=\frac{1}{2}\mathbf{T}_{\mathbf{R}}^{+}\begin{bmatrix}(2-\gamma)\boldsymbol{\alpha}_{0\mathrm{I}}\mathbf{R}_1 & \gamma\boldsymbol{\alpha}_{0\mathrm{I}}\mathbf{R}_1\\ (1-\gamma)\boldsymbol{\alpha}_{0\mathrm{II}}\mathbf{R}_1 & (1+\gamma)\boldsymbol{\alpha}_{0\mathrm{II}}\mathbf{R}_1\end{bmatrix};\quad \boldsymbol{\alpha}_{12}=\frac{1}{2}\mathbf{T}_{\mathbf{R}}^{+}\begin{bmatrix}\mathbf{0} & -\boldsymbol{\alpha}_{0\mathrm{I}}\mathbf{R}_1 & -\boldsymbol{\alpha}_{0\mathrm{I}}\mathbf{R}_1\\ \mathbf{0} & \mathbf{0} & \mathbf{0}\end{bmatrix};$$

$$\boldsymbol{\alpha}_{13}=\frac{1}{2}\mathbf{T}_{\mathbf{R}}^{+}\begin{bmatrix}\mathbf{0} & \mathbf{0} & \mathbf{0}\\ -\boldsymbol{\alpha}_{0\mathrm{II}}\mathbf{R}_1 & -\boldsymbol{\alpha}_{0\mathrm{II}}\mathbf{R}_1 & \mathbf{0}\end{bmatrix};\quad \boldsymbol{\alpha}_{21}=\frac{1}{2}\mathbf{T}_{\mathbf{R}}^{l-}\begin{bmatrix}(2-\gamma)\boldsymbol{\alpha}_{0\mathrm{I}}\mathbf{R}_1 & \gamma\boldsymbol{\alpha}_{0\mathrm{I}}\mathbf{R}_1\\ \mathbf{0} & \mathbf{0}\end{bmatrix};$$

$$\boldsymbol{\alpha}_{22}=\frac{1}{2}\mathbf{T}_{\mathbf{R}}^{l-}\begin{bmatrix}\mathbf{0} & -\boldsymbol{\alpha}_{0\mathrm{I}}\mathbf{R}_1 & -\boldsymbol{\alpha}_{0\mathrm{I}}\mathbf{R}_1\\ -\boldsymbol{\alpha}_{0\mathrm{III}}\mathbf{R}_2 & -\boldsymbol{\alpha}_{0\mathrm{III}}\mathbf{R}_2 & \mathbf{0}\end{bmatrix};\quad \boldsymbol{\alpha}_{23}=\frac{1}{2}\mathbf{T}_{\mathbf{R}}^{l-}\begin{bmatrix}\mathbf{0} & \mathbf{0} & \mathbf{0}\\ \mathbf{0} & \boldsymbol{\alpha}_{0\mathrm{III}}\mathbf{R}_2 & \boldsymbol{\alpha}_{0\mathrm{III}}\mathbf{R}_2\end{bmatrix}; \tag{34c}$$

$$\boldsymbol{\alpha}_{31}=\frac{1}{2}\mathbf{T}_{\mathbf{R}}^{r-}\begin{bmatrix}(1-\gamma)\boldsymbol{\alpha}_{0\mathrm{II}}\mathbf{R}_1 & (1+\gamma)\boldsymbol{\alpha}_{0\mathrm{II}}\mathbf{R}_1\\ \mathbf{0} & \mathbf{0}\end{bmatrix};\quad \boldsymbol{\alpha}_{32}=\frac{1}{2}\mathbf{T}_{\mathbf{R}}^{r-}\begin{bmatrix}\mathbf{0} & \mathbf{0} & \mathbf{0}\\ -\boldsymbol{\alpha}_{0\mathrm{III}}\mathbf{R}_2 & -\boldsymbol{\alpha}_{0\mathrm{III}}\mathbf{R}_2 & \mathbf{0}\end{bmatrix};$$

$$\boldsymbol{\alpha}_{33}=\frac{1}{2}\mathbf{T}_{\mathbf{R}}^{r-}\begin{bmatrix}-\boldsymbol{\alpha}_{0\mathrm{II}}\mathbf{R}_1 & -\boldsymbol{\alpha}_{0\mathrm{II}}\mathbf{R}_1 & \mathbf{0}\\ \mathbf{0} & \boldsymbol{\alpha}_{0\mathrm{III}}\mathbf{R}_2 & \boldsymbol{\alpha}_{0\mathrm{III}}\mathbf{R}_2\end{bmatrix}$$

Substituting Eqn (34a) into expressions (b, d, and f) in Eqns (31) and solving the internal displacements as functions of the regular (external) nodal displacements.

$$\begin{bmatrix}\mathbf{L}_{22}^{+}-\boldsymbol{\alpha}_{11} & -\boldsymbol{\alpha}_{12} & -\boldsymbol{\alpha}_{13}\\ -\boldsymbol{\alpha}_{21} & \mathbf{L}_{22}^{l-}-\boldsymbol{\alpha}_{22} & -\boldsymbol{\alpha}_{23}\\ -\boldsymbol{\alpha}_{31} & -\boldsymbol{\alpha}_{32} & \mathbf{L}_{22}^{r-}-\boldsymbol{\alpha}_{33}\end{bmatrix}\begin{Bmatrix}\mathbf{d}_{6'5'}\\ \mathbf{d}_{786}\\ \mathbf{d}_{58'7'}\end{Bmatrix}=\begin{Bmatrix}\mathbf{S}_1\\ \mathbf{S}_2\\ \mathbf{S}_3\end{Bmatrix}+\begin{bmatrix}\mathbf{0} & \mathbf{0} & -\mathbf{L}_{21}^{+}\\ -\mathbf{L}_{21}^{l-} & \mathbf{0} & \mathbf{0}\\ \mathbf{0} & -\mathbf{L}_{21}^{r-} & \mathbf{0}\end{bmatrix}\begin{Bmatrix}\mathbf{d}_{ext}^{l-}\\ \mathbf{d}_{ext}^{r-}\\ \mathbf{d}_{ext}^{+}\end{Bmatrix} \tag{35}$$

The internal nodal displacements can be further expressed explicitly as functions of external nodal displacements as below:

$$
\begin{Bmatrix} \mathbf{d}_{6'5'} \\ \mathbf{d}_{786} \\ \mathbf{d}_{58'7'} \end{Bmatrix} = \begin{bmatrix} \mathbf{Y}_7 & \mathbf{Y}_8 & \mathbf{Y}_9 \\ \mathbf{Y}_4 & \mathbf{Y}_5 & \mathbf{Y}_6 \\ \mathbf{Y}_1 & \mathbf{Y}_2 & \mathbf{Y}_3 \end{bmatrix} \begin{Bmatrix} \mathbf{S}_1 \\ \mathbf{S}_2 \\ \mathbf{S}_3 \end{Bmatrix} + \begin{bmatrix} \mathbf{X}_{13} & \mathbf{X}_{14} & \mathbf{X}_{15} \\ \mathbf{X}_{10} & \mathbf{X}_{11} & \mathbf{X}_{12} \\ \mathbf{X}_7 & \mathbf{X}_8 & \mathbf{X}_9 \end{bmatrix} \begin{Bmatrix} \mathbf{d}_{ext}^{l-} \\ \mathbf{d}_{ext}^{r-} \\ \mathbf{d}_{ext}^{+} \end{Bmatrix} \tag{36}
$$

where the matrices $\mathbf{X}_p$ (p = 1, 2, .. 15) and $\mathbf{Y}_q$ (q = 1, 2, .. 9) can be found in [21].

Finally, by substituting Eqn (36) into Eqn (31a, 31c, and 31e) to eliminate the internal nodal displacements, the fully condensed elemental equilibrium equation is obtained as

$$
\begin{bmatrix} \mathbf{L}_{11}^{l-} + \mathbf{L}_{12}^{l-}\mathbf{X}_{10} & \mathbf{L}_{12}^{l-}\mathbf{X}_{11} & \mathbf{L}_{12}^{l-}\mathbf{X}_{12} \\ \mathbf{L}_{12}^{r-}\mathbf{X}_7 & \mathbf{L}_{11}^{r-} + \mathbf{L}_{12}^{r-}\mathbf{X}_8 & \mathbf{L}_{12}^{r-}\mathbf{X}_9 \\ \mathbf{L}_{12}^{+}\mathbf{X}_{13} & \mathbf{L}_{12}^{+}\mathbf{X}_{14} & \mathbf{L}_{11}^{+} + \mathbf{L}_{12}^{+}\mathbf{X}_{15} \end{bmatrix} \begin{Bmatrix} \mathbf{d}_{ext}^{l-} \\ \mathbf{d}_{ext}^{r-} \\ \mathbf{d}_{ext}^{+} \end{Bmatrix} = \begin{Bmatrix} \mathbf{F}_{ext}^{l-} \\ \mathbf{F}_{ext}^{r-} \\ \mathbf{F}_{ext}^{+} \end{Bmatrix} - \begin{bmatrix} \mathbf{L}_{12}^{l-}\mathbf{Y}_4 & \mathbf{L}_{12}^{l-}\mathbf{Y}_5 & \mathbf{L}_{12}^{l-}\mathbf{Y}_6 \\ \mathbf{L}_{12}^{r-}\mathbf{Y}_1 & \mathbf{L}_{12}^{r-}\mathbf{Y}_2 & \mathbf{L}_{12}^{r-}\mathbf{Y}_3 \\ \mathbf{L}_{12}^{+}\mathbf{Y}_7 & \mathbf{L}_{12}^{+}\mathbf{Y}_8 & \mathbf{L}_{12}^{+}\mathbf{Y}_9 \end{bmatrix} \begin{Bmatrix} \mathbf{S}_1 \\ \mathbf{S}_2 \\ \mathbf{S}_3 \end{Bmatrix} \tag{37}
$$

Note that Eqn (36) and Eqn (37) share the same matrices $\mathbf{X}_p$ (p = 1, 2, …15), $\mathbf{Y}_q$ (q = 1, 2,…9),), and $\boldsymbol{S}_r$ (r = 1, 2, 3), which are all functions of the characteristic cohesive stresses $(\boldsymbol{\sigma}_{0\mathrm{I}}, \boldsymbol{\sigma}_{0\mathrm{II}}, \text{ and } \boldsymbol{\sigma}_{0\mathrm{III}})^{(i,j,k,l,m,n)}$ (Eqn 32b) and the cohesive stiffnesses $(\boldsymbol{\alpha}_{0\mathrm{I}}, \boldsymbol{\alpha}_{0\mathrm{II}}, \text{ and } \boldsymbol{\alpha}_{0\mathrm{III}})^{(i,j,k,l,m,n)}$ (Eqn 32c). They are not known at this point because the crack displacements are not known yet. The solving procedure for these equations will be discussed in next section 3.3.

3.3 Consistency-check Based Elemental Condensation Algorithm

In section 3.1 and 3.2, the elemental equilibrium equations for single crack (Eqn 29) and for two interactive cracks (Eqn 37) have been derived. However, these nonlinear equations have yet to be solved. In literature, Eqn (29) or Eqn (37) is typically re-formulated into an incremental form and then solved with either the direct matrix inversion technique [50, 51, 53] or a Newton-Raphson type of iterative solver [49, 75, 76]. This is known as the static condensation process.

In this paper, the explicit nature of the solutions enables a very efficient elemental condensation process that is completely different from what have been used in literature. Instead of solving the incremental form of the elemental equilibrium of Eqn (29) or Eqn (37), in this paper we first solve the internal nodal displacements (Eqn (28) or Eqn (36)) analytically through a simple consistency checking procedure. It will be shown that once these equations are solved, the equilibrium equations (Eqn (29) or (37)) are satisfied with mathematical exactness by substituting the related matrices into them.

<u>Single Intra-Elemental Crack</u>

In this case, the internal crack displacements have been given in Eqn (28). It is noted that, once Eqn (28a) is solved, i.e., $\mathbf{S}_0, \mathbf{A}$, $\mathbf{B}$, $\boldsymbol{\Psi}_{22}^{+}$, and $\boldsymbol{\Psi}_{22}^{-}$ are established, simply substituting these matrices into Eqn (29) will guarantee the elemental equilibrium. We first convert the global crack displacements in Eqn (28a) into local crack displacements using Eqn (26b), which gives

$$
\begin{Bmatrix} \delta_{s66'} \\ \delta_{n66'} \\ \delta_{s55'} \\ \delta_{n55'} \end{Bmatrix} = \mathrm{Diag}\left[\mathbf{R}_1^{\mathbf{T}};\mathbf{R}_1^{\mathbf{T}}\right]\begin{pmatrix} -l_{e1}\left(\mathbf{A}^{-1}+\mathbf{B}^{-1}-l_{e1}\mathbf{A}^{-1}\boldsymbol{\alpha}(\boldsymbol{\Psi}_{22}^{-})^{-1}+l_{e1}\mathbf{B}^{-1}\boldsymbol{\alpha}(\boldsymbol{\Psi}_{22}^{+})^{-1}\right)\mathbf{S}_0 \\ +\left(\mathbf{B}^{-1}-l_{e1}\mathbf{A}^{-1}\boldsymbol{\alpha}(\boldsymbol{\Psi}_{22}^{-})^{-1}\right)\mathbf{L}_{21}^{-}\mathbf{d}_{ext}^{-}+\left(l_{e1}\mathbf{B}^{-1}\boldsymbol{\alpha}(\boldsymbol{\Psi}_{22}^{+})^{-1}-\mathbf{A}^{-1}\right)\mathbf{L}_{21}^{+}\mathbf{d}_{ext}^{+} \end{pmatrix}^{(i,j,k,l)} \tag{38}
$$

In Eqn (38) the superscripts (i, j, k, l) in the right-hand-side are included to emphasize that the matrices $\mathbf{S}_0, \mathbf{A}$, $\mathbf{B}$, $\boldsymbol{\Psi}_{22}^{+}$, and $\boldsymbol{\Psi}_{22}^{-}$ are all functions of the cohesive slope matrix $\boldsymbol{\alpha}_0^{(i,j,k,l)}$ and characteristic stress matrix $\boldsymbol{\sigma}_0^{(i,j,k,l)}$ (Eqn 26c & 28b). Thus, for any trial cohesive segment combination (i, j, k, l), a set of local crack displacements is immediately solved from Eqn (38). The solved local crack displacements are then subjected to a consistency check, and *the true solution is found if the following statement is true*

$$
\boxed{(\delta_{s66'} \in \overleftrightarrow{\delta_s}^{(i)} \text{is true}) \;\&\&\; (\delta_{n66'} \in \overleftrightarrow{\delta_n}^{(j)} \text{is true}) \;\&\&\; (\delta_{s55'} \in \overleftrightarrow{\delta_s}^{(k)} \text{is true}) \;\&\&\; (\delta_{n55'} \in \overleftrightarrow{\delta_n}^{(l)} \text{is true})}
$$

where $\overleftrightarrow{\delta_s}^{(i)}$, $\overleftrightarrow{\delta_n}^{(j)}$, $\overleftrightarrow{\delta_s}^{(k)}$ and $\overleftrightarrow{\delta_s}^{(l)}$ are the respective crack displacement ranges of the assumed segments (i, j, k, l) (Section 2.2).

This is the core idea behind the solving algorithm used in this paper. The mathematical exactness (in piece-wise linear sense) of the solution is guaranteed by the solution uniqueness of the local problem (the solution uniqueness for linear material with nonlinear discontinuities has been discussed in [77]). The detailed algorithm formulation and extended discussions on its numerical performance in solving fracture problems can be found in [78].

<u>Two Intra-Elemental Cracks</u>

In this case, the crack displacements as explicit functions of external displacements (such as the Eqn (38) for the single crack case) are not readily available. However, the solving procedure presented above remains applicable in solving the internal displacement equation of Eqn (36a). The equation is repeated below with superscripts added to emphasize the dependence of $\mathbf{X}_p$ (p = 1, 2, .. 15), $\mathbf{Y}_q$ (q = 1, 2, .. 9), and $\boldsymbol{S}_r$ (r = 1, ..3) on the cohesive segment combination (i, j, k, l, m, n)

.

$$
\begin{Bmatrix} \mathbf{d}_{6'5'} \\ \mathbf{d}_{786} \\ \mathbf{d}_{58'7'} \end{Bmatrix} = \left(\begin{bmatrix} \mathbf{Y}_7 & \mathbf{Y}_8 & \mathbf{Y}_9 \\ \mathbf{Y}_4 & \mathbf{Y}_5 & \mathbf{Y}_6 \\ \mathbf{Y}_1 & \mathbf{Y}_2 & \mathbf{Y}_3 \end{bmatrix}\begin{Bmatrix} \mathbf{S}_1 \\ \mathbf{S}_2 \\ \mathbf{S}_3 \end{Bmatrix}\right)^{(i,j,k,l,m,n)} + \begin{bmatrix} \mathbf{X}_{13} & \mathbf{X}_{14} & \mathbf{X}_{15} \\ \mathbf{X}_{10} & \mathbf{X}_{11} & \mathbf{X}_{12} \\ \mathbf{X}_7 & \mathbf{X}_8 & \mathbf{X}_9 \end{bmatrix}^{(i,j,k,l,m,n)} \begin{Bmatrix} \mathbf{d}_{ext}^{l-} \\ \mathbf{d}_{ext}^{r-} \\ \mathbf{d}_{ext}^{+} \end{Bmatrix} \tag{39}
$$

For a trial cohesive segment combination (i, j, k, l, m, n) and given external nodal displacements, a set of solution to the internal nodal displacements, $\mathbf{d}_{6'5'} = \left\{\mathbf{d}_{6'}, \mathbf{d}_{5'}\right\}^{\mathbf{T}}$, $\mathbf{d}_{786} = \left\{\mathbf{d}_7, \mathbf{d}_8, \mathbf{d}_6\right\}^{\mathbf{T}}$, and $\mathbf{d}_{58'7'} = \left\{\mathbf{d}_5, \mathbf{d}_{8'}, \mathbf{d}_{7'}\right\}^{\mathbf{T}}$, is immediately solved from Eqn (39). Then, the crack displacements at the

integration point of each segment (points I, II, and III in Figure 4) are computed and converted to local coordinates, i. e.,

$$\begin{cases} \{\delta_{\mathrm{sI}},\delta_{\mathrm{nI}}\}^{\mathbf{T}} = \mathbf{R}_1^{\mathbf{T}}\left((1-\gamma/2)\mathbf{d}_{6'} + (\gamma/2)\mathbf{d}_{5'} - \left(\mathbf{d}_6+\mathbf{d}_8\right)/2\right)^{(i,j,k,l,m,n)} \\ \{\delta_{\mathrm{sII}},\delta_{\mathrm{nII}}\}^{\mathbf{T}} = \mathbf{R}_1^{\mathbf{T}}\left((1-\gamma/2)\mathbf{d}_{6'} + (1+\gamma)/2\mathbf{d}_{5'} - \left(\mathbf{d}_5+\mathbf{d}_{8'}\right)/2\right)^{(i,j,k,l,m,n)} \\ \{\delta_{\mathrm{sIII}},\delta_{\mathrm{nIII}}\}^{\mathbf{T}} = \mathbf{R}_2^{\mathbf{T}}\left((\mathbf{d}_{7'}+\mathbf{d}_{8'})/2 - (\mathbf{d}_7+\mathbf{d}_8)/2\right)^{(i,j,k,l,m,n)} \end{cases} \tag{40}$$

The local crack displacements are then subjected to a consistency check similar to the single crack case and the exact solution is found when the following statement is true.

$$\boxed{\begin{gathered}(\delta_{sI} \in \overleftrightarrow{\delta}_s^{(i)} \text{ true}) \;\&\&\; (\delta_{nI} \in \overleftrightarrow{\delta}_n^{(j)} \text{ true}) \;\&\&\; (\delta_{sII} \in \overleftrightarrow{\delta}_s^{(\mathrm{k})} \text{ true}) \;\&\&\; (\delta_{nII} \in \overleftrightarrow{\delta}_n^{(l)} \text{ true}) \\ \&\&\; (\delta_{sIII} \in \overleftrightarrow{\delta}_s^{(m)} \text{ true}) \;\&\&\; (\delta_{nIII} \in \overleftrightarrow{\delta}_n^{(n)} \text{ true})\end{gathered}}$$

Once the solution is found, $\mathbf{X}_p$ (p = 1, 2, …15), $\mathbf{Y}_q$ (q = 1, 2, …9), and $\boldsymbol{S}_r$ (r = 1, 2, 3) are all established with the determined (i, j, k, l, m, n). Substituting them into Eqn (29) the fully condensed elemental equilibrium is then satisfied with mathematical exactness (in piece-wise linear sense and within the limit of FE discretization accuracy).

3.4 Numerical Implementation

The new A-FEM and the solving procedure above can be integrated into any standard FE programs as a general purposed element because the elemental locality is completely retained. Here we briefly describe how to implement it into an existing FE program as an element.

For any displacement based FEM programs, the external nodal displacements are passed into the element to establish: 1) instantaneous element stiffness matrix or Jacobian matrix, and 2) the external force array (also called right-hand-side or RHS). Both matrices have been derived and solved explicitly in section 3.1 for single crack case (Eqn 29) and in section 3.2 for two intra-elemental cracks (Eqn 37).

The local crack displacements were saved as solution-dependent variables (or state variables) and subjected to constant updates so that their maximum values ever experienced were always available for assessing loading or unloading condition (for consistency check). Another minor issue is to guarantee the deformation continuity across the element edge that is shared by a crack-tip element and the element immediately ahead of it, which is a standard continuous element. This was conveniently done in this paper by enforcing the internal nodal displacements at the edge to be $\mathbf{d}_5 = \mathbf{d}_{5'} = N_A\mathbf{d}_A + N_B\mathbf{d}_B$, where 5 and 5' are the internal nodes at the crack-tip; A and B are the two external nodes of the element edge hosting the crack-tip; and N_A and N_B are the standard line shape functions associated with node A and B.

One of the advantages of this method is that it does not need a sophisticated global tracking algorithm such as the level-set functions in the X-FEM for a propagating crack, which requires heavy calculations when implemented in a narrow band manner. However, it is beneficial to record

the crack path so that the inter-element continuity of a crack is reinforced. This was done with a common block accessible to all user elements, within which the geometric information of a crack is constantly updated as it propagates. A detailed data structure and propagation rules regarding multiple crack interaction has been given in detail in [21].

We note that the new A-FEM only needs to record the cracks developed in response to the local stress conditions. There is no need to actively assign an incremental crack length for crack extension. The crack initiation in an element is purely determined by the local stresses in the crack front element accordingly to a specified initiation criterion (such as the maximum principal stress criterion used in the following numerical examples in section 4). The propagation is purely determined by the cohesive crack propagation rule of Eqn (15).

4. 3-D A-FEM FORMULATION

Extension of the 2D A-FEM formulation to 3D is relatively straightforward. Here we briefly present the 3D A-FEM for the 4-node tetrahedron element as shown in Figure 5 (a). [79]. There are two possible configurations if the element is cut by a crack surface; i) the element is cut into one tetrahedron subdomain and one wedge subdomain as shown in Fig 5(b), and ii) the element is cut into two wedge subdomains as shown in Fig (5c).

The tetrahedron-wedge configuration with the triangular crack plane (Figure 5(b)) has 6 internal nods as 5, 6, 7, 5', 6' and 7' while the wedge-wedge configuration with quadrilateral crack plane has 8 internal nodes 5, 6, 7, 8, 5', 6',7' and 8'. Displacement jumps across the cohesive crack is simply the difference in displacements between node-pair 5-5', 6-6', 7-7', and 8-8'. Defining a local coordinate system as shown in Fig 5(d) with the surface out-normal ($\vec{\mathbf{N}}$) as the local z-axis, the rotation matrix can be obtained as

$$\mathbf{R} = \begin{bmatrix} l_1 & m_1 & n_1 \\ l_2 & m_2 & n_2 \\ l_3 & m_3 & n_3 \end{bmatrix} \tag{41a}$$

where l_i, m_j and n_k $(i, j, k = 1,2,3)$ are the direction cosines of the crack plane with $\vec{\mathbf{N}} = l_1\vec{i} + m_1\vec{j} + n_1\vec{k}$ being the out-normal direction, $\vec{\mathbf{T}} = l_2\vec{i} + m_2\vec{j} + n_2\vec{k}$ and $\vec{\mathbf{S}} = n_1\vec{i} + n_2\vec{j} + n_3\vec{k}$ being the two orthogonal in-plane shear directions, and

$$l_i = Cos\alpha_i, \quad m_i = Cos\beta_i, \quad n_i = Cos\gamma_i \quad (i = 1,2,3)\,. \tag{41b}$$

α_i, β_i, and γ_i are the angles between the local axes and global axes as illustrated in Figure 5(d).

Following the similar procedure of 2D-AFEM in section 3.1, the local equilibrium equation can be written as the identical form of Eqn (19):

$$\begin{cases} \begin{bmatrix} \mathbf{L}_{11}^{+} & \mathbf{L}_{12}^{+} \\ \mathbf{L}_{21}^{+} & \mathbf{L}_{22}^{+} \end{bmatrix} \begin{Bmatrix} \mathbf{d}_{ext}^{+} \\ \mathbf{d}_{\text{int}}^{+} \end{Bmatrix} = \begin{Bmatrix} \mathbf{F}_{ext}^{+} \\ \mathbf{F}_{\text{int}}^{+} \end{Bmatrix} \\ \begin{bmatrix} \mathbf{L}_{11}^{-} & \mathbf{L}_{12}^{-} \\ \mathbf{L}_{21}^{-} & \mathbf{L}_{22}^{-} \end{bmatrix} \begin{Bmatrix} \mathbf{d}_{ext}^{-} \\ \mathbf{d}_{\text{int}}^{-} \end{Bmatrix} = \begin{Bmatrix} \mathbf{F}_{ext}^{-} \\ \mathbf{F}_{\text{int}}^{-} \end{Bmatrix} \end{cases} \tag{42}$$

The only differences between Eqn (19) and (42) are the dimension of the submatrices and the definition of external and internal DoFs and forces. For the tetrahedron-wedge cut configuration (Fig 5a),

$$\begin{aligned}&\mathbf{F}_{\mathrm{ext}}^{+}=\mathbf{F}_{4};\ \ \mathbf{F}_{\mathrm{ext}}^{-}=\mathbf{F}_{123};\ \ \mathbf{d}_{\mathrm{ext}}^{+}=\mathbf{d}_{4};\ \ \mathbf{d}_{\mathrm{ext}}^{-}=\mathbf{d}_{123}\\&\mathbf{F}_{\mathrm{int}}^{+}=\mathbf{F}_{5'6'7'};\ \ \mathbf{F}_{\mathrm{int}}^{-}=\mathbf{F}_{567};\ \ \mathbf{d}_{\mathrm{int}}^{+}=\mathbf{d}_{5'6'7'};\ \ \mathbf{d}_{\mathrm{int}}^{-}=\mathbf{d}_{567}\end{aligned},$$

and for the wedge-wedge cut configuration (Fig 5b),

$$\begin{aligned}&\mathbf{F}_{\mathrm{ext}}^{+}=\mathbf{F}_{34};\ \ \mathbf{F}_{\mathrm{ext}}^{-}=\mathbf{F}_{12};\ \ \mathbf{d}_{\mathrm{ext}}^{+}=\mathbf{d}_{34};\ \ \mathbf{d}_{\mathrm{ext}}^{-}=\mathbf{d}_{12}\\&\mathbf{F}_{\mathrm{int}}^{+}=\mathbf{F}_{5'6'7'8'};\ \ \mathbf{F}_{\mathrm{int}}^{-}=\mathbf{F}_{5678};\ \ \mathbf{d}_{\mathrm{int}}^{+}=\mathbf{d}_{5'6'7'8'};\ \ \mathbf{d}_{\mathrm{int}}^{-}=\mathbf{d}_{5678}\end{aligned}.$$

The internal force array integrated from cohesive stresses between the cohesive crack surfaces can be written as

$$\mathbf{F}_{\mathrm{int}}^{-}=-\mathbf{F}_{\mathrm{int}}^{+}=A_{e}\left(\mathbf{S_0}+\boldsymbol{\alpha}\cdot\Delta\mathbf{d}_{\mathrm{int}}\right), \tag{43a}$$

where A_e is the area of the crack surface. $\mathbf{S_0}$ and $\boldsymbol{\alpha}$ are the characteristic stress and cohesive stiffness matrix similar to those in Eqn (26). For the tetrahedron-wedge cut configuration,

$$\begin{aligned}&\mathbf{S_0}=\mathrm{Diag}[\mathbf{R}^{\mathrm{T}};\mathbf{R}^{\mathrm{T}};\mathbf{R}^{\mathrm{T}}](\mathbf{T_{coh}})^{\mathrm{T}}\boldsymbol{\sigma_0}\\&\boldsymbol{\alpha}=\mathrm{Diag}[\mathbf{R^T};\ \mathbf{R^T};\ \mathbf{R^T}]\ (\mathbf{T}_{\mathrm{coh}})^{\mathbf{T}}\ \boldsymbol{\alpha}_0\ \mathbf{N}_{\mathrm{coh}}\ \mathrm{Diag}[\mathbf{R};\ \mathbf{R};\mathbf{R}]\\&\boldsymbol{\sigma_0}=\left\{\hat{\tau}_s^{(i)}-\alpha_s^{(i)}\delta_s^{(i)};\hat{\tau}_t^{(j)}-\alpha_t^{(j)}\delta_t^{(j)};\hat{\sigma}^{(k)}-\alpha_n^{(k)}\delta_n^{(k)};\ \ \cdots;\ \ \hat{\sigma}^{(q)}-\alpha_n^{(q)}\delta_n^{(q)}\right\}^{\mathrm{T}};\\&\boldsymbol{\alpha}_0=\mathrm{Diag}[\alpha_{\mathrm{s}}^{(\mathrm{i})};\alpha_{\mathrm{t}}^{(\mathrm{j})};\alpha_{\mathrm{n}}^{(\mathrm{k})};\alpha_{\mathrm{s}}^{(\mathrm{l})};\alpha_{\mathrm{t}}^{(\mathrm{m})};\alpha_{\mathrm{n}}^{(\mathrm{n})}\ \ \ \alpha_{\mathrm{s}}^{(\mathrm{o})};\alpha_{\mathrm{t}}^{(\mathrm{p})};\alpha_{\mathrm{n}}^{(\mathrm{q})}]\end{aligned} \tag{43b}$$

where $\mathbf{T_{coh}}$ and $\mathbf{N}_{\mathrm{coh}}$ are the respective integration and interpolation matrix for the 3-node cohesive crack surface. Each of the free indices (*i*,*j*,*k*,*l*,*m*,*n*,*o*,*p*,*q*) can range from 1-4 for the cohesive law shown in Figure 2.

For the wedge-wedge cut configuration,

$$\begin{aligned}&\mathbf{S_0}=\mathrm{Diag}[\mathbf{R}^{\mathrm{T}};\mathbf{R}^{\mathrm{T}};\mathbf{R}^{\mathrm{T}};\mathbf{R}^{\mathrm{T}}](\mathbf{T_{coh}})^{\mathrm{T}}\boldsymbol{\sigma_0}\\&\boldsymbol{\alpha}=\mathrm{Diag}[\mathbf{R^T};\ \mathbf{R^T};\ \mathbf{R^T};\mathbf{R}^{\mathrm{T}}]\ (\mathbf{T}_{\mathrm{coh}})^{\mathbf{T}}\ \boldsymbol{\alpha}_0\ \mathbf{N}_{\mathrm{coh}}\ \mathrm{Diag}[\mathbf{R};\ \mathbf{R};\mathbf{R};\mathbf{R}]\\&\boldsymbol{\sigma_0}=\left\{\hat{\tau}_s^{(i)}-\alpha_s^{(i)}\delta_s^{(i)};\hat{\tau}_t^{(j)}-\alpha_t^{(j)}\delta_t^{(j)};\hat{\sigma}^{(k)}-\alpha_n^{(k)}\delta_n^{(k)};\ \ \cdots;\ \ \hat{\sigma}^{(t)}-\alpha_n^{(t)}\delta_n^{(t)}\right\}^{\mathrm{T}};\\&\boldsymbol{\alpha}_0=\mathrm{Diag}[\alpha_{\mathrm{s}}^{(\mathrm{i})};\alpha_{\mathrm{t}}^{(\mathrm{j})};\alpha_{\mathrm{n}}^{(\mathrm{k})};\alpha_{\mathrm{s}}^{(\mathrm{l})};\alpha_{\mathrm{t}}^{(\mathrm{m})};\alpha_{\mathrm{n}}^{(\mathrm{n})};\alpha_{\mathrm{s}}^{(\mathrm{o})};\alpha_{\mathrm{t}}^{(\mathrm{p})};\alpha_{\mathrm{n}}^{(\mathrm{q})};\alpha_{\mathrm{s}}^{(\mathrm{r})};\alpha_{\mathrm{t}}^{(\mathrm{s})};\alpha_{\mathrm{n}}^{(\mathrm{t})}]\end{aligned} \tag{43c}$$

In this case $\mathbf{T_{coh}}$ and $\mathbf{N}_{\mathrm{coh}}$ are the respective integration and interpolation matrix for the 4-node cohesive surface. Each of the free indices (*i*,*j*,*k*,*l*,*m*,*n*,*o*,*p*,*q*,*r*,*s*,*t*) can range from 1-4 for the cohesive law shown in Figure 2.

With the characteristic stress, cohesive stiffness, interpolation and integration matrices fully defined, the equation that relates internal displacements to the external displacements, and the equation of elemental equilibrium are found to be in exactly the same matrix form of Eqn (28) and (29), respectively. Thus the consistency-check based procedure for elemental condensation as described in section 3.3 can be readily applied to solve the element equibrium.

One of the biggest challenges in 3D fracture modeling is to maintain the conformity of the evolving crack surface. A crack surface tracking scheme is absolutely necessary and proper numerical treatments have to be done to guarantee that the crack surface, which may cut multiple elements before they merge at some point, maintains a relatively smooth planar configuration without too much out-of-plane oscillation. Several crack tracking schemes such as local and global tracking algorithms have been developed in the literature [80-83]. Here we adopt the local tracking algorithm first proposed by Aries and Belytschko [80]. The detailed algorithm will not be given here but interested readers are referred to [80].

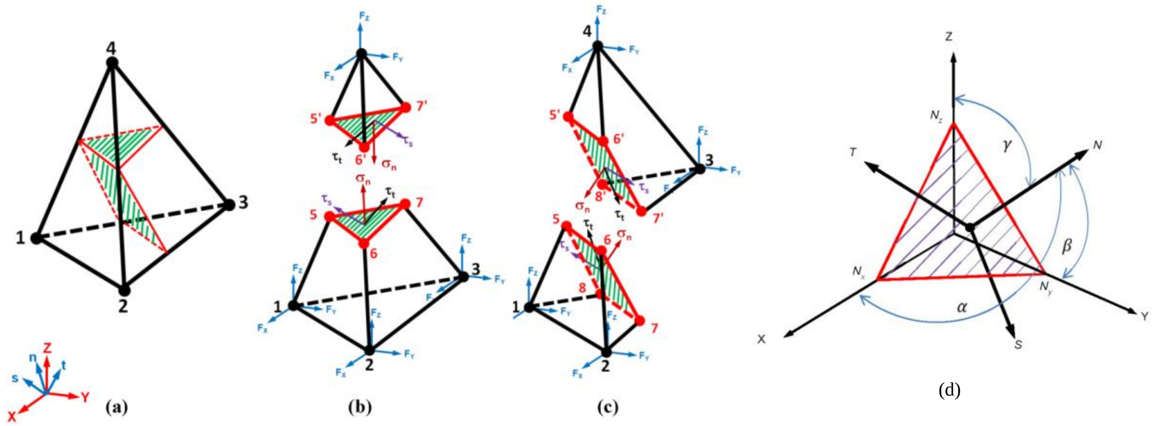

Figure 5: Element illustration for (a) a regular 4-node tetrahedron element with two possible cut configurations by a crack plane, (b) the A-FE with tetrahedron-wedge configuration, (c) the A-FE with wedge-wedge configuration, (d) definition of local coordinates for the crack plane.

5. DEALING WITH MATERIAL ORTHOTROPY AND NONLINEARITY

A majority of modern composites are highly orthotropic due to the directional reinforcement structures. The material orthotropy is not only reflected in the orthotropic elastic constants, but also in their progressive damage modes, i.e., matrix tension and compression failure, fiber direction tensile rupture and compressive kinking, shear failure, and interlaminar delamination. The various failure modes can appear simultaneously but their interactions have not been fully studied due to lack of analytical tools. Furthermore, it has been shown that typical polymer matrix composites exhibit various nonlinearity at continuum level (i.e., before initiation of discrete cracks). These include strong shear nonlinearity, asymmetric tensile and compressive modulus, and often times with strong nonlinear stress-strain relation under longitudinal and transverse compression [29, 84, 85]. While the strong influence of the shear nonlinearity on interlaminar delamination has been well appreciated [9, 13, 20, 86, 87], overall the complex interaction between such material nonlinearity and the intra-ply damage initiation and propagation

has not been well studied, largely due to the lack of high-fidelity analytical means to couple them into a single analysis. In this study, the following nonlinearities were explicit considered:

5.1 Asymmetric Tension/Compression in Longitudinal and Transverse Direction

Based on experimental evidence, the stress-strain relation under longitudinal or transverse tension is typically linear elastic until the respective strength value (X_t or Y_t) is reached. This is represented with a tensile modulus, i.e., E_{1T} for longitudinal tension or E_{2T} for transverse tension. Under longitudinal or transverse compression, however, typical PMCs exhibit relatively strong nonlinearity in the stress-strain relation up to the respective strength value (X_c or Y_c), as shown in Figure 6(a). In this paper, the full stress-strain relation is written as follows

$$\sigma_k\left(\varepsilon_k\right)=\begin{cases} E_{kT}\ \varepsilon_k & \varepsilon_k \geq 0 \\ E_{kC}\ \varepsilon_k & \varepsilon_k^0 \leq \varepsilon_k < 0 \qquad (k=1 \text{ or } 2) \\ \dfrac{E_{kC}\varepsilon_k}{\left[1+\left|E_{kC}\varepsilon_k / \sigma_k^0\right|^{n_k}\right]^{(1/n_k)}} & \varepsilon_k < \varepsilon_k^0 \end{cases} \tag{44}$$

where the subscript k = 1 stands for longitudinal response and k = 2 refers to transverse response. E_{kC} is the compressive modulus and ε_k^0 is the elastic limiting strain in compression. σ_k^0 is an asymptotic stress and n_k is a power index. They control the shape of the nonlinear constitutive relation and have to be characterized from experiments. The nonlinear constitutive relation was implemented as a damage model (Chapery model), i.e., the instantaneous secant modulus derived from Eqn (44) was used to form the material stiffness matric ($\mathbf{D}$ matrix in Eqn 18) and, upon unloading at a strain $\varepsilon_k^* > \varepsilon_k^0$, the unloading path points directly towards the origin (Fig 6a).

5.2 Shear Nonlinearity

Similar nonlinear model was used to account for the shear nonlinearity, as shown in Figure 6(b). The shear stress-strain curve can be written as:

$$\tau_{12}\left(\gamma_{12}\right)=\begin{cases} G_{12}^0\ \gamma_{12} & \left|\gamma_{12}\right| \leq \gamma_{12}^0 \\ \dfrac{G_{12}^0\ \gamma_{12}}{\left(1+\left|G_{12}^0\ \gamma_{12} / \tau_{12}^0\right|^{n_g}\right)^{(1/n_g)}} & \left|\gamma_{12}\right| > \gamma_{12}^0 \end{cases} \tag{45}$$

Where G_{12}^0 is the elastic shear modulus and γ_{12}^0 the elastic limiting shear strain. τ_{12}^0 is an asymptotic shear stress and n_g is a power index. They control the shape of the nonlinear constitutive relation and have to be fitted from experimental data. The nonlinear shear stress-strain relation was also implemented as a damage model (Chapery model), i.e., the instantaneous secant modulus derived from Eqn (45) was used to form the material stiffness matrix (i.e., the $\mathbf{D}$ matrix

in Eqn 18), and upon unloading at a strain $\left|\gamma_{12}^{*}\right| > \gamma_{12}^{0}$, the unloading path points directly towards the origin (Fig 6b).

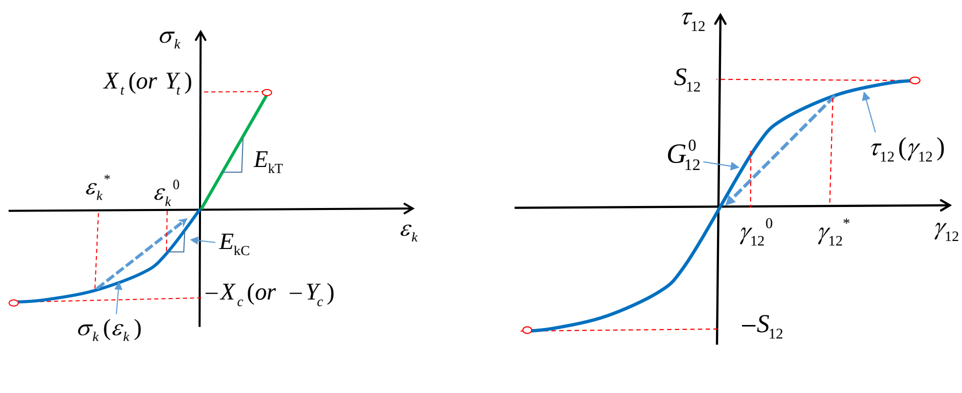

Figure 6 (a) asymmetric tension/compression stress-strain relation, and (2) shear nonlinearity.

5.3 Cohesive Laws for Fiber Rupture, Fiber Kinking, and Matrix Cracks

Similar to all other numerical techniques such as X-FEM and PNM-FEM that uses cohesive zone models to describe the progressive failure processes, in this study it is assumed that once an initiation criterion of a certain damage mode is satisfied, a cohesive crack with corresponding type is inserted. Further cohesive damage evolution until the crack becomes traction free is based on the normal and shear traction-separation laws and a mixed mode propagation criterion. As discussed earlier, it is very critical to consider tensile and compressive cohesive responses explicitly and simultaneously, and it is also very important to consider the possible coupling between the two modes. In this study, we propose the unified tension-compression cohesive laws for normal cohesive response and apply a commonly used shear cohesive law as shown in Figure 7. Triangular shaped cohesive laws were chosen for all modes for their simplicity.

The shear (mode II) response shown in Figure 7(a) is a standard one used widely in literature (e.g. [67, 69]). The response is anti-symmetrical with respect to positive and negative sense. The two governing cohesive parameters are the shear strength S_{12} and a mode II toughness Γ_{II}, from which the critical shear displacement can be obtained as $\delta_{Sc} = 2\Gamma_{II} / S_{12}$.

The fiber direction (or longitudinal) tensile and compressive cohesive responses are unified into a single cohesive law as shown in Figure 7(b) for tensile rupture and compressive kinking. The tensile response is governed by the longitudinal tensile strength X_t and a toughness Γ_{FT}, from which the critical displacement can be obtained as $\delta_{FTc} = 2\Gamma_{FT} / X_t$; while the compressive response is governed by the longitudinal compressive strength $-X_c$ and a toughness Γ_{FC} from which the critical compressive displacement can be obtained as $\delta_{FCc} = -2\Gamma_{FC} / X_c$.

Similarly, the cohesive model for matrix tension and compressive responses are unified into a single cohesive law as shown in Figure 7(c). The tensile response is governed by the transverse tensile strength Y_t and a toughness Γ_{MT}, from which the critical displacement can be obtained as $\delta_{MTc} = 2\Gamma_{MT} / Y_t$. The compressive response is governed by the transverse compressive strength $-Y_c$ and a toughness Γ_{MC} from which the critical compressive displacement can be obtained as $\delta_{MCc} = -2\Gamma_{MC} / Y_c$.

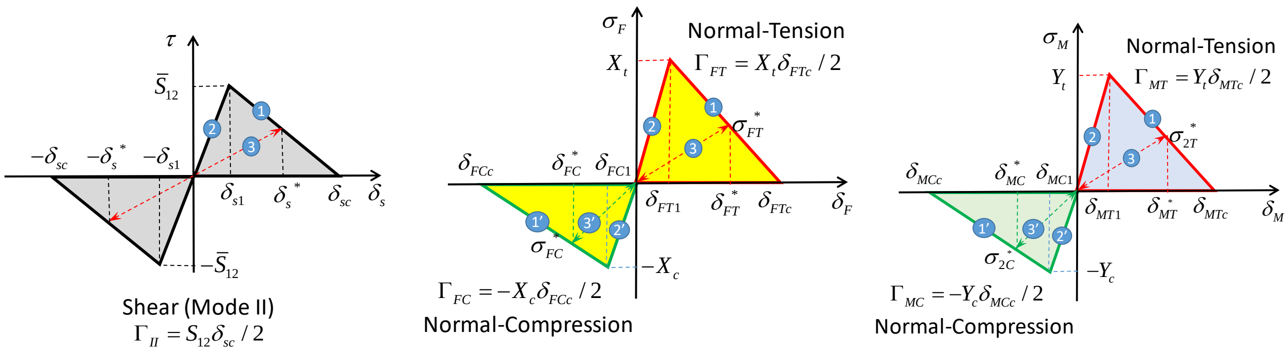

Figure 7 cohesive laws for (a) (matrix) shear damage mode; (b) fiber tensile rupture/compressive kinking damage mode; c) matrix tension/compression damage mode. Here the first subscript "F" denotes variables associated with fiber rupture or kinking damage, "M" refers to variables associated with matrix tension or compression damage. The second subscript "T" or "C" differentiate the tensile ("T") and compressive ("C") part of the cohesive laws.

We note that the negative normal displacements (δ_{MC}, δ_{FC}) in the compressive cohesive laws are not unphysical for typical composite failure under compression dominant conditions: the compressive kinking and compressive matrix crushing do induce finite amount of local negative normal displacements, if the associated damage bands are modelled with cohesive cracks with zero-thickness cohesive zones, as implemented in this and other studies. Numerically, such negative normal displacements lead to mesh interpenetration if they are modelled as explicit cohesive elements, causing numerical divergence (negative Jacobian). However, this is not an issue with our embedded cohesive zone model in the A-FEM.

It is noted that in Figure 7, all the cohesive laws are piece-wise linearized. Each of the segment with a constant slope is indexed with a number. This is done in accordance with the consistency-check based condensation algorithm discussed in section 3.3. Each segment is characterized by a critical stress ($\hat{\tau}^{(i)}$ or $\hat{\sigma}_{F/M}{}^{(j)}$), a corresponding local crack displacement ($\delta_s{}^{(i)}$ or $\delta_{F/M}{}^{(j)}$), and a constant stiffness ($\alpha_s{}^{(i)}$ or $\alpha_{F/M}{}^{(j)}$). Here the superscripts i (=1,2,3) and j (= 1, 2, 3; 1', 2', 3') are free indices for the cohesive segments with constant stiffness.

For each cohesive law in Figure 7, segment 3 and 6 are defined for irreversibility. The characteristic stresses and displacements, which are marked with superscript "*", are the maximum historical values ever experienced during the entire deformation history up to this point. Should unloading occur, it follows an instantaneous path with a constant stiffness of $\hat{\sigma}_{R/M}{}^{*} / \delta_{R/M}{}^{*}$. In this

study, these historical quantities are recorded for each damage modes and they play key roles in enabling partial damage coupling to be discussed shortly.

5.4 3D Geometric Models for Binary Model Analysis of Textile Composites

To handle large textile CMC structures, we have, follow the same augmentation process as in section 2, developed a breakable 1D tow element (Figure 8), which can be coupled with the 3D-A-FEM to simulate progressive damage and the failure of reinforcement tows. The 1D tow elements, which follow the spatial loci of each of the tow center lines, are embedded in a 3D effective medium, which is modelled by 3D A-FEM elements, a strategy that is based on the Binary Model (BM) formulation established in prior work [88-90]. Possible tensile tow rupture and compressive tow kinking are incorporated via a 1D cohesive law.

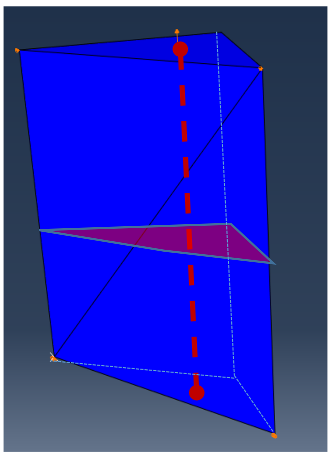

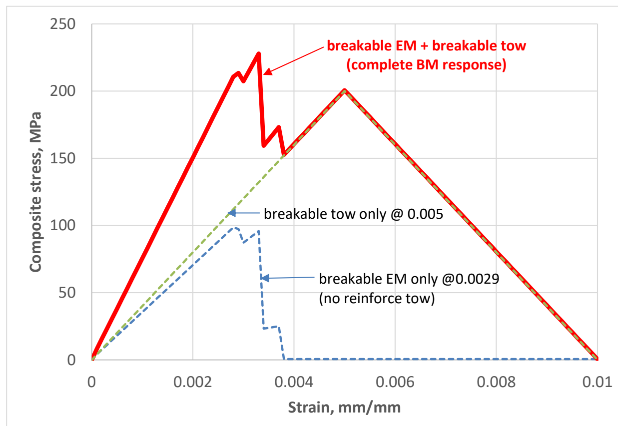

(a) (b)

Figure 8. (a) a simple BM model containing a prism EM and a straight tow (red dashed line). (b) The simulated elemental stress-strain response of the BM (red-solid line), which is a summation of the solid element responses (blue dashed line) and the tow response (green dashed line).

We have completed and improved the 3D A-FEM with shear nonlinearity to simulate realistic 3D textile composites under the BM scheme. The subcontractor of this project, Dr. Brian Cox has developed a very efficient algorithm for generating tow elements with realistic spatial distributions in textile composites [91]. The generator converts machine instructions for a 3D weaving loom into topological ordering rules, which are then converted into 3D spatial models of the tows in the textile. The input deck of the generator consists entirely of arrays of bounded integers, which are defined to correspond to weaving machine actions, thereby guaranteeing that any choice of the integers is in principle an achievable architecture on the machine. The fact that only bounded integers are used as input allows the generator to be linked easily with an optimization search engine, e.g., based on a genetic algorithm or an ant colony search algorithm Such an example is given in Figure 9.

By embedding such tow elements into the 3D effective medium modelled with our 3D A-FEs, very encouraging results can be obtained. One of such example will be detailed in next section.

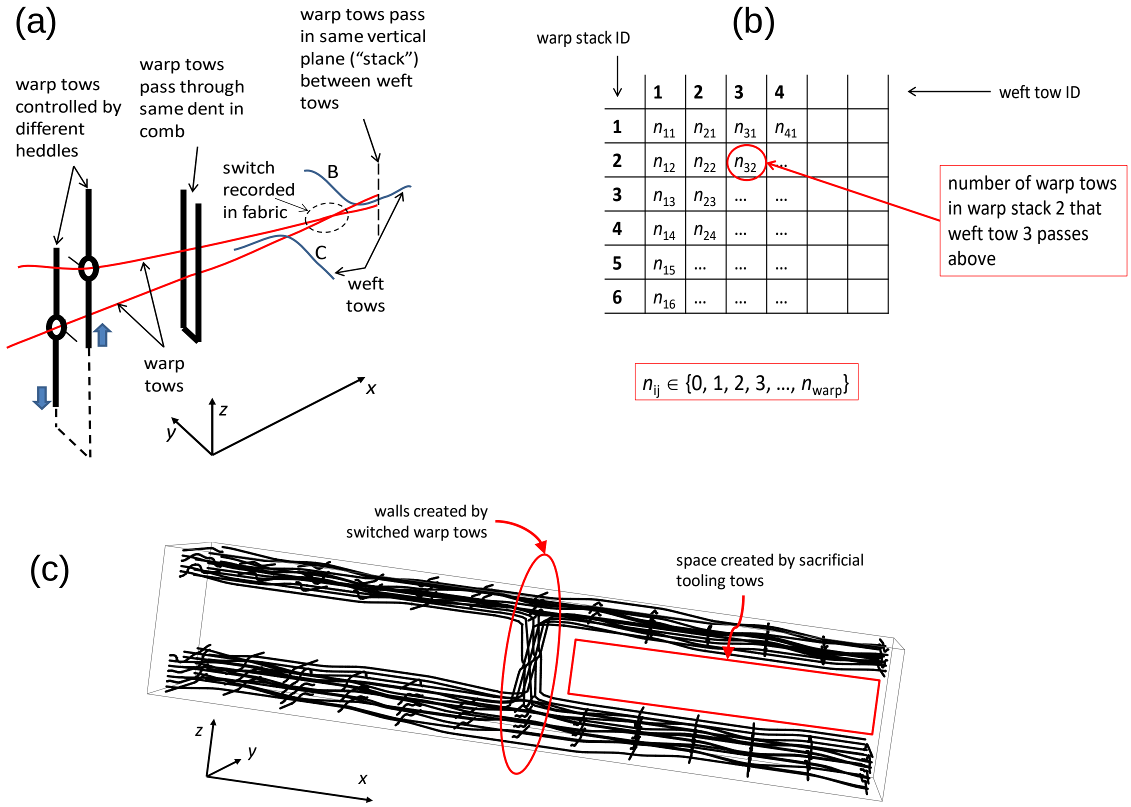

	1	2	3	4		
1	n_{11}	n_{21}	n_{31}	n_{41}		
2	n_{12}	n_{22}	n_{32}	…		
3	n_{13}	n_{23}	…	…		
4	n_{14}	n_{24}	…	…		
5	n_{15}	…	…	…		
6	n_{16}	…	…	…		

Figure 9. Illustration of the tow-mesh generator the geometric model generator. (a) Machine actions on a 3D weaving loom, which are represented as arrays of bounded integers (b), from which a complex 3D component is automatically generated (c). Nothing in the input deck tells the generator explicitly that it is making a sandwich structure.

6. NUMERICAL EXAMPLES AND DISCUSSIONS

6.1 Four-Point Shear Beam Test

In this section, we test the new A-FEM's capability in simulating the crack propagation in a 4-point shear beam test reported by [92]. The problem has been simulated successfully using extended finite element method (X-FEM) by Moes and Belytschko [66]. Here we adopt the numerical model setup used in [66], which is reproduced in Figure 10. The geometry dimensions are: b = 200 mm; $l = 4b$; $a = 0.2b$; $c/b = 0.4$; $l_1 = l_2$ = 20 mm; t = 100 mm.

Maximum principal stress criterion was used for crack initiation. That is, crack initiation from a pristine elastic element occurs when the maximum principal stress averaged within the element $(\bar{\sigma}_{\max})$, reaches the mode I cohesive strength $(\hat{\sigma})$. The crack path is perpendicular to the maximum principal stress direction. The concrete material properties are: $E = 28000$ N/mm^2;. $\nu = 0.1$; $\Gamma_{\mathrm{I}} = 0.145$ N/mm; $\hat{\sigma} = 2.4$ N/mm^2. The cohesive law used is triangular type with an initial slope of $\alpha_{n1} = 2.0\times10^4$ N/mm^3 and a softening slope of $\alpha_{n2} = -20$ N/mm^3.

As in [66], the maximum principal stress criterion was used for crack initiation. That is, crack initiation from a pristine elastic element occurs when the maximum principal stress averaged within the element $(\bar{\sigma}_{\max})$, reaches the mode I cohesive strength $(\hat{\sigma})$. The crack direction is perpendicular to the maximum principal stress direction.

To investigate the mesh sensitivity of the new A-FEM, the problem was analyzed by five different structured meshes with characteristic mesh size of h = 2, 4, 8, 13, and 20 mm (the total elements are 10760, 2849, 1094, 640, and 410, in the same order), and three unstructured meshes with h ~ 4, 8, and 15 mm (total elements 4062, 1333, and 463, respectively). The two finer meshes, h = 2 and 4 mm, are typical of those used in literature [51, 52, 66, 75], while the larger meshes (8, 13.3, and 20 mm) are used in this study to explore the mesh limit of the new A-FEM. The unstructured meshes of ~ 4, 8, and 13 mm were intended to check the mesh sensitivity and the robustness of the new A-FEM. Five of the discretized models (structured h = 2, 8, and 20 mm meshes and unstructured h ~ 8 and 13 mm meshes) under deformed states are shown in Figure 10 (b, c, d, e, f) with the crack trajectories roughly following the center lines of the white bands.

The loading parameters were set to be identical for all the cases, with a maximum prescribed displacement of 1.0 mm, a suggested initial incremental size of 0.001 mm, and a maximum incremental size of 0.01 mm. The actual size of each increment was determined by the automatic incrementation scheme in ABAQUS which depends on the convergence rate.

All simulations were run on a Dell precision M4600 (x64 bit) mobile workstation with Intel Core i7–2860 QM CPU @ 2.5 GHz and with 8 GB of RAM. Simulations were terminated when the load-point displacement reached 0.1 mm (after snap-back). RIKS option (arc-length method) was invoked in attempt to capture the snap-back behavior.

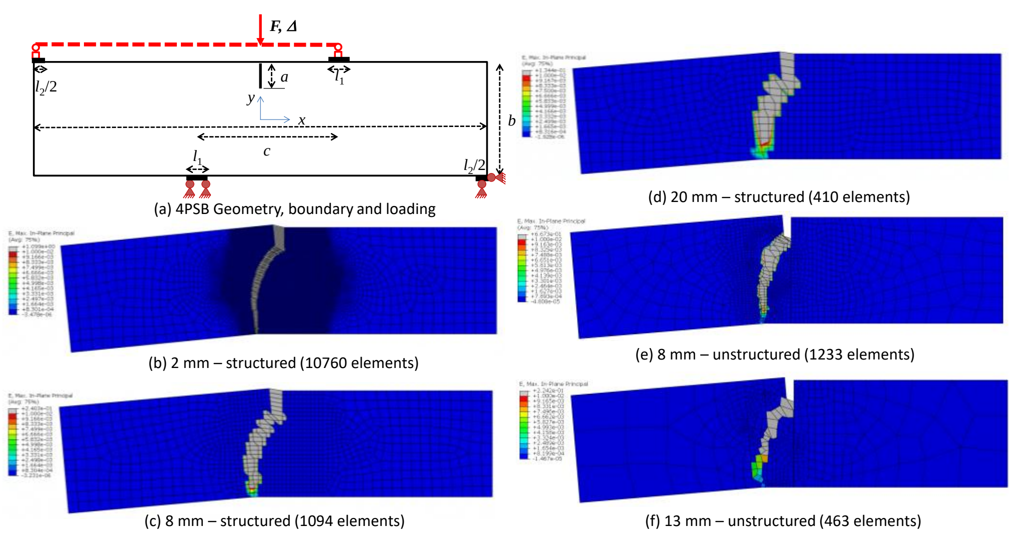

Figure 10 (a) Numerical models and simulated crack paths for structured 2mm (b), 8 mm mesh (c), and 20 mm mesh (d), and unstructured 8 mm (e) and 13 mm (f) meshes.

Numerical Accuracy and Mesh Sensitivity

The simulated load-displacement curves are plotted in Figure 11(a). The X-FEM prediction obtained by Moes and Belytschko [66], which used a triangular mesh of h ~ 3 mm, was superimposed on this plot for comparison. For each case, the load linearly increases with the applied displacement until crack initiation from the pre-crack tip, which occurs at an applied displacement of ~ 0.04 mm. After the initiation the load-displacement curve becomes increasingly nonlinear due to continuous crack growth. The peak load is reached at the displacement of about ~0.09 mm. After the peak load, all curves exhibit a strong snap-back behavior. In this study, the strong snap-back behavior was captured using the arc-length method available in ABAQUS (Option RIKS).

The A-FEM computed load-displacement results are very consistent with the X-FEM result obtained in [66]. In particular, the load-displacement curves obtained with smaller mesh sizes (i.e., h = 2 mm, 4 mm, and 8 mm) are almost identical with the X-FEM results. For the larger meshes, i.e., h = 13 mm and 20 mm, the curves deviate mildly from the finer mesh curves due to increases in initial stiffness. The systematic increase of initial stiffness with the increase of mesh sizes is largely due to the inherent numerical inaccuracy associated with the 4-node plane elements (it is well-known that larger FE elements lead to overestimate of elemental stiffness). If the deviation of initial slope is discounted, the load-displacement curves obtained with larger meshes (h = 13 and 20 mm) remain very consistent with the X-FEM curve and the finer mesh results. This clearly demonstrates the mesh insensitivity of the new A-FEM.

The mesh insensitivity of the new A-FEM is further demonstrated by the fact that the load-displacement curves obtained from unstructured meshes are also very consistent with the results of the structure meshes with similar mesh sizes. Two of the load-displacement curves obtained from the unstructured meshes, h = 4 and 8 mm, as shown in Fig. 11(a) by the dashed lines, are basically indistinguishable from the results of the respective structured meshes.

Figure 11(b) summarizes the crack trajectories predicted by the new A-FEM simulations with the structured (solid lines) and unstructured (dashed lines) meshes. The crack paths are all very consistent and close to the experimental curve, despite they were obtained with vastly different mesh sizes and structures. The mild difference in crack paths with larger meshes is largely attributed to the maximum kinking angle limit of +/-45^o permitted by our numerical program. This is a standard numerical treatment to avoid possible crack curve back. It is seen that even with this artificial limit, it takes no more than 2 to 3 sequential kinks for the trajectories to establish a path that is very close to the experimental curve.

It should be mentioned that the mesh insensitivity in this example is expected because all the mesh sizes are considerably smaller than the cohesive zone size (or fracture process zone size). The cohesive zone size, estimated by $l_{\mathrm{coh}} = E\Gamma_{\mathrm{I}} / 2\hat{\sigma}^2$ [23, 93] is about $l_{\mathrm{coh}} = 350\ \mathrm{mm}$. This is about twice the beam depth and more than 15 times the largest mesh size (20 mm). In this example, the mesh size is limited by the spacing between the notch and the nearest loading zone, which is merely 40 mm (Fig 10a). With the largest 20 mm mesh, there are only two columns of elements between the notch and the nearest loading zone. The fact that the new A-FEM simulation can still correctly capture the crack trajectory is rather encouraging. Elsewhere, it has been demonstrated through other examples that the new A-FEM remains fairly accurate with mesh sizes up to 70% of the cohesive zone size, in which cases the X-FEM exhibited serious (unacceptable) mesh dependency [57].

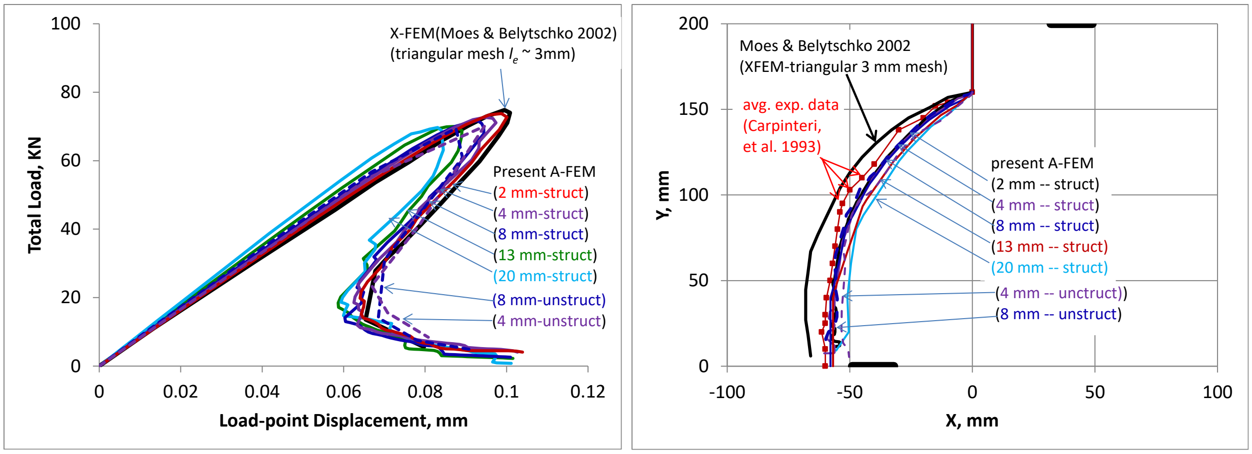

(a) (b)

Figure 11 A-FEM simulated (a) load-displacement curves and (b) crack trajectories the X-FEM results of [66]and experimental results of [92] .

Numerical Efficiency and Stability as Compared to PNM-FEM

In this section, we compare the numerical accuracy, efficiency, and stability of the new A-FEM against the phantom-node based FEM. The meshes and boundary conditions are exactly the same as those used in previous section. It is noted that both the new A-FEM and the PNM-based A-FEM have been implemented in the ABAQUS package (v6.11) as user-defined elements and they employ the same crack tracking algorithm [18, 21] (the tracking algorithm of the new A-FEM was directly inherited from the previous PNM-based A-FEM). Thus the numerical performance comparison should be objective.

For all simulations, the loading parameters were set to be identical with a maximum prescribed displacement of 0.1 mm, and a suggested maximum incremental size of 0.002 mm. The minimum increment size is 10^{-8} mm and largest suggested incremental size is 10^{-3} mm. RIKS option (arc-length method) was invoked in attempt to capture the snap-back behavior.

Comparisons of the predicted load-displacement curves using the new A-FEM and the PNM-based A-FEM are given in Figure 12(a). The X-FEM result reported in [66] is also included in this plot for comparison. Both the new A-FEM and the PNM-based A-FEM completed the simulations without much numerical difficulty. The new A-FEM results agree very well with the X-FEM result of Moes and Belytschko (2002). The PNM-based A-FEM also did a good job except that the snap-backs are slightly sharper than those predicted by the new A-FEM and by the X-FEM.

However the new A-FEM empowered by the consistency-check based condensation algorithm is much more efficient than the PNM-based A-FEM. Figure 12(b) compares the CPU time (in seconds) required by the two methods in completing the simulations. For an identical mesh the CPU time required by the new A-FEM is, on average, merely 1/50 of that required by the PNM-based A-FEM (i.e., an increase of numerical efficiency by 5,000%). The ~50 times increase of CPU time by the PNM-based A-FEM is NOT due to the use of double nodes (recall that the total DoFs of a PNM-based A-FEM model is two times the DoFs of the corresponding model of the new A-FEM). The two dashed lines in Figure 12(b) represent the CPU times required by both methods to complete the elastic problems with the same mesh and the same load incremental numbers, but with crack initiation and propagation prohibited. In such crack-free,

elastic simulations, the CPU time required by the PNM-based A-FEM is about 60% more than that required by the new A-FEM, which is consistent with what reported in [18]. Thus, for the PNM-based A-FEM, the ~100 time (10,000%) increase of CPU time from a crack-free elastic simulation to the respective crack propagation simulation is directly due to the additional computational cost in treating the propagating crack. The CPU times of the new A-FEM simulations are on average about twice that of the respective elastic calculations (~100% increase).

A close examination of the two methods shows that the significant increase of CPU time by the PNM-based A-FEM is associated with: 1) the ever increasing active DoFs as a crack propagates, and 2) the numerical procedure to judicially determine the crack configuration and to properly assign the ghost and real nodes to cracked subdomains. These two elements are critical to many advanced numerical methods that employ additional external DoFs to account for propagating cracks (e.g. X-FEM[2], PNM, and G-FEM). However, the new A-FEM does not need either of them (see [21] for the detailed A-FEM formulation). It is obvious that the consistency-check based algorithm of the new A-FEM contributes significantly to the improvement in numerical efficiency and accuracy.

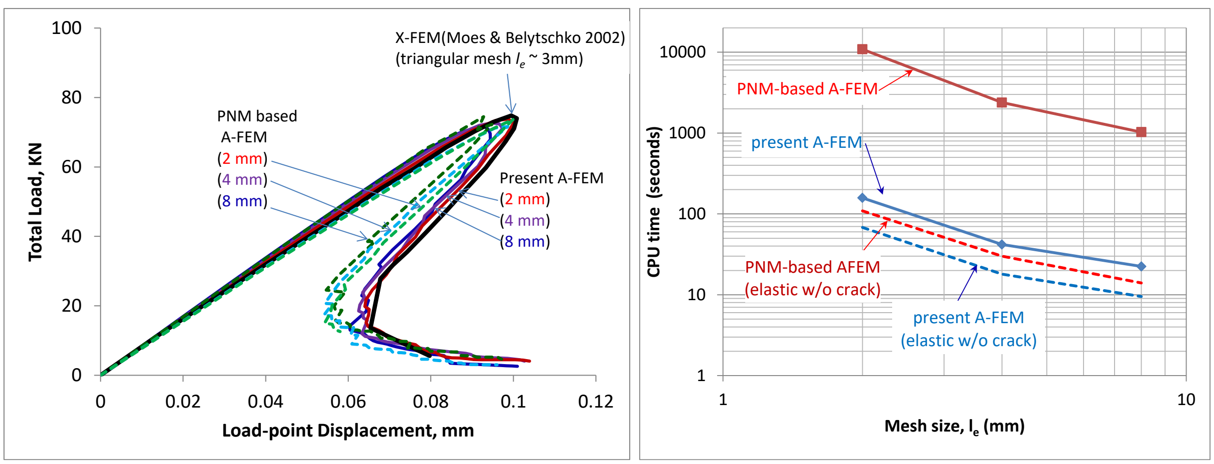

(a) (b)

Figure 12 (a) Comparison of predicted load-displacement curves using the PNM-based A-FEM and the new A-FEM. (b) Comparison of the CPU time as a function of mesh sizes.

6.2 Coupled Fiber-Matrix Interface Debonding and Kinking

We next demonstrate the capability of the new A-FEM in dealing with multiple crack interaction. We chose to model a single fiber/matrix domain as shown in Figure 13. The entire domain is 1 mm x 1 mm and the fiber diameter is 0.5 mm (i.e., fiber volume fraction 19.6%). Two sets of meshes were used to simulate the problem: a) a fine mesh as shown in Fig 13(a) with 2244 elements, and b) a coarse mesh as shown in Fig 13(b) with 110 elements. In the fine mesh (a) the elements are arranged to conform to the circular fiber/matrix interface. The ring of elements that host the bi-material interface are initially augmented with a weak discontinuity and are allowed

[2] We also compared the numerical efficiency with the X-FEM in ABAQUS (v6.11) and found that the present A-FEM is 2-3 orders of magnitude more efficient (see 94. Mohammadizadeh, S., *A novel Augmented Finite Element Method for Modeling Arbitrary Cracking in 2D Solids*, in *Dept of Mechanical and Aerospace Engineering* University of Miami, PhD thesis, 2013.).

for secondary crack kinking into the matrix subdomain if the subdomain stresses meet the maximum stress criterion. The coarse mesh (b) is a structured one and does not conform to the fiber/matrix interface (shown by the dashed circle in Fig 13(b)). That is, the fiber-matrix interface is deliberately set to bisect the structured elements. The elements traversed by the interface are initially augmented to account for intra-element material difference, possible interface debonding, and crack kinking into the matrix.

The modulus and Poisson's ratio for the fiber and matrix, respectively, are E_f = 40 GPa; ν_f = 0.33; and E_m = 4 GPa; ν_m = 0.4. A cohesive model with triangular traction-separation laws were used for interface debonding and matrix cracking. The cohesive parameters for matrix cracking and interface debonding are set to be identical: $\hat{\sigma} = \hat{\tau} = 50$ MPa; $\delta_{\mathrm{nc}} = \delta_{\mathrm{sc}} = 1\times10^{-2}$ mm; and $\delta_{\mathrm{n1}} = \delta_{\mathrm{s1}} = 1\times10^{-6}$ mm; Therefore, the fracture toughnesses for mode I and mode II are $\Gamma_{\mathrm{I}} = \Gamma_{\mathrm{II}} = 0.25$ N/mm. For the kinking crack initiation and propagation in the matrix, the maximum principal stress criterion is assumed.

Symmetric, displacement-controlled loading is imposed on both the left and right edges, while the top and bottom edges are stress free. For both cases, the prescribed maximum nominal strain is 2% and the maximum nominal strain increment is 0.05%. Under this loading scheme, the CPU time needed to complete the simulations is: 140 seconds (58 increments) for the fine-conforming mesh, and 20 seconds (58 increments) for the coarse-nonconforming mesh.

The maximum strain distributions at four loading stages for the two cases are shown in Figure 13 (a) and (b). The predicted curves of nominal stress versus nominal strain are shown in Figure 13(c). In both cases, the nominal stress-strain curves can be roughly categorized into three stages. The first stage is the elastic stage ($\varepsilon_1 < 0.5\%$), wherein the interface remains well bonded and the response is linear, which can be seen from Fig 13(a1) and (b1)[3]. At a nominal strain of 0.5%, debonding cracks start to initiate at (R, 0) and (-R, 0), and they propagates both upwards and downwards along the interface. These interface cracks propagates in a symmetric fashion regarding to both horizontal and vertical directions (Fig 13 a2 & b2). As the debonding length increases, the composite stiffness is gradually reduced, but the stress continues to rise due to further stretching in matrix. This stage is eventually followed by a kinking initiation. For the fine mesh, kinking occurs at a nominal strain of ~0.84% and for the coarse mesh, it happens at a strain of 1.2% (Figure 13 a3 & b3). Shortly after the kinking initiation, the kinking cracks propagate quickly towards the top and bottom specimen boundaries, completely separating the entire domain (Figure 13 a4 & b4). This process is characterized by a sudden drop of load in the load-displacement curves.

[3] The apparent strange strain distributions in Fig 11(b) are due to ABAQUS graphics output. Since ABAQUS does not support graphic depicting of UELs, we had to superimpose a layer of ABAQUS CPS4 elements with near zero stiffness to display the strain distribution. In this way, any displacements are interpolated continuously within an element.

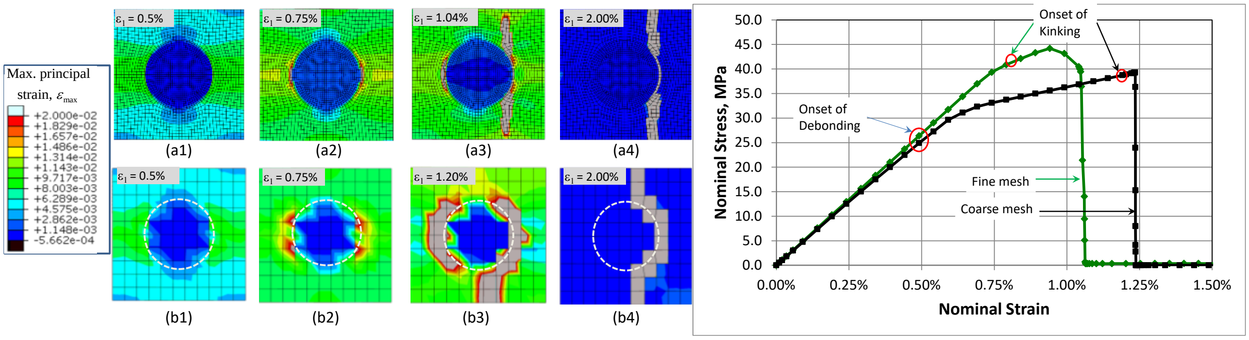

(a) (b)

Figure 13 (a) Crack development, including the initial fiber-matrix interface (dashed line), debonding crack, and final kinking cracks in matrix, are indicated in the top and bottom contour plots for the two meshes. (b)The new A-FEM simulated nominal stress versus displacement for a single fiber/matrix domain under uniaxial tension.

It is seen that, despite the vast difference in mesh size and interface conformity, the predicted stress-strain curves remain very similar to each other. The differences in predicted composite elastic modulus and energy dissipation are well within 5% (The predicted modulus values, 5.2 GPa for mesh (a) or 5.37 GPa for mesh (b), are moderately greater than the lower-bound estimation of 4.86 GPa based on the rule-of-mixture, which is a quick proof that the current predictions are reasonable). Finally, the 10% and 14% difference in predicted composite strengths and ultimate strains, respectively, by the two meshes are at least acceptable given the large difference in mesh size and interface conformity.

It is emphasized here that in the above simulations, the tightly coupled cracking development processes, especially the formation of the kinking crack from the active interface debonding crack tip zone, is purely determined by the program from the computed local stresses in the matrix subdomain according to the prescribed maximum principal stress criterion (for initiation). While this complex, coupled fracture processes can be captured with relative easily by the present A-FEM with subdomain (secondary) cracking capability, few other existing methods can truly handle this with explicit consideration of the interactive stresses at the two active fracture process zones.

6.3 Simulations of Complex Damage Evolution in a 3D textile composite

In this example, the 3D A-FEM is used to simulate the multiple crack initiation in a C/SiC angle interlock weave shown in Fig. 14(a), which is a 3D reconstruction from a high-resolution μCT measurement reported in [95]. A virtual specimen was generated with stochastic tow geometry using Monte Carlo methods in which the geometrical model resulting from application of the Markov chain algorithm was converted into a mesh of solid computational elements suited to the A-FEM formulation as shown in Figure 14(b) [10, 96]. The calibrated tow elasticity is numerically similar to the elasticity deduced for a similar carbon/SiC material, reported in [97]. Nonlinear fracture laws were calibrated from the same tests by matching the predicted matrix cracking stress with the experiment.

The matrix containing the crack is present in this image, but the matrix elsewhere has been stripped away in rendering the image to reveal the underlying tow architecture. All such warp tow segments are indicated by the vertical dashed lines in Fig 14(c); they correlate consistently with

crack arrest. (The right image in Fig 14(c) actually refers to a material in which the weft tow spacing was larger than in the left and center images, but is otherwise of identical architecture; it has been re-scaled to facilitate comparisons. Importantly, the relation of crack position to weft tow position is the same in all three images.)

Key features of the crack pattern, including the approximate periodicity of the microcracks, which form above near-surface weft tows, and the alignment of microcracks in diagonal bands (one of which is outlined by the ellipse in Fig 14c), are well replicated by the virtual tests. The locations of the cracks relative to underlying weft tows are also well predicted by the 3D A-FEM simulation. One particular characteristic of the microcracking demonstrates the potential of the A-FEM for virtual tests because of its capability in predicting details. The microcracks seen in experiments form above weft tows and propagate both into the composite and across the surface of the composite, tracking the weft tow. However, the propagation across the surface is limited: when the microcrack approaches the region where the weft tow dips beneath a warp tow, propagation is arrested. Thus the microcracks remain of finite length (Fig. 14c). This behavior is replicated well by the 3D A-FEM simulations. The images of Figs. 14(c, d) focus on a single microcrack in the matrix layer. The microcrack can be seen to have followed a weft tow and then arrested as it approached the location where the weft tow is submerged under a warp tow.

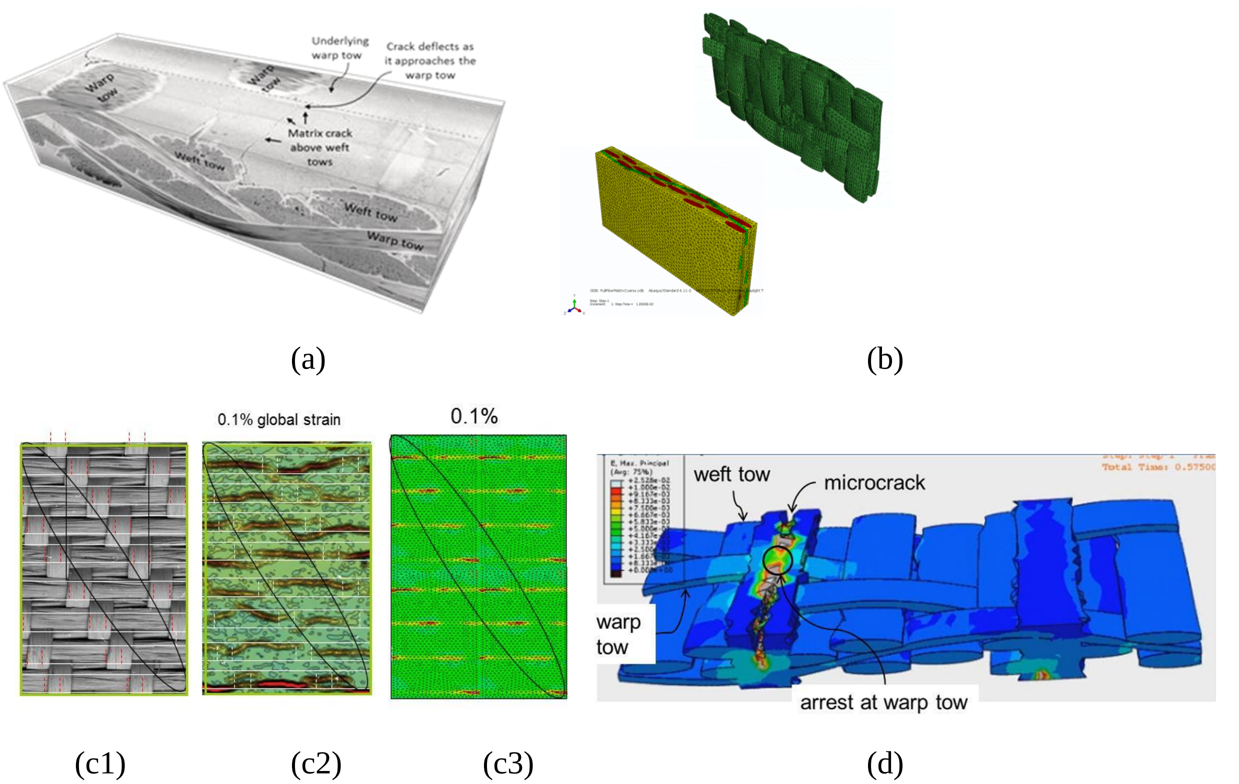

Figure 14. (a) 3D visualization of μCT data provides further detail of the observation in (a) that matrix cracks that have formed above a weft tow segment arrest when they approach the region where a warp tow that crosses over the weft tow. (b) virtual specimen generated from the μCT data with top graph shows the two architecture and the bottom graph shows the mesh for the entire model. (c1) textile preform coated with thin layer of matrix (C/SiC angle interlock). (c2) observations of microcracks by digital image correlation in composite formed by full infiltration of SiC matrix into preform in (a). (c3) predicted crack pattern. (d) Detailed rendering of a

simulation shows one microcrack above a weft tow correctly predicted to arrest upon approaching the underlying warp tow.

The phenomenon of crack arrest is correlated with lowering of stress in the superficial matrix by straightening of the warp tow. (Earlier evidence for tow straightening in this class of composites was reported in [98].) Both this stress heterogeneity and the critical stress for microcracking depend on geometrical details such as the thickness of the superficial matrix layer and the orientations of tows. They will therefore be affected by stochastic variance in the tow architecture. By simulating the evolution of discrete crack systems with high fidelity, the virtual tests can directly relate variance in microstructure to variance in failure due to microcracking (a potentially fatal event in hot structures).

6.4 Progressive Failure Prediction of Composite Laminates

6.4.1 Unidirectional Open-Hole Tension (OHT) and Compression (OHC) Specimens

In this case study the progressive damage evolution in the unidirectional open hole tension specimen reported in Prabhakar and Waas (2013) [99] were simulated. The UD composite is a proprietary material similar to IM7/8552. Here the properties reported in [99] are summarized in Table 1, supplemented with other parameters from various data sources from literature. Specimens with fiber orientation of 90^0, 45^0 and 0^0 were simulated with both tension and compression load. Whenever available, the A-FEM results were compared with either experimental or simulated results in literature.

Table 1. Composite properties of the OHT and OHC specimens

IM7/8552 Elastic Constants	$E_{1T} = E_{1C}$ (GPa)	$E_{2T} = E_{2C}$ (GPa)	ν_{12} --	ν_{23} --	G_{12}^0 (GPa)
	136	6.7	0.33	0.016	3.2
Strength (MPa)	X_t	X_c	Y_t	Y_c	S_{12}
	2960	1680	60	288	90
Toughness (N/mm)	Γ_{FT}	Γ_{FC}	Γ_{MT}	Γ_{MC}	Γ_{II}
	14.8	25.2	0.67	2.47	1.67

<u>90° Tension and Compression</u>

The 90^0 OH specimen as shown in Figure 15(a) is 50.8 mm along the loading direction and 38.1 mm wide. The thickness is 0.635 mm and the center hole diameter is 6.35 mm. To check the mesh sensitivity of the current method, the specimen was discretized into two sets of unbiased, unstructured meshes, one with 1298 elements and the other with 2093 elements.

The A-FEM simulations indicated that for this case, crack initiation occurred at the maximum stress concentration sites, i.e., the top-center and bottom-center of the hole edge. Once initiated,

both cracks propagated rapidly towards the specimen edge leading to a complete two-part separation. The simulated tensile reaction force vs. applied displacement curves using the two meshes are very consistent and they are very close to the CDFE results reported in [99]. Note though, the CDFE results were obtained with biased meshes, i.e., assigning much refined elements in regions where the crack initiation and extension are anticipated. The predicted peak load corresponds to a OHT strength of 25 MPa, much smaller than the un-notched transverse tensile strength of Y_t = 60 MPa (a maximum stress concentration factor of 2.4 along the hole edge).

Under compression (Fig. 15b), the A-FEM predicted that two compressive cracks would be initiated at the same locations of the tension cracks, but at a much larger (compressive) load, due to a much larger compressive transverse strength of Y_c = 288 MPa. The predicted OHC strength, deduced from the compressive load-displacement curves in Figure 15(b), is 130 MPa.

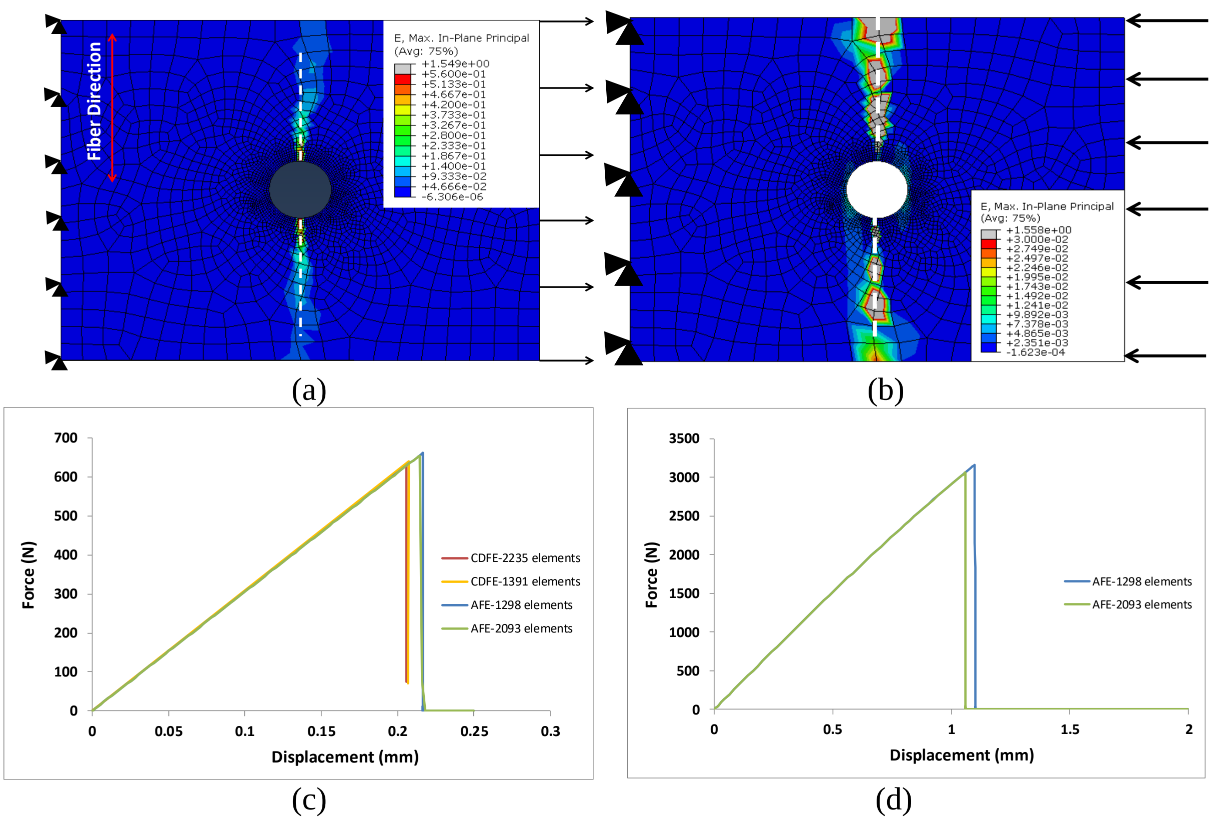

Figure 15 (a) OHT specimen and loading; (b) OHC specimen and loading; (c) A-EFM predicted OHT-90^0 load-displacement curves as compared to the CDFE results; (d) A-FEM predicted OHC-90^0 load-displacement curves.

45^o Tension and Compression

The OH-45^0 specimen as shown in Figure 16(a) and (b) is 75.2 mm along the loading direction and 38.1 mm wide. The thickness is 0.635 mm and the center hole diameter is 6.35 mm. The specimen was discretized into two sets of unbiased, unstructured meshes, one with 2441 elements and the other with 4299 elements.

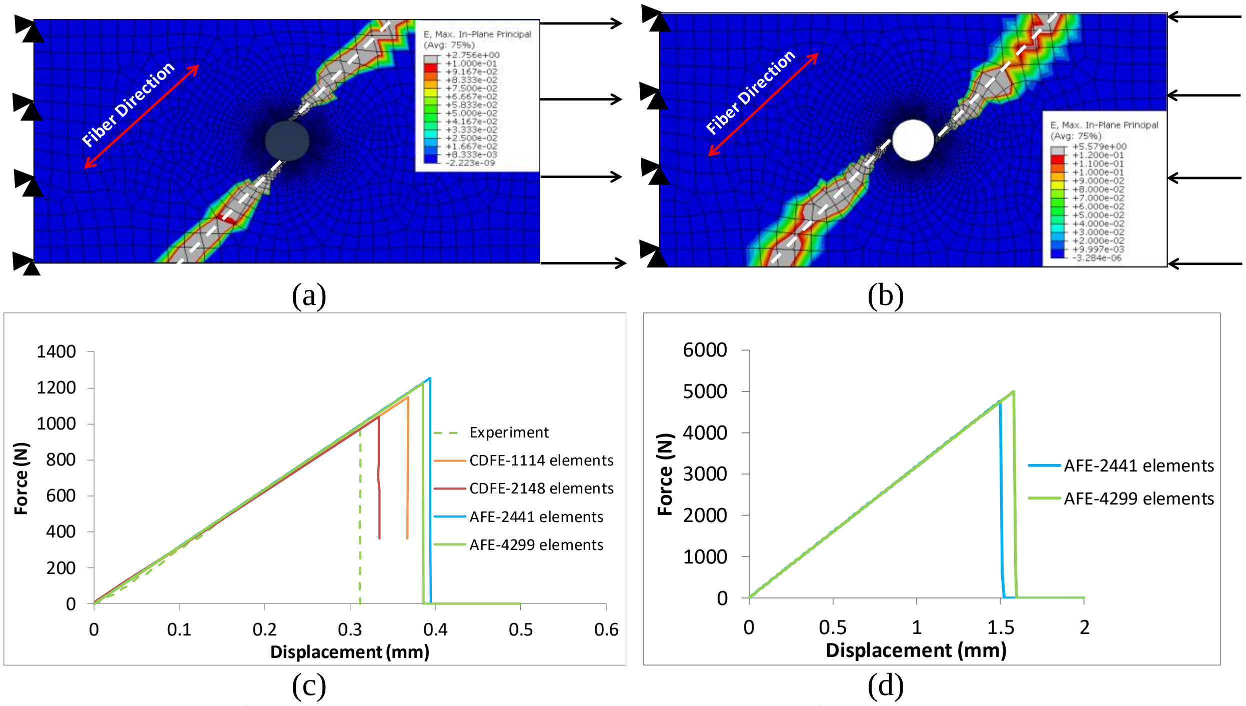

Figure 16 (a) OHT-45^0 specimen and loading (2441 ele mesh); (b) OHC-45^0 specimen and loading (2441 ele mesh); (c) A-EFM predicted OHT-45^0 load-displacement curves as compared to the CDFE results; (d) A-FEM predicted OHC-45^0 load-displacement curves.

The A-FEM predicts that under tension, the OHT-45^0 was failed by initiation of two cracks near the top-center and bottom-center of the hole edge respectively, which rapidly propagated along fiber direction (i.e. 45^0) all through the specimen width (Fig 16a). With the help of inertia-based stabilizing method, this strongly unstable crack initiation and propagation until two-part separation was simulated without any numerical difficulty. The simulated load-displacement curves for the two meshes are almost identical to each other and they are sufficiently close to the experimental and CDFE results reported in [99] (Fig 16c) Furthermore, the predicted crack paths are very consistent with the experimental observation and the predicted OHT-45^0 strength of 45 MPa is very close to the experimental value of 42 MPa [99].

For the OHC-45^0 test, the A-FEM predicts a similar sudden failure process. However, the two cracks are initiated at different locations, instead of top-center and bottom-center, the two cracks were initiated at the left-middle and right-middle of the hole edge (Fig 16b) (These crack initiation locations were verified by independent stress analyses using ABAQUS CPS4 element according to Sun's criterion). The simulated load-displacement curves for the two meshes are consistent with each other. The ultimate (compressive) load of 4700 N is much higher than the tensile failure load (1200 N) due to the larger Y_c value. The predicted OHC-45^0 strength is 196 MPa.

0^o Tension and Compression

The OH-0^0 specimen as shown in Figure 17 is 101.6 mm along the loading direction and 38.1 mm wide. The thickness is 0.635 mm and the center hole diameter is 6.35 mm. The specimen was discretized into three sets of unbiased, unstructured meshes with 6706 elements, 12891 elements,

and 26290 elements, respectively. The characteristic element sizes are 1.0 mm, 0.5 mm, and 0.25 mm, in the same order.

In this particular case, since the experimentally measured load-displacement curve as reported in [99] is plagued by early grip slipping (which caused premature cracking at a much reduced peak load). We seek alternative validation from a cohesive zone model as shown in Figure 17(b). In this model, the two experimentally observed crack paths were explicitly modelled with cohesive elements; while the other domains are discretized into standard CPS4 elements available in ABAQUS (V6.14).

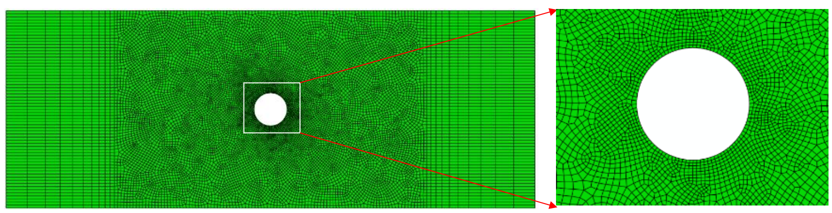

(a) AFEM 12981 element model

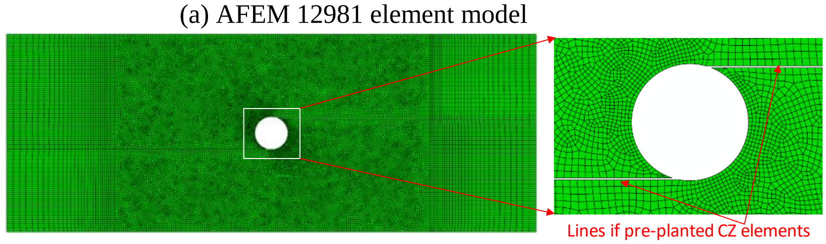

(b) CPS4 + CZM 24009 element model

Figure 17 OH specimen geometry and loading. (a) A-FEM mesh without initially designated cracks (12981 elements), and (b) CZM mesh (24009 elements) with two designated crack paths in accordance with experimental observation of [99].

The simulated load-displacement curves for the three different A-FEM meshes and the CZM model are summarized in Figure 18(a). In all cases, the curves are pretty linear up to a load level of 11000 N. Beyond this point, all curves exhibit some degree of deviation from linearity, which can be seem more clearly from the magnified view in Figure 18(b). Although the overall load-displacement responses from the four different models are fairly consistent to each other, each curve exhibits somewhat different local kinks (i.e. sudden load drops) at different loading stages.

Each of these mild load-drops corresponds to the stick-slip behavior of crack propagation, which are very sensitive to mesh size and local mesh structure along the crack path. As an example, the crack initiation and propagation in the 12891-element A-FE model and the 24009 CZM model were compared in Figure 19. Figure 19 (a1) shows the contour plot of ε_{max} when the load-point displacement is $\Delta = 0.355$ mm, just before any significant crack extension and corresponding to point ① in Figure 19(b). The magnitude and distribution of ε_{max} in CZM model and AFEM model are nearly identical. Note that at this point in the A-FEM model, four small cohesive cracks, one for each quadrant roughly at an angle of 15^0 with respect to the vertical center line, have already

been initiated but have not become traction-free cracks yet. The predicted initiation locations of these cracks are consistent with experimental observations of [99], as well as with a detailed μCT characterization of similar specimens under similar loading conditions [86].

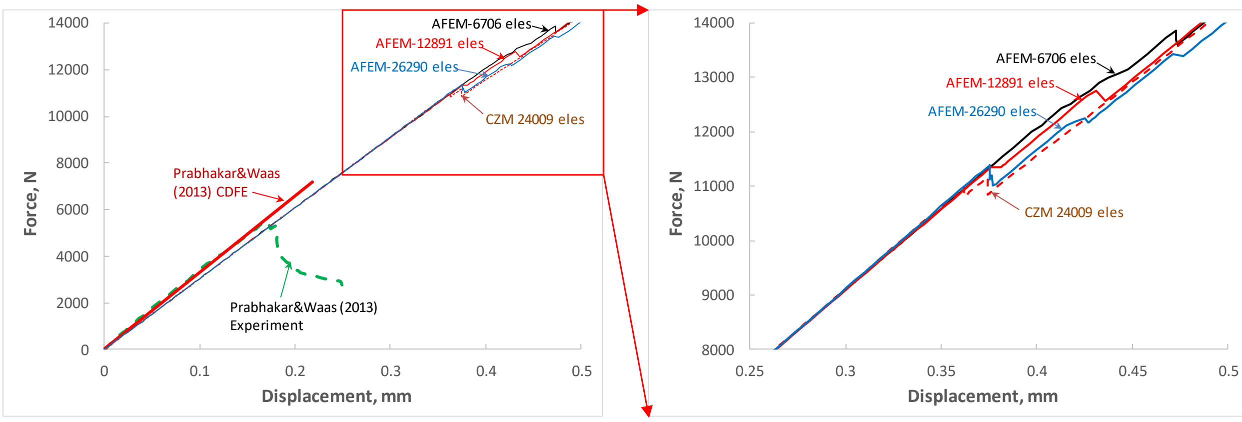

Figure 18 Load-displacement relation predicted using A-FEM as compared with data from CZM analysis and experiments.

Shortly after this point, at Δ = 0.365 mm (point ② in Figure 19b), one of the cracks in the CZM model suddenly propagated and arrested at a distance of about 25 mm to the left of the open hole, as indicated in the left contour plot of Figure 19(a2). This resulted the first load drop in the CZM load-displacement curve in Figure 19(b). At this point in the A-FEM model (right plot of Figure 19(a2)), the four small cracks extended by a small amount (~ 1.0 mm), which caused a small reduction of stiffness in the A-FEM load-displacement curve but no visible load-drop.

Upon further displacement increase to Δ = 0.385 mm (point ③ in Figure 19b), the upper right crack in the CZM model extended suddenly to about 25 mm and the left bottom crack also extended by a further amount of 5 mm, as indicated in the left contour plot of Figure 19(a3). This resulted a second load-drop in the CZM load-displacement curve (Fig 19b). Between point ② and ③ in the A-FEM model, two of the four initiated cracks, the upper right one and the bottom left one, extended almost simultaneously (at Δ = 0.380 mm) by an amount of 25 mm, which resulted a significant load-drop in the A-FEM load-displacement curve. The other two initiated cracks stopped further development from this point on.

As the load-point displacement further increased to Δ = 0.475 mm (point ④ in Figure 19(b)), the two cracks in the CZM model propagated steadily towards to the loading edge. However, in the A-FEM model, each of the two cracks propagated in a stick=slip fashion, causing several kinks in the A-FEM load-displacement curve as seen between point ③ and ④ in Figure 19(b).

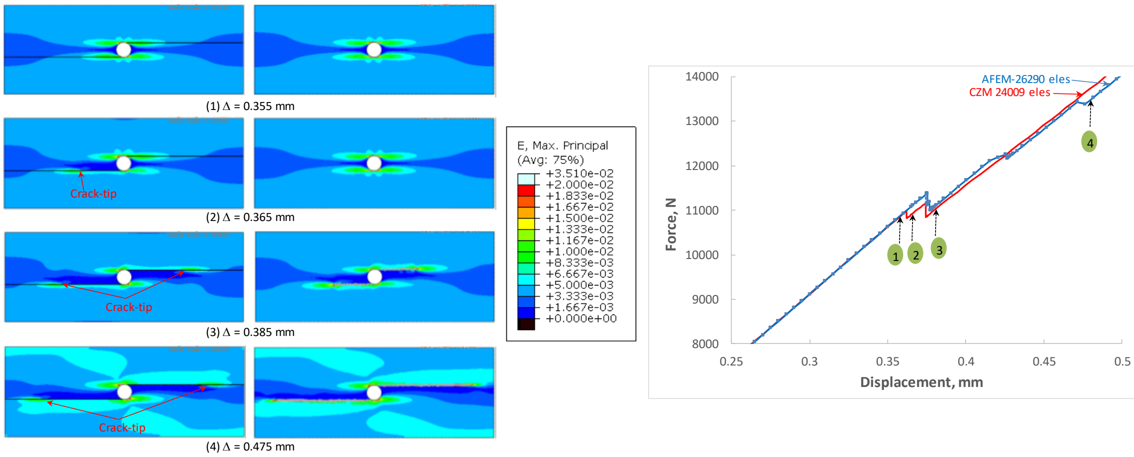

Figure 19 (a) comparison of crack development in the 24009-element CZM model (left) and in the 12891-element A-FEM model(right) at four different displacement increment; (b) the respective 4 instances at the simulated load-displacement curves.

When subjected to longitudinal compression, the crack development is much different due to the change of stress state surrounding the hole. In particular, the tensile hoop stresses at the left-center and right-center of the hole edge, coupled with the low Y_t strength values (60 MPa), lead to the development of two tensile dominant cracks much earlier than the shear dominant splitting cracks (Figure 20a). The tensile cracks partially alleviate the stress concentration around the hole hence the development of the shear dominant splitting cracks are much delayed.

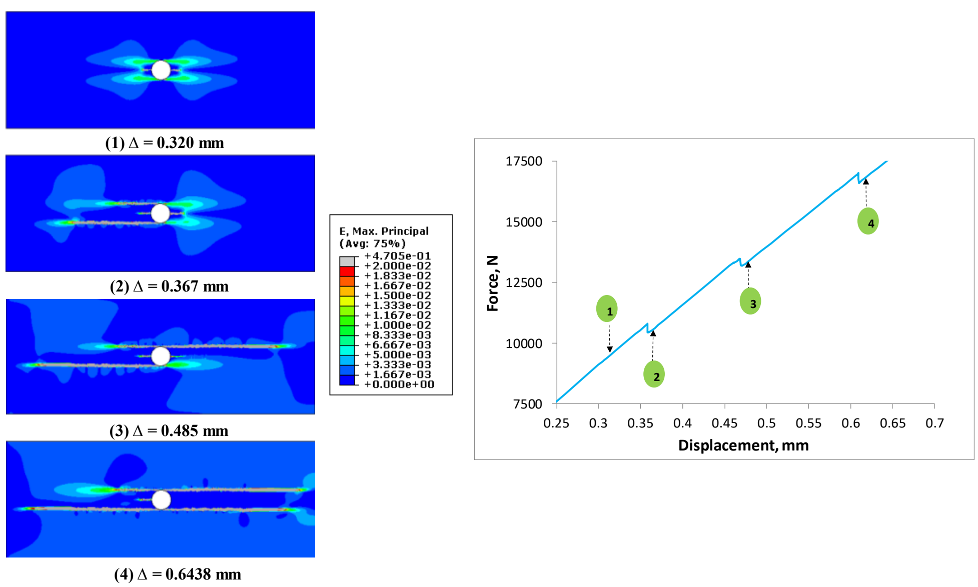

Figure 20 Strain contour plots of a 0°-OHC lamina under four load levels (26290 element mesh) illustrating the multiple crack initiation and propagation in this specimen. (a) two tensile crack initiation at applied displacement of Δ = 0.32 mm, (b) appreciable propagation of two additional corner cracks at Δ = 0.358 mm, (c) much extended two corner cracks suppressing the propagation of the first two tensile cracks at Δ = 0.367 mm, and (d) final stage of simulation at Δ = 0.821 mm.

6.4.2 Quasi-isotropic Open-Hole Tension (OHT) and Compression (OHC) Specimens

In this case study, we apply the nonlinear orthotropic A-FEM to analyze the progressive damage evolution in multi-directional laminated composites, which typically exhibit arbitrary multiple cracking events co-evolving from earlier loading stage up to final, catastrophic failure [21]. Explicitly damage accumulation descriptions of various damage modes typically observed in composites, including matrix cracking, fiber rupture in tension/kinking in compression, and delamination are all included as described in section 5.

The quasi-isotropic open hole specimen with a layup of $(45/90/\text{-}45/0)_s$ as illustrated in Figure 21 is of dimension 150 mm x 38 mm x 1.0 mm and the center hole diameter is 6.35 mm. Each ply is modeled with 6707 A-FE elements and all the interlaminar interfaces are modeled with 3D cohesive zone elements developed previously in the PI's group.

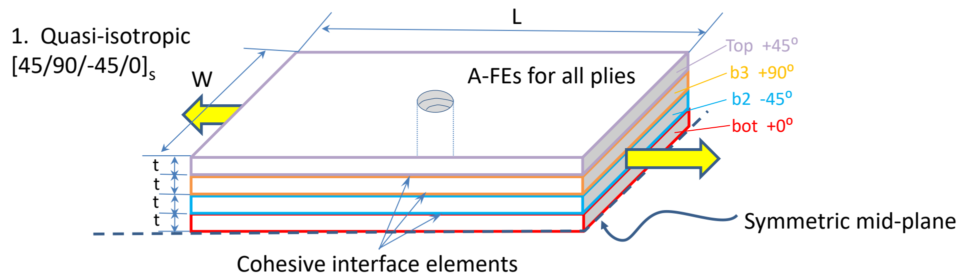

Figure 21 Quasi-isotropic open hole specimen with L = 150 mm and W = 38 mm.

The crack initiation is based on Hashin's criterion. Upon cohesive crack initiation in an element, the element is augmented automatically and a cohesive damage accumulation law according to the crack type is introduced to account for the post-crack fatigue life. For the material studied in this paper (IM7/8552), the cohesive damage accumulation laws for all the crack types have been previously calibrated and reported by [100, 101].

Figure 22 gives a validated example of the A-FEM prediction to an open-hole tension-tension specimen reported in [102]. The specimen is exposed to a cyclic loaded with a maximum load level of 50% of the failure load and a load ratio 0.1 for 30,000 cycles, followed by a monotonic load until complete failure. Figure 22(a) shows the strain contours in the plies as well as the fatigue cracks generated automatically by the A-FEM. The A-FEM predicted cracks and crack types are consistent with experimental observation. The predicted residual strength of 515 MPa is very close to the experimentally reported mean value of 544 MPa. The deamination at the interfaces as shown in these figures is also consistent with experimental observations [102]. This and other validated examples indicate that the A-FEM based fatigue analysis tool can meet the challenge of predicting fatigue life of composites with explicit consideration of multiple discrete damage events.

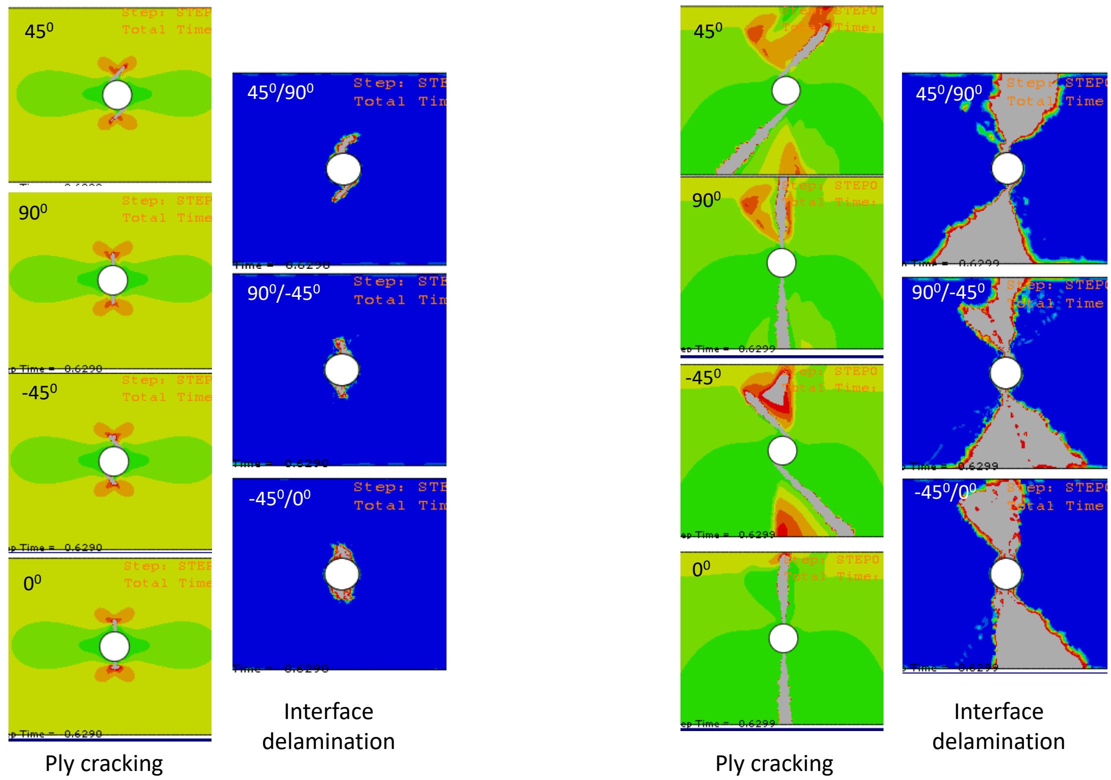

Figure 22 (a) A-FEM predicted individual cracking in each ply (white bands) and delamination at the three interfaces (white/red areas) at the peak load; (b) much extended ply cracking and delamination immediately after peak load

6.5 Coupled BM-AFEM for Large Textile Composites

In this section, we demonstrate the useful application of the developed breakable 1D tow elements (section 5.4) in modeling the progressive damage in large textile composites. Shown in Figure 23(a) is an integrally woven CMC panel of dimension of 51 mm x 51 mm x 2.4 mm. The panel consists of 103 weft tows and 99 warp tows, part of which can be seen from the magnified view. The material properties of this panel has been calibrated from a leveraging AFRL program and will not be repeated here.

The fiber tow grid and elements are generated using the geometric model generators as described in section 5.4. The panel is discretized into 8 layers of 3D solid elements (8 x 10,000 = 80,000) which are connected by 7 layers of 3D CZM interface elements (7 x 10,000 = 70,000). In addition, 50,000 tow elements are embedded in the 3D model with some tow elements passing through the various interfaces.

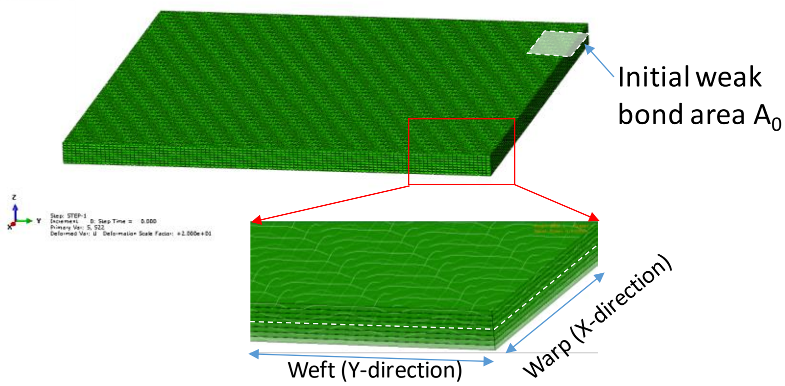

(a)

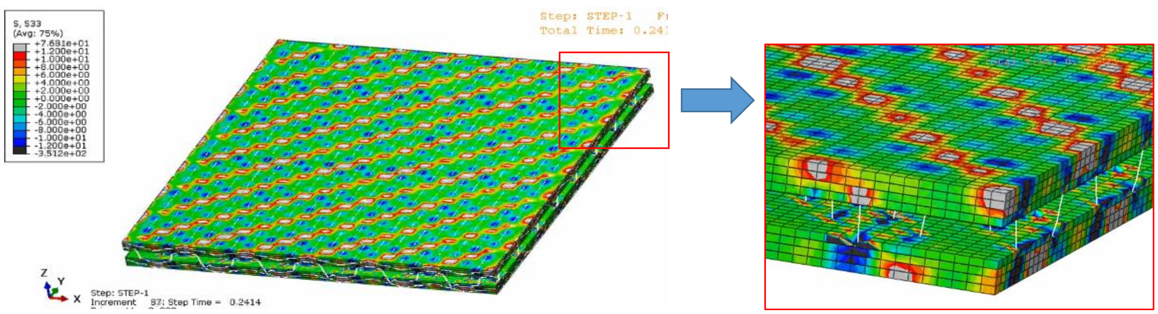

(b)

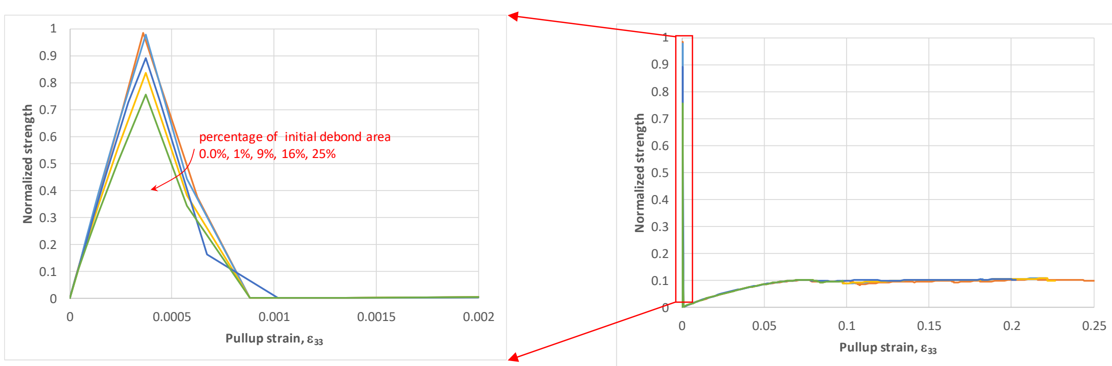

(c)

Figure 23 (a) BM-AFEM model for the integrally woven CMC panel with embedded tow elements showing by the magnified view; (b) BM-AFEM simulated surface stress distribution very consistent with experimental measurement. The magnified view of the upper-right corner show the cracked interface bridged by tows. (c) BM-AFEM simulated stress (normalized) vs. strain curves with initial flaws of various sizes.

Initial flaws of size 1%, 9%, 16%, and 25% with respect to the entire area (51 mm x 51 mm) is introduced into the center interface to investigate the effects of such flaws on the structural integrity, especially the through-the-thickness strength. To mimic the test, the bottom surface is fixed and the entire top surface is under a displacement controlled loading.

The BM-AFEM simulated deformation and surface stress distributions are shown in Figure 23(b). The pseudo periodic stress distribution with oscillating tensile and compressive stress, despite the overall tensile loading, is very typical of textile composites [97, 103]. It is mainly caused by the reinforcing tow architecture. The magnified view clearly shows the tow bridging across the debonded interface, which improves the damage tolerance of the relatively brittle CMCs.

The predicted stress-strain curves (normalized) are summarized in Figure 23(c). All stress-strain curves exhibit an initial spike followed by a prolonged plateau with about 10% of the peak strength. The initial spike with strain less than 0.01% is due to the very brittle nature of the matrix (with critical energy release rate on the order of 1-10 J/m^2): the interface debonding occurs at very small strain levels (< 0.01%). However, the fiber tows are able to bridge the debonded interface and provide further damage tolerance. It also shows that, for this particular loading condition, effective bridging is not fully realized until the nominal strain reaches about 3-5%. Other simulations show that fiber bridging is much more effective when the fracture process is shear dominant.

It is rather encouraging that, although the fiber tows are modelled as the simplest possible 1D elements (which are embedded in the 3D domain with multiple-point-constraint), the simulation results are nevertheless very consistent with physical reality.

7. CONCLUDING REMARKS

In this study, a new augmented finite element method (A-FEM) has been formulated based on the principle of virtual work. One of the major advantages of this method is that it can accurately account for arbitrary intra-element cracks and their interaction without the need for additional external DoFs as in X-FEM or extra nodes as in PNM. The new A-FEM formulation does not need to assume deformation modes for elemental displacement enrichment as in the embedded discontinuity method either. Instead, it introduces internal node-pairs with normal displacements as internal nodal DoFs, which are eventually condensed at elemental level. Thus the crack displacements are natural outcomes of the elemental equilibrium consideration. The advantage is multi-fold. First, it enables a unified treatment of both weak and strong discontinuities. Second, for strong discontinuities with piece-wise linear constitutive relations, the new A-FEM formulation ensures an exact solution (in the piece-wise linear limit) to the condensed elemental equilibrium, which greatly improves the numerical accuracy, stability, and efficiency by 2-3 orders of magnitude. Third, the unique A-FEM formulation makes it straightforward to repeat the augmentation procedure within an element to include multiple intra-element cracks, which is very powerful in dealing with multiple crack interaction problems because such augmented elements do not need extra external DoFs or nodes.

The elemental condensation was done through a novel consistency-check procedure. It has been shown that it provides analytical solution to local equilibrium for piece-wise linearized cohesive laws. Rather than assuming trial crack displacements and iterating for elemental

equilibrium such as in the Newton-Raphson method, it starts with trial cohesive segments in the cohesive laws and finds the analytical solution (in piece-wise linear sense) to the elemental equilibrium through a simple consistency check. For piece-wise linear cohesive laws with only a small number of possible stiffness segments, this algorithm is very efficient.

Through the numerical examples, it has been demonstrated that the new A-FEM method, empowered by the new elemental condensation algorithm, achieved very 2-3 orders of magnitude improvement in numerical accuracy, efficiency, and stability. The A-FEM's capabilities in high-fidelity simulations of interactive cohesive cracks in heterogeneous solids have also demonstrated through the benchmarking examples in this report (more substantial results are published in journal articles acknowledged to this project as listed in appendix A). Therefore, it is concluded that all the proposed research goals as listed in the beginning of this report have been achieved.

Furthermore, we have gone beyond the proposed goals of this study to expand the capability and to apply the A-FEM to benefit several other projects, through a wide collaboration with national and international university, US government laboratories, and US industrial companies (See details in Appendix C). These ongoing collaborations have generated sufficient interest elsewhere to be continuing beyond the life of the present program.

On the educational front, the project has benefitted three (4) PhD students, two (2) MS students, and two (2) post-doctorate researchers. Most of them have graduated and joined the US workforce as researchers in US research institutions and industrial companies.

References:

1. Cox, B.N. and Q.D. Yang, *In Quest of Virtual Tests for Structural Composites.* Science, 2006. **314**: p. 1102-1107.
2. LLorca, J., C. González, and e. al., *Multiscale modeling of composite materials: a roadmap towards virtual testing.* Advanced Materials, 2011. **23**: p. 5130-5147.
3. Yang, Q.D., et al., *Virtual Testing for Advanced Aerospace Composites: Advances and Future Needs.* Journal of Engineering Materials and Technology, 2011. **133**: p. 11002-11008.
4. Kaddour, A.S., et al., *Mechanical properties and details of composite laminates for the test cases used in the thrid world-wide failure exercise.* Journal of Composite Materials, 2013. **47**: p. 2427-2442.
5. Soden, P.D., M.J. Hinton, and A.S. Kaddour, *A comparison of the predictive capabilityies of current failure theories for composite laminates.* Composite Science and Technology, 1998. **58**: p. 1225-1254.
6. Fawcett, A., J. Trostle, and S. Ward, in *International Conference on Composite Materials*. 1997: Gold Coast, Australia.

7. Hallett, S.R. and M.R. Wisnom, *Experimental Investigation of Progressive Damage and the Effect of Layup in Notched Tensile Tests.* Journal of COMPOSITE MATERIALS, 2006b. **40**: p. 119-141.
8. Pierron, F., et al., *Full-field assessment of the damage process of laminated composite open-hole tensile specimens. Part II: Experimental results.* Composites: Part A, 2007. **38**: p. 2321-2332.
9. Van de Meer, F.P., *Mesolevel modeling of failure in composite laminates: contitutive, kinematic and algorithic aspects.* Archive of Computational Method in Engineering, 2012. **19**: p. 381-425.
10. Cox, B.N., et al., *Stochastic virtual tests for high temperature ceramic matrix composites.* Annual Reviews of Material Science, 2014. **44**: p. 17.1-17.51.
11. Huynh, D.B.P. and T. Belytschko, *The extended finite element method for fracture in composite materials.* International Journal for Numerical Methods in Engineering, 2009. **77**: p. 214-239.
12. Dolbow, J., N. Moës, and T. Belytschko, *An extended finite element method for modeling crack growth with frictional contact.* Computer Methods in Applied Mechanics and Engineering, 2001. **190**: p. 6825-6846.
13. Iarve, E.V., et al., *Mesh independent matrix cracking and delamination modelling in laminated composites.* International Journal for Numerical Methods in Engineering, 2011. **88**: p. 749-773.
14. Iarve, E.V., D. Mollenhauer, and R. Kim, *Theoretical and experimental investigation of stress redistribution in open-hole composite laminates due to damage accumulation.* Composites: Part A, 2005. **36**: p. 163-171.
15. Van de Meer, F.P., C. Oliver, and L.J. Sluys, *Computational analysis of progressive failure in a notched laminate including shear nonlinearity and fiber failure.* Composite Science and Technology, 2010. **70**: p. 692-700.
16. Van de Meer, F.P. and L.J. Sluys, *A phantom node formulation with mixed mode cohesive law for splitting in laminates.* International Journal of Fracture, 2009. **158**: p. 107-124.
17. de Borst, R., J.J.C. Remmers, and A. Needleman, *Mesh-independent discrete numerical representations of cohesive-zone models.* Engineering Fracture Mechanics, 2006. **73**(2): p. 160-177
18. Ling, D.S., Q.D. Yang, and B.N. Cox, *An augmented finite element method for modeling arbitrary discontinuities in composite materials.* International Journal of Fracture, 2009. **156**: p. 53-73.
19. Yang, Q.D., et al., *A-FEM for complex multi-scale damage evolution in laminated composites , May 2010.* Proceddings of SAMPE Technical Conference, Paper #465, 2010. **42**: p. 1-8.
20. Fang, X.J., et al., *High-Fidelity Simulations of Multiple Fracture Processes in a Laminated Composites in Tension.* Journal of the Mechanics and Physics of Solids, 2011. **59**: p. 1355-1373.
21. Liu, W., et al., *An Efficient Augmented Finite Element Method (A-FEM) for Arbitrary Cracking and Crack Interaction in Solids.* International Journal for Numerical Methods in Engineering, 2014. **99**: p. 438-468.
22. Yang, Q.D., M.D. Thouless, and S.M. Ward, *Numerical Simulations of Adhesively-Bonded Beams Failing with Extensive Plastic Deformation.* Journal of the Mechanics and Physics of Solids, 1999. **47**: p. 1337-1353.

23. Yang, Q.D. and B.N. Cox, *Cohesive Models for damage evolution in laminated composites.* International Journal of Fracture, 2005. **133**(2): p. 107-137.
24. Turon, A., et al., *A damage model for the simulation of delamination in advanced composites under variable-mode loading.* Mechanics of Materials, 2006. **38**: p. 1072-1089.
25. Wisnom, M.R. and F.-K. Chang, *Modelling of Splitting and Delamination in Notched Cross-Ply Laminates.* Composites Science and Technology, 2000. **60**: p. 2849-2856.
26. Hallett, S.R. and M.R. Wisnom, *Numerical investigation of progressive damage and the effect of layup in notched tensile tests. Journal of Composites Materials*, 2006a. **40**: p. 1229-1245.
27. Xu, X.-P. and A. Needleman, *Numerical Simulations of Fast Crack Growth in Brittle Solids.* Journal of the Mechanics and Physics of Solids, 1994. **42**: p. 1397-1434.
28. Hutchinson, J.W. and A.G. Evans, *Mechanics of Materials: Top-Down Approaches to Fracture.* Acta Materialia, 2000. **48**: p. 125-135.
29. Davila, C.G., P.P. Camanho, and C.A. Rose, *Failure Criteria for FPR Laminates.* Journal of Composite Materials, 2005. **39**: p. 323-345.
30. Camanho, P.P., et al., *Prediction of in situ strengths and matrix cracking in composites under transverse tension and in-plane shear.* Composite Part A: Applied Science and Manufacturing, 2006. **37**: p. 165-176.
31. Chang, K.Y., S. Liu, and F.K. Chang, *Damage Tolerance of Laminated Composites Containing an Open Hole and Subjected to Tensile Loadings.* Journal of Composite Materials, 1991. **25**: p. 274-301.
32. Fang, X.J., et al., *An Augmented Cohesive Zone Element for Arbitrary Crack Coalescence and Bifurcation in Heterogeneous Materials.* International Journal for Numerical Methods in Engineering, 2011. **88**: p. 841-861.
33. Ling, D.S., et al., *Nonlinear fracture analysis of delamination crack jumps in laminated composites.* Journal of Aerospace Engineering, 2011. **24**: p. 181-188.
34. Yang, Q.D., et al., *An Improved Cohesive Element for Shell Delamination Analyses.* International Journal for Numerical Methods in Engineering, 2010. **83**(5): p. 611-641.
35. Morris, W.L., R.V. Inman, and B.N. Cox, *Microscopic Deformation in a Heated Unidirectional Graphite/Epoxy Composite.* Journal of Materials Science, 1989. **24**: p. 199-204.
36. Cox, B.N., et al., *Failure Mechanisms of 3D Woven Composites in Tension, Compression, and Bending.* Acta Metallurgica et Materialia, 1994. **42**: p. 3967-3984.
37. Cox, B.N., M.S. Dadkah, and W.L. Morris, *On the tensile failure of 3D woven composites.* Composites, Part A, 1996. **27A**: p. 447-458.
38. Borden, M.J., et al., *A phase-field description of dynamic brittle fracture*. 2011, The Institute for Computational Engineering and Sciences, The University of Texas at Austin.
39. Miehe, C., M. Hofacker, and W. F., *A phase field model for rate-independent crack propagation: Robust algorithmic implementation based on operator splits.* Computer Methods in Applied Mechanics and Engineering, 2010. **199**: p. 2765–2778.
40. Bourdin, B., G.A. Francfort, and J.J. Marigo, *The variational approach to fracture.* Journal of Elasticity, 2008. **91**: p. 5-148.
41. Belytschko, T., J. Fish, and B.E. Engelmann, *A finite element with embedded localization zones.* Computer Methods in Applied Mechanics and Engineering, 1988. **70**(1): p. 59-89.

42. Dvorkin, E.N., A.M. Cuitiño, and G. Gioia, *Finite elements with displacement interpolated embedded localization lines insensitive to mesh size and distortions.* International Journal for Numerical Methods in Engineering, 1990. **30**(3): p. 541-564.
43. Ortiz, M., A. Leroy, and A. Needleman, *A finite element method for localized failure analysis.* Computational methods in Applied Mechanics and Engineering, 1987. **61**: p. 189–214.
44. Simo, J.C. and M.S. Rifai, *A class of mixed assumed strain methods and the method of incompatible modes.* International Journal for Numerical Methods in Engineering, 1990. **29**: p. 1595-1638.
45. Wriggers, P. and J. Korelc, *On enhanced strain methods for small and finite deformation of solids.* Computational Mechanics, 1996. **18**(413-428).
46. Simo, J.C. and T.J.R. Hughes, *On the variational foundations of assumed strain methods.* Journal of Applied Mecanics, 1986. **53**: p. 51-54.
47. Alfaiate, J., G.N. Wells, and L.J. Sluys, *On the use of embedded discontinuity elements with crack path continuity for mode-I and mixed-mode fracture.* Engineering Fracture Mechanics, 2002. **69**: p. 661-686.
48. Ibrahimbegovic, A. and S. Melnyk, *Embedded discontinuity finite element method for modeling of localized failure in heterogeneous materials with structured mesh: an alternative to extended finite element method.* Computational Mechanics, 2007. **40**(1): p. 149-155.
49. Sluys, L.J. and A.H. Berends, *Discontinuous failure analysis for mode-I and mode-II localization problems.* Int. J. Solids Struct., 1998. **35**: p. 4257–4274.
50. Linder, C. and F. Armero, *Finite elements with embedded branching.* Finite Elements in Analysis and Design, 2009. **45**: p. 280-293.
51. Linder, C. and F. Armero, *Finite elements with embedded strong discontinuities for themodeling of failure in solids.* International J. Numer. Meth. Engng, 2007. **72**: p. 1391-1433.
52. Dias-da-Costa, D., et al., *Towards a generalization of a discrete strong discontinuity approach.* Computational methods in Applied Mechanics and Engineering, 2009. **198**: p. 3670-3681.
53. Rudraraju, S., et al., *In-plane fracture of laminated fiber reinforced composites with varying fracture resistance: Experimental observations and numerical crack propagation simulations.* International Journal of Solids and Structures, 2010. **47**: p. 901-911.
54. Jirásek, M., *Comparative study on finite elements with embedded discontinuities.* Computer Methods in Applied Mechanics and Engineering, 2000. **188**: p. 307-330.
55. Simo, J.C., J. Oliver, and F. Armero, *An analysis of strong discontinuities induced by softening solutions in rate-independent solids.* Journal of Computaional Mechanics, 1993. **12**: p. 277-296.
56. Armero, F. and K. Garikipati, *An analysis of strong discontinuities in multiplicative finite strain plasticity and their relation with the numerical simulation of strain localization in solids.* International Journal of Solids & Structures, 1996. **33**: p. 2863-2885.
57. Liu, W., et al., *An Accurate and Efficient Augmented Finite Element Method for Arbitrary Crack Interactions.* Journal of Applied Mechanics, 2013. **80**: p. 041033-1,-12.
58. Kafkalidis, M.S., et al., *Deformation and Fracture of An Adhesive Layer Constrained by Plastically-Deforming Adherends.* International Journal of Adhesion Science and Technology, 2000. **14**: p. 1593-1646.

59. Thouless, M.D. and Q.D. Yang, *A parametric study of the peel test.* International Journal of Adhesion & Adhesives, 2008. **28**: p. 176-184.
60. Ling, D.S., et al., *A Finite Element Method with Mesh-Separation Based Approximation Technique and Its Application in Modeling Crack Propagation with Adaptive Mesh Refinement.* International Journal for Numerical Methods in Engineering, 2014. **99**: p. 487-521.
61. Wang, J.S. and Z. Suo, *Experimental determination of interfacial toughness using Brazil-nut-sandwich.* Acta. Metallurgica, 1990. **38**: p. 1279-1290.
62. Parmigiani, J. and M.D. Thouless, *The Effects of cohesive strength and toughness on mixed-mode delamination of beam-like geometries.* Engin. Fract. Mech., 2007. **74**: p. 2675-2699.
63. Goutianos, S. and B.F. Sorensen, *Path dependence of truss-like mixed mode cohesive laws.* Engineering Fracture Mechanics, 2012. **91**: p. 117-132.
64. Remmers, J.C., *Discontinuities in Materials and Structures -- A Unifying Computational Approach*. 2006, Delft University.
65. de Borst, R., *Numerical aspects of cohesive zone models.* Engineering Fracture Mechanics, 2003. **70**: p. 1743-1757.
66. Moës, N. and T. Belytschko, *Extended finite element method for cohesive crack growth.* Engineering Fracture Mechanics, 2002. **69**: p. 813-833.
67. Yang, Q.D. and M.D. Thouless, *Mixed Mode Fracture of Plastically-Deforming Adhesive Joints.* International Journal of Fracture, 2001. **110**: p. 175-187.
68. Yang, Q.D., et al., *Fracture and Length Scales in Human Cortical Bone: The necessity of Nonlinear Fracture Models.* Biomaterials, 2006a. **27**: p. 2095-2113.
69. Cavalli, M.N., M.D. Thouless, and Q.D. Yang, *Modeling the Deformation and Fracture of Weld-bonded Joints.* Welding Journal, 2004. **83**: p. 133S-139S.
70. Cavalli, M.N., M.D. Thouless, and Q.D. Yang, *Modeling the Deformation and Failure of Aluminum Spot Welded Joints.* International Journal of Fatigue and Fracture, 2005. **28**: p. 861-874.
71. Mousavi, S.E., H. Xiao, and N. Sukumar, *Generalized Gaussian quadrature rules on arbitrary polygons.* International Journal for Numerical Methods in Engineering, 2010. **82**: p. 99-113.
72. Sukumar, N., B. Moran, and T. Belytschko, *The natural element method in solid mechanics.* International Journal for Numerical Methods in Engineering, 1998. **43**: p. 839-887.
73. Jones, R.M., *Mechanics of Composite Materials (2nd edition)*. 1999, New York: Brunner-Routledge.
74. Do, B.C., et al., *Improved Cohesive Stress Integration Schemes for Cohesive Zone Elements* Engineering Fracture Mechanics, 2013. **107**: p. 14-28.
75. Dias-da-Costa, D., et al., *An embedded formulation with conforming finite elements to capture strong discontinuities.* Int. J. Numer. Meth. Engng, 2013. **93**: p. 224-244.
76. De Borst, R., et al., *Nonlinear Finite Element Analysis of Solids and Structures*. 2012: John Wiley & Sons.
77. Cervera, M., M. Chiumenti, and R. Codina, *Mixed stabilized finite element methods in nonlinear solid mechanics PartII: strain localization.* Computer Methods in Applied Mechanics and Engineering, 2010. **199**: p. 2571-2589.

78. Liu, W., et al., *Numerical Performance of a Consistency-Check Based Algorithm for Element Condensation in Augmented Finite Element Methods.* International Journal of Fracture, 2014: p. submitted.
79. Naderi, M., D. Schesser, and Q.D. Yang, *Augmented finite element method for arbitrary cracking in 3D solids.* International Journal of Fracture, 2014. **submitted**.
80. Areias, P.M.A. and T. Belytschko, *Analysis of three-dimensional crack initiation and propagation using the extended finite element method.* International Journal for Numerical Methods in Engineering, 2005. **63**(5): p. 760-788.
81. Gasser, T.C. and G.A. Holzapfel, *3D Crack propagation in unreinforced concrete. A two-step algorithm for tracking 3D crack paths.* Computer Methods in Applied Mechanics and Engineering, 2006. **195**(37-40): p. 5198-5219.
82. Oliver J, H.A., *On strategies for tracking strong discontinuities in computational failure mechanics.* In Proceedings of the Fifth World Congress on Computational Mechanics (WCCM V), Vienna, Austria, Mang HA, Rammersdorfer FG, Erberhardsteiner J (eds), 2002.
83. Oliver, J., et al., *Continuum approach to the numerical simulation of material failure in concrete.* International Journal for Numerical and Analytical Methods in Geomechanics, 2004. **28**(7-8): p. 609-632.
84. Pinho, S.T., et al., *Material and strcutural response of polymer-matrix fiber-reinforced composites.* Journal of Composite Materials, 2012. **46**: p. 2313-2341.
85. Vogler, M., R. Rolfes, and P.P. Camanho, *Modeling the inelastic deformation and fracture of polymer composites – Part I: Plasticity model.* Mechanics of Materials, 2013. **59**: p. 50-64.
86. Yang, Q.D., et al., *On crack initiation in notched, cross-plied polymer matrix composites.* Journal of the Mechanics and Physics of Solids, 2015. **78**: p. 314-332.
87. Xie, J. and A. Waas, *Predictions of delamination growth for quasi-static loading of composite laminates.* Journal of Applied Mechanics, 2015. **82**(8): p. 081004-081004-12.
88. Cox, B.N., W.C. Carter, and N.A. Fleck, *A Binary Model of textile composites: I Formulation.* Acta Metallurgica et Materialia, 1994. **42**: p. 3463-3479.
89. Yang, Q.D. and B.N. Cox, *Spatially Averaged Local Strains in Textile Composites via the Binary Model Formulation.* Journal of Engineering Materials and Technology, 2003. **125**: p. 418-425.
90. Yang, Q.D. and B.N. Cox, *Predicting failure in textile composites using the Binary Model with gauge-averaging.* Engineering Fracture Mechanics, 2010. **77**(16): p. 3174-3189.
91. Vanaerschot, A., et al., *Multi-scale modelling strategy for textile composites based on stochastic reinforcement geometry.* Computational methods in Applied Mechanics and Engineering, 2016. **310**: p. 906-934.
92. Carpinteri, A., et al., *Is mode II fracture energy a real material property?* computers and structures, 1993. **48**(3): p. 397-413.
93. Turon, A., et al., *An Engineering Solution for Mesh Size Effects in the Simulation of Delamination Using Cohesive Zone Models.* Engin. Fract. Mech., 2007. **74**: p. 1665-1682.
94. Mohammadizadeh, S., *A novel Augmented Finite Element Method for Modeling Arbitrary Cracking in 2D Solids*, in *Dept of Mechanical and Aerospace Engineering* University of Miami, PhD thesis, 2013.

95. Bale, H., et al., *Characterizing Three-Dimensional Textile Ceramic Composites using Synchrotron X-Ray Micro-Computed-Tomography.* Journal of the American Ceramic Society, 2011. **95**(1): p. 392-402.
96. Rinaldi, R., et al., *Generating virtual textile composite specimens using statistical data from micro-computed tomography: 3D tow representations.* Journal of the Mechanics and Physics of Solids, 2012. **60**(8): p. 1561-1581.
97. Yang, Q.D., et al., *Evaluation of macroscopic and local strains in a 3D woven C/SiC composite.* Journal of American Ceramics Society, 2005. **88**: p. 719-725.
98. Berbon, M.Z., et al., *Effect of weave architecture on tensile properties and local strain heterogeneity in thin-sheet C-SiC composites.* Journal of the American Ceramic Society, 2002. **85**: p. 2039-2048.
99. Prabhakar, P. and A. Waas, *A novel continuum-decohesive finite element for modeling in-plane fracture in fiber reinforced composites.* Composites Science and Technology, 2013. **83**: p. 1-10.
100. Nojavan, S., D. Schesser, and Q.D. Yang, *An In Situ Fatigue Cohesive Zone Model for Crack Propagation in Composites under Cyclic Loading.* International Journal of Fatigue, 2016. **82**: p. 449-461.
101. Nojavan, S., D. Schesser, and Q.D. Yang, *A Unified Fatigue-CZM for Crack Initiation and Propagation in Composites under Cyclic Loading.* Composite Structures, 2016. **146**: p. 34-49.
102. Iarve, E.V., K.H. HOOS, and D. Mollenhauer. *Damage Initiation and Propagation Modeling in Laminated Composites under Fatigue Loading*. in *American Society for Composites 29th Technical Conference*. 2014. La Jolla, CA.
103. Flores, S., et al., *A computational tool for design and analysis of 3D ceramics composite structures.* Composite: A, 2010. **41**: p. 222-229.

Appendix A: Journal Publications/Book Chapters

Published/accepted (18):

1. Q. D. Yang and B. C. Do, "Predicting Damage Evolution in Composites with Explicit Representation of Discrete Damage Modes", Handbook of Damage Mechanics: Nano to Macro Scale for Materials and Structures, editor George Voyiadjis. SpringerReference, New York, 2014 (book chapter)
2. W. Liu, Q.D. Yang*, S. Mohammadizadeh, and X.Y. Su, "An Efficient Augmented Finite Element (A-FEM) for Arbitrary Cracking and Crack Interaction in Solids", *International Journal of Numerical Methods in Engineering*, **99** (438-468), 2014.
3. D.S. Ling*, L.F. Bu, F.B. Tu, Q.D. Yang, and Y.M. Chen, "A finite element method with mesh-separation-based approximation technique and its application in modeling crack propagation with adaptive mesh refinement", *International Journal of Numerical Methods in Engineering,* **99 (487-521)**, 2014
4. F.B. Tu, D.S. Ling*, L.F. Bu, and Q.D. Yang, Generalized bridging domain method for coupling finite elements with discrete elements, *Computer Methods in Applied Mechanics and Engineering*, **276** (509-533), 2014.
5. Q. D. Yang*, D. Schesser, M. Niess, P. Wright, M. Mavrogordato, I. Sinclair, S. M. Spearing, and B. N. Cox, "On crack initiation in notched, cross-plied polymer matrix composites", *Journal of the Mechanics and Physics of Solids***,** **78** (314-332). 2014.
6. C. X. Zhang, J. Z. Song, Q. D. Yang, "Periodic buckling patterns of graphene/hexagonal boron nitride heterostructure", N*anotechnology*, ***25*** (445401-10), 2014
7. Q. Xu, W.M. Tao, S.X. Qu*, Q. D. Yang, "A cohesive zone model for the elevated temperature interfacial debonding and frictional sliding behavior", *Composite Science and Technology*, ***110*** (45-52), 2015
8. W. Liu, D. Schesser, Q. D. Yang and D.S. Ling, "A Consistency-Check Based Algorithm for Element Condensation in Augmented Finite Element Methods for Fracture Analysis", *Engineering Fracture Mechanics*, ***139*** (78-97), 2015.
9. Y. C. Gu, J. Jung, Q. D. Yang, and W. Q. Chen, "A New Stabilizing Method for Numerical Analyses with Severe Local and Global Instability**",** *ASME Journal of Applied Mechanics,* **82** (101010-1, -12), 2015
10. J. Jung, B. C. Do, and Q. D. Yang, "A-FEM for Arbitrary Cracking and Crack Interaction in Solids under Thermo-Mechanical Loadings", *Philosophical Transactions A***. 374**: 20150282.2016
11. G. Borstnar, M. N. Mavrogordato, Q. D. Yang, I. Sinclair, and S. M. Spearing, "Crack path simulation in a particle-toughened interlayer within a polymer composite laminate", *Composite Science & Technology* **133** (89-96). 2016
12. A. Vanaerschot, B. N. Cox, S. V. Lomov, D. Vandepitte, "Multi-scale modelling strategy for textile composites based on stochastic reinforcement geometry," Comput. Methods Appl. Mech. Engrg. 310 (906–934). 2016
13. M. Naderi, J. Jung, and Q. D. Yang, "A three-dimensional Augmented Finite Element for Modeling arbitrary cracking in solids", International Journal of Fracture, 192 (147-168). 2016

14. J. Jung and Q. D. Yang, “A Two-Dimensional Augmented Finite Element for Dynamic Crack Initiation and Propagation”. *International Journal of Fracture*. 203 (41-61). 2017
15. G. D. Nian, Y. J. Shan, S.X. Qu, and Q. D. Yang, “Failure analysis of syntactic foams: a computational model with cohesive law and XFEM”, *Composites Part B*. **89** (18-26), 2016
16. B. N. Legarth and Q. D. Yang, “Micro-mechanical analyses of debonding and matrix cracking in dual-phase materials”, *ASME Journal of Applied Mechanics*, **83** (051006-1, -9), 2016
17. J. S. Hu, K. F. Zhang, Q.D. Yang, H. Cheng, Y. Yang, An experimental study on bearing response of single-lap bolted composite interference-fit joints. ***In press***, *Composite: Part B*. 2017
18. J.S. Hu, K. F. Zhang, Q. D. Yang, C. Hui, S. N. Liu, Y. Yang, Fretting behaviors of interface between CFRP and coated titanium alloy in composite interference-fit joints under service condition. ***In press***, *Materials & Design*, 2017

Manuscripts in Preparation:

1. Y.W. Xu, J. Jung, S. Nojavan, and Q.D. Yang, “An Orthotropic A-FEM for Progressive Damage Analyses of Laminar Composites with Explicit Presentation of All Major Damage Modes,” in preparation for possible submission to Composite A, 2017.
2. J. Quek and B. N. Cox, “Graph theory analysis of rich fiber-scale data opens a new route to high-fidelity simulations of damage evolution in composites,” in preparation for submission to *JMPS*, 2017.
3. Y.W. Xu, J. Jung, and Q. D. Yang, “Effects of fine scale nonlinearity on coupled delamination and ply cracking in laminated composites,” in preparation for possible submission to Composites & Structures, 2017.
4. Q.D. Yang, T. A. Parthasarathy, O. Sudre, B.N. Cox, “Coupled Binary Model (CDM) and Continuum Damage Model (CDM) for Failure Analysis of Textile CMC Structures Subject to Environmental Degradation, ” in presparation for possible submission to the Journal of American Ceramics Society. 2017.
5. Q.D. Yang, Y. H. Yang, O. Sudre, B.N. Cox, “Coupled Binary Model (CDM) and Continuum Damage Model (CDM) for Progressive Failure Analysis of Large Textile CMC Structures, ” in presparation for possible submission to the Journal of American Ceramics Society. 2017.

Appendix B: Graduate Students/Post-Doctorate Researchers

1. Dr. Mehdi Naderi (former post-doc researcher, 12/2012-4/2014), 80% Effort. Now with Technical Data Analysis, Inc, Washington, DC.
2. Dr. Jaedal Jung (former post-doc Researcher, 7/2014-4/2017), overall 30% effort since 7/2014. Now with Teledyne Scientific Company, Thousand Oaks, CA.
3. Dr. Derek Schesser (Ph.D student, graduated in 5/2015), 50% support from this project during 2013-2015. Now a DARPA Science Engineering Technology Advisor (SETA).
4. Ms. Brigitte Morales (PhD student, 6/2014-5/2015), 50% support. Left this program and joined another group in the department in 6/2015 after being awarded with an NSF scholarship.
5. Ms. Yunwei Xu (PhD student in progress), supported by this project 100% from 8/15/2014-8/14/2016.
6. Mr. Yuhang Yang (PhD student in progress) supported 100% from 8/15/2016-8/14/2017.
7. Mr. Scott Floerke (MS student graduated 5/2017). Performed C4 blast simulations on aluminum panels under joined advising of the PI and Dr. Chian-fong Yen in ARL.
8. Mr. James Robertson (MS student graduated 5/2017). Programed a fiber/matrix model generator using python script language which enabled high-fidelity RVE analyses.

Appendix C: Collaborations and Technical Transfer

The key enabling capabilities developed in this study, especially the discrete modeling capability, have benefitted several other federally and industrially supported research projects. In the meanwhile, the current project has also been significantly enriched in the process of fulfilling specific requirements of these projects, as well as in gaining much improved understandings on the progressive failure processes through analyzing the materials provided by these leveraging projects.

1. ***Behavior and Life Prediction of SiC/SiC CMCs for Turbine Applications, PI: Brian Cox, Teledyne Scientific Company, AFRL Contract number: FA8650-13-C-5212***

   This project, concluded in June 2017, involved multiple groups from AFRL, universities (Univ. Miami, UC-Santa Barbara), and leading industrial companies (Teledyne, Honeywell). In this project, the 1D breakable tow element is integrated with an AFRL environmental code to account for the time- and temperature- dependent degradation of tow modulus and strength when subjected to hostile high temperature environmental condistions. The 3D A-FE has also been enriched with temperature DoFs so that it can be used to compute the steady-state or transient temperature fields in UHT structures, and the possible temperature dependent material properties. Based on a previously established modeling technology, the Binary Model (BM), two strategies for textile CMCs have been tested: 1) coupled BM-AFEM that can explicitly account for the matrix cracking, and the temperature- and environment-dependent tow failure; 2) coupled BM-CDM that uses calibrated continuum damage mechanics model (CDM) to account for the material degradation due to numerous initial flaws and matrix microcracking. The first strategy is far more computationally costly but can provide high-fidelity material failure information (suitable for microscopic or unit cell level analysis with adequately characterized initial material configuration). The second strategy is less accurate and requires experimental calibration from physical testing of real a material, but it does provide a quick and effective means for rapid analyses of large CMC structures (see section 6.5 for example). This is a key contribution to the research community in ultra-high temperature (UHT) materials and structures.

2. ***DARPA Materials Development Platform (MDP), PI: Olivere Sudre, Teledyne Scientific Company.***

   The thermal-mechanical A-FEM (with steady-state and transient temperature DoFs) have enabled us to team up with Teledyne (led by Dr. Olivier Sudre) to test its capability in virtual testing of new materials of interest to DARPA. The coupled BM-CDM strategy serves as an essential platform in virtual development and assessment of high-temperature composite structures such as airfoils. The program is expected to transfer to Teledyne and DARPA by December 2017.

3. ***Micromechanical Failure Analysis of Aligned Low-Aspect Short Fiber Composite Materials for TFF, PI: Ryan Karkkainen, University of Miami. DARPA Award No. HR0011725815.***

In this project, the 3D A-FEM is being used to assess the mechanical properties of short-fiber reinforced polymers. The fact that the A-FEM allows for explicit representation of all failure modes at microscopic level (fiber breakage, matrix cracking, and fiber/matrix interface debonding) in a material domain of significance volume may offer a new way of predicting such composite properties without homogenization, which typically requires calibration parameters from real materials.

4. ***Composite Progressive Damage Analyses. The Boeing Company. PI: Qingda Yang.***

We have been supported by Boeing Structural Damage Technology Group since 2014 to further develop the A-FEM for progressive fatigue damage analysis with explicit consideration of multiple discrete crack formation and propagation. Under this support, the 2D A-FEM has been extended greatly to include many material characteristics crucial to composite failure, including material orthotropy, shear nonlinearity, temperature dependent material and fracture properties. More critically, the 2D A-FEM now has the capability of initiating multiple types of cracks observed in different plies in a composite laminate (matrix cracking in tension, shear, and compression, fiber rupture in tension and kinking in compression, all coupled with possible delamination as shown in section 6.4.2), under either static or cyclic loadings. The 2D fatigue A-FEM has been successfully transfer to Boeing and is currently being subjected to their internal evaluation (with their proprietary material properties). Boeing is currently supporting us to develop a 3D brick element which can be more convenient for laminated composites.

5. ***Continued Collaboration with Army Research Laboratories (ARL)***

Since the beginning of this project, we have been in collaboration with researchers in ARL (Dr. C.F. Yen) to work on problems of mutual interests. During the project period two of our students, Derek Schesser (then PhD candidate, 2014) and Scott Floerke (then MS student, 2017) worked with Dr. Yen as summer interns. Derek helped to transfer the earlier version of the 2D A-FEM into the ARL computing platform and worked under Dr. Yen’s guide on the development and instrumentation of a novel high-speed torsional test facility at ARL. Scott Floerke worked on the dynamic fracture of aluminum panel, using both our dynamic A-FEM and the commercial software LS-Dyna and ABAQUS. This collaboration resulted a MS thesis and a journal paper is in preparation. We are ready to transfer the much more matured version of the A-FEM upon request.

6. ***Collaboration with National/International Universities***

We have been in close collaboration with Dr. Spearing’s group in Southampton University (UK, Dr. Mark Spearing) on application, validation, and verification of the A-FEM predictions with in-situ micro-CT measurements of composites. Dr. Spearing’s group has access to the state-of-art micro-CT measurement facilities and has a wealth of in-depth material toughening data and their correlation with the in-situ observation of the microscopic damage development. This collaboration has so far resulted in two high-profile journal publications and this collaboration is continuing.

We are also in collaborating with Professors in Demark Technical University (DTU, Profs. Bent Sorensen, Brian Legarth) on coupling A-FEM simulation with their state-of-art capability of in-situ SEM for microscopic measurement of fiber/matrix bonding properties.

The major research findings have been published in the ASME Journal of Applied Mechanics.

In collaboration with the Department of Engineering Mechanics at Zhejiang University, we have studied the failure mechanisms in syntactic foams and the cyclic thermal-mechanical response of fiber/matrix interfaces, which resulted two joint publications.

We are also in collaboration with a visiting student from the Northwestern Polytechnical University of China (Mr. Junsan Hu) to investigate the joining technologies for composite materials. In particular, we attempt to gain understandings through experimental testing on the local damages surrounding those pin-holes in typical bearing joints due to mechanical insertion and in-service attrition. We have co-authored two journal publications.

Dr. Brian Cox, our subcontractor at Arachne Consulting, has been collaborating extensively with Dr. Yang and with third parties in three projects that were undertaken to broaden the scope of applications of AFEM in problems of interest to the Army and the materials development community. We have been in collaboration Teledyne to Generating code for textile reinforced components; with Dr. Jerry Quek of the Institute for High Performance Computing (IHPC), Singapore, to explore methods of generating defect populations at the fiber scale in a nominally unidirectional ply by extremely fast computational methods based on graph theory; with Dr. X. Boyang in the Delft University (Netherland) to study the fundamental question of how bifurcation of a crack, or the coalescence of two cracks, occurs when the mother crack and the mother/daughter pair are governed by a nonlinear spatially-distributed fracture zones.

All of these collaboration projects have generated sufficient interest elsewhere to be continuing beyond the life of the present program.